

Effects of Climate Change on the Physical Conditions of the Brazilian Shelf

Dissertation

with the aim of achieving a doctoral degree

at the faculty of Mathematics, Informatics and Natural Sciences

Department of Earth Sciences

at Universität Hamburg

submitted by

Mihael Machado de Souza

from Natal (RN), Brazil

Hamburg, 2020

Accepted as Dissertation
at the Department of Earth Sciences, Universität Hamburg

Reviewed by **PD Dr. Thomas Pohlmann**
and **Dr. Moritz Mathis**

Hamburg, 13.10.2020
(Day of Oral Defense)

Prof. Dr. Dirk Gajewski
Chair of the Subject Doctoral Committee

Prof. Dr. Heinrich Graener
Dean of the MIN Faculty

*"Success is the ability to move
from one failure to another
without loss of enthusiasm."
- Anonymous*

Abstract

Earth System Models (ESM) cannot properly resolve all relevant drivers within shelf seas due to their coarse resolution, as shallow depths and cross-shelf exchange processes modify the response of coastal waters to anthropogenic climate change on regional scales. To account for these local processes, we downscaled results from the MPI-ESM-MR (RCP8.5 scenario) to a domain of the South Atlantic Ocean with a horizontal resolution of $1/12^\circ$, using the HAMSOM model. Our analysis focus on process that have a direct connection to the physical conditions along the Brazilian shelf, simulating the period from 1950 to 2100 and capturing the evolution of conditions from the recent past until the end of the 21st century. In essence, all the identified impacts stem from the southwestward migration of the South Atlantic Subtropical High (SASH), in response to the widening of the Hadley cells and the poleward migration of the westerlies. On a synoptic scale, the strengthening and narrowing of the Southern Ocean atmospheric circulation leads to a decrease of the Malvinas Current (MC) transport, as it forces the Antarctic Circumpolar Current to flow closer to Antarctica. With a weaker MC and no significant impact to the Brazil Current transport, the Brazil-Malvinas confluence continuously migrates poleward during the 21st century and its intra-annual variability reduces by approximately half of its historical range. On a regional scale, although the SASH's migration is not accompanied by an increase in its intensity, the closer proximity to the Brazilian coast leads to a strengthening of alongshore winds ($\approx 2 \text{ m s}^{-1}$). This, in turn, increases the offshore Ekman forcing and promote an enhanced onshore bottom intrusion of South Atlantic Central Water (SACW), specially along southeast Brazil. This wider bottom intrusion, however, does not translate into increased vertical flows at the bottom of the mixed layer. Increased surface heating and, in the mid-to-outer shelf area where SACW is dominant, the shoaling of the pycnocline seems to counteract and limit vertical flows, as the shelf waters become more stratified. This is because both processes contribute to a stronger pycnocline gradient, which inhibit fluxes between the surface and deeper shelf waters. Nevertheless, the presence of the SACW upwelling acts as a dampening mechanism over the warming of surface waters. This keeps the increase in sea surface temperature below global projections and can even lead to colder surface waters, as is the case around Cabo Frio where the upwelling process exerts a dominant influence. Ultimately, we identified that the subtropical Brazilian shelf, in particular the South Brazil Bight, is likely to experience greater modifications to its physical conditions than waters along tropical Brazil. This is in contrast to what is suggested by global projections, and highlights the importance of taking into account the regional forcing when considering long-term impacts at coastal regions.

Zusammenfassung

Erdsystemmodelle (ESM) können aufgrund ihrer groben Auflösung nicht alle relevanten Prozesse in Schelfmeeren hinreichend genau auflösen. Die geringen Wassertiefen sowie Austauschprozesse mit dem offenen Ozean haben einen wesentlichen Einfluss auf die Veränderung von Küstengewässern durch den anthropogen verursachten Klimawandel. Um diese lokalen Prozesse besser zu erfassen, haben wir die Ergebnisse des MPI-ESM-MR (RCP8.5-Projektion) mit Hilfe des regionalen hydrodynamischen Modells HAMSOM für den Bereich des Südatlantiks mit einer horizontalen Auflösung von $1/12^\circ$ regionalisiert. Unsere Analyse konzentrierte sich auf die Prozesse, die in direktem Zusammenhang mit den physikalischen Bedingungen entlang des brasilianischen Schelfs stehen. Wir simulierten den Zeitraum von 1950 bis 2100 und erfassten damit die Entwicklung der Bedingungen von der jüngeren Vergangenheit bis zum Ende des 21. Jahrhunderts. Im Wesentlichen sind alle identifizierten klimabedingten Änderungen auf die Südwestverlagerung des Subtropischen Wirbels im Südatlantik (SASH) als Reaktion auf die Verstärkung der Hadley-Zelle und die damit verbundene polwärtige Verlagerung der Westwindzone zurückzuführen. Auf synoptischer Skala führt die Bündelung und Verstärkung der atmosphärischen Zirkulation im Südpolarmeer zu einer Verringerung des Transports des Malvinenstroms (MC), da sich der Antarktische Zirkumpolarstrom näher in Richtung Antarktis verschiebt. Infolge eines schwächeren MC und ohne eine signifikante Änderung des Transports des Brasilstroms wandert die Brasil-Malvinenstrom-Konfluenzzone im Laufe des 21. Jahrhunderts kontinuierlich Richtung Süden, während sich ihre saisonale Variabilität auf etwa die Hälfte verringert. Obwohl die Verlagerung des SASH nicht direkt mit einer Zunahme seiner Intensität verbunden ist, verstärken sich die Windgeschwindigkeiten entlang der brasilianischen Küste wegen der Annäherung des Wirbels an den südamerikanischen Kontinent um $\text{ca. } 2 \text{ m s}^{-1}$. Dies wiederum verstärkt den Offshore-Ekman-Transport, was insbesondere entlang der Küste Südostbrasiliens zu einem verstärkten Vordringen von Südatlantischem Zentralwasser (SACW) als Bodenwasser Richtung Küste führt. Dieser verstärkte Einfluss des SACW führt jedoch nicht zu einer zu erwartenden erhöhten vertikalen Strömung an der unteren Begrenzung der durchmischten Deckschicht. Die Ursache hierfür liegt in einer stärkeren vertikalen Schichtung des Schelfwassers als Folge einer nun flacheren Pyknokline in Verbindung mit einer erhöhten Oberflächenerwärmung. Dieses Phänomen ist besonders ausgeprägt in den Bereichen des mittleren bis äußeren Schelfs, in denen das SACW dominiert. Vor allem dort tragen beide Prozesse zu einem stärkeren Gradienten in der Pyknokline bei, was auf dem Schelf den Austausch zwischen durchmischem Oberflächenwasser und dem Wasser aus tieferen Schichten hemmt. Der trotz der stabil-

eren Schichtung vorhandene Auftrieb des SACW dämpft auf der anderen Seite die Erwärmung des Oberflächenwassers. Dies reduziert bei globalen Projektionen des anthropogenen Klimawandels den Anstieg der Meeresoberflächentemperatur und kann sogar zu kälterem Oberflächenwasser führen, wie es bei Cabo Frio der Fall ist, wo der Auftriebsprozess dominiert. Zusammenfassend haben wir festgestellt, dass die subtropischen Bereiche des brasilianischen Schelfes, insbesondere die Südbrasilianische Bucht, wahrscheinlich größere Veränderungen ihrer physikalischen Bedingungen erfahren werden als die Gewässer entlang der tropischen Küste Brasiliens. Dies steht im Gegensatz zu den Prognosen globaler Projektionen und unterstreicht die Notwendigkeit, bei der Betrachtung langfristiger Auswirkungen des Klimawandels auf Küstenregionen auch die regionalen Einflüsse stärker zu berücksichtigen.

Acknowledgments

First of all, I'd like to thank my supervisors, Dr. Thomas Pohlmann and Dr. Moritz Mathis. Our discussions regarding the different approaches to climate downscaling and your encouragement and confidence when I wanted to try unorthodox methodologies were greatly appreciated. Thomas, I'm specially grateful to you for taking a chance on me, even though we hardly knew each other. In the end, you allowed me to pursue my own interests and essentially design my own project, being there to offer guidance whenever I felt stuck. To the other members of our research group, Dr. Bernhard Mayer, Dr. Abdul Basit, Zhang Zheen and Wenguo Li, a special thanks for all the conversations and lunches. They always offered some respite to the academic mindset, and made for some memorable discussions. Finally, I would also like to thank Dr. Alexa Griesel, who always offered a strong perspective on how clear my text and ideas were during our panel meetings. These remarks were invaluable in helping me put my manuscripts in better shape each time around.

To the friends made along the way, Chris, Phil, Jason, Linda, Romain and Justine. You provided me with much needed entertainment and fun, to take the mind off of work sometimes. To my family, thank you for the support and encouragement through all the highs and lows (those specially!) during this journey. In special to my wife, Ana. We've been partners for over 12 years now, and you always believed in me, even when I did not believe in myself.

Lastly, I'd like to thank the Deutscher Akademischer Austauschdienst (DAAD) for the scholarship provided. It allowed me to experience a research culture different from my own and expand my cultural horizons living as an expat in Germany. I'd also like to acknowledge the Deutsches Klimarechenzentrum (DKRZ), which provided the computational resources that allowed this doctorate thesis to be possible in the first place.

Thank you!

Author Contributions

Mihael M. de Souza Research Questions. Methodological Conception. Data Preparation. Numerical Simulations & Validation. Formal Analysis. Data Visualization. Writing, Editing & Review of Thesis and all Original Drafts.

Thomas Pohlmann Supervision & Resources. Research Questions. Methodological Conception. Editing & Review of Thesis and all Original Drafts.

Moritz Mathis Supervision. Methodological Conception. Editing & Review of all Original Drafts.

Bernhard Mayer Numerical Simulations (Technical Support). Editing & Review of Chapter [3](#) (Original Draft).

Maurício A. Noernberg Editing & Review of Chapter [3](#) (Original Draft).

Contents

List of Figures	12
List of Tables	19
1 Contextualization	20
1.1 Climate change in Brazil	21
1.2 Motivation and goal	24
1.3 Modeling framework	25
1.4 Research outline	27
2 Driving Mechanisms of the Variability and Long-term Trend of the Brazil-Malvinas Confluence during the 21st Century	29
2.1 Abstract	30
2.2 Introduction	30
2.3 Methods	33
2.3.1 The HAMSOM model	33
2.3.2 Model setup	34
2.3.3 Model output and data analysis	36
2.3.4 Gradient-boosting decision tree	37
2.4 Evaluation of model results	38
2.4.1 Temperature	38
2.4.2 Salinity	39
2.4.3 Surface circulation	40
2.4.4 Boundary current transport and the Brazil-Malvinas confluence	42
2.5 Results and discussion	44
2.5.1 The Brazil-Malvinas confluence southward drift	44

2.5.2	Response of the Malvinas Current to the Antarctic Circumpolar Current variability	46
2.5.3	Natural variability of the Brazil-Malvinas confluence	49
2.6	Conclusions	54
3	Possible Impacts of Anthropogenic Climate Change to the Upwelling in the South Brazil Bight	55
3.1	Abstract	56
3.2	Introduction	56
3.3	Methods	59
3.4	Results	61
3.4.1	Ensemble evaluation	61
3.4.2	Climatic impacts in the SBB	62
3.5	Discussion	65
3.5.1	The two upwelling regimes	65
3.5.2	Anthropogenic climate impacts to the upwelling regimes	71
3.6	Conclusions	77
4	Response of the Brazilian Shelf's Stratification to a Strong Warming Scenario	78
4.1	Abstract	79
4.2	Plain language summary	79
4.3	Introduction	80
4.4	Methods	82
4.4.1	Modeling framework	82
4.4.2	Data analysis	82
4.5	Results	84
4.5.1	Anthropogenic impact on stratification	84
4.5.2	Clustering impacts across the Brazilian shelf	85
4.6	Discussion	90

4.6.1	Shelf's stratification response to a strong warming scenario	90
4.6.2	Understanding the regional segmentation	93
4.7	Conclusions	96
5	Overall Assessment & Concluding Remarks	98
5.1	Model evaluation and historical performance	99
5.2	Forecasting anthropogenic climate impacts	102
5.3	Outlook and recommendations	105
	Bibliography	107
	Affirmation on Oath	121

List of Figures

1.1	Combined land and ocean surface temperature anomaly between 1850 and 2012. Adapted from IPCC (2014).	21
1.2	Bathymetry of the high resolution HAMSOM domain. The red box indicates the subdomain for the Brazil – Malvinas Confluence analysis (Chapter 2), the cyan box indicates the subdomain for the South Brazil Bight analysis (Chapter 3), and the black box indicates the subdomain for the Brazilian shelf analysis (Chapter 4). The dashed black line is the 200 m isobath and roughly represents the shelf break location.	26
2.1	Bathymetry of the HAMSOM domain. The red box indicates the subdomain for the Brazil – Malvinas confluence, the focus of our study. The two black transects at 29° and 45° S are the locations where the volume transport estimates for the Brazil and Malvinas currents were made. . . .	35
2.2	Sea surface temperature comparison between the WOCE/Argo Global Hydrographic Climatology (WAGHC - left) and HAMSOM (right) during austral summer (top) and winter (bottom), averaged over 1985 to 2016.	39
2.3	Zonally-averaged meridional temperature profile of the modelled domain based on the WOCE/Argo Global Hydrographic Climatology (WAGHC - top) and the HAMSOM model (center). At the bottom, the differences found between both datasets. All units are in °C and the red dash along the vertical axis indicates where the scale is fragmented to highlight the upper ocean (0 m to 500 m). Both datasets are averaged over 1985 to 2016. . . .	40
2.4	Sea surface salinity comparison between the WOCE/Argo Global Hydrographic Climatology (WAGHC - left) and HAMSOM (right) during austral summer (top) and winter (bottom), averaged over 1985 to 2016. . . .	41
2.5	Zonally-averaged meridional salinity profile of the modelled domain based on the WOCE/Argo Global Hydrographic Climatology (WAGHC - top) and the HAMSOM model (center). At the bottom, the differences found between both datasets. The red dash along the vertical axis indicates where	

	the scale is fragmented to highlight the upper ocean (0 m to 500 m). Both datasets are averaged over 1985 to 2016.	42
2.6	Surface mean kinetic energy (upper panels) and turbulent kinetic energy (bottom panels), in $\text{m}^2 \text{s}^{-2}$, calculated based on the binned surface drifter tracks from the Global Drifter Program (GDP - left) and HAMSOM's (right) u- and v-velocity components for the period between 2000 to 2016. The red ellipses in the bottom images highlights the location of the Zapiola anticyclone.	43
2.7	Monthly averages obtained from HAMSOM of the Brazil-Malvinas confluence latitudinal position (top), and of the Malvinas (middle) and Brazil (bottom) current transports in Sverdrups \pm one standard deviation. On the top panel, the dashed line indicates the overall average position of the confluence during the validation time window (1993 to 2008).	44
2.8	Time series of the Brazil-Malvinas confluence latitude (BMC) and the volume transports of the Malvinas and Brazil currents (at the transects defined on Fig. 2.1, based on HAMSOM) and the Antarctic Circumpolar current across the Drake Passage (based on MPI-ESM). The BMC is calculated based on the maximum temperature gradient over the 1000 m isobath, following the methodology from Goni et al. (2011), while the ACC is calculated based on the results from the MPI-ESM. The red line separates between the historical (1975 to 2009) and prognostic (2010 to 2100) periods, and the dashed lines are the calculated trends within those time intervals. The blue shade on the hist/RCP8.5 scenario represents HAMSOM's internal variability based on the five ensemble members.	45
2.9	Differences on sea level pressure (SLP – left) and zonal wind velocities (U - right) for the control (top) and hist/RCP8.5 (bottom) simulations based on results from the MPI-ESM. The differences reflect the change between the end of the 21 st century (2071 to 2100) and the historical period climatology (1981 to 2010).	47
2.10	Hovmoller diagram of the depth-integrated transport of the Antarctic Circumpolar Current across 47° W for the control (top) and hist/RCP8.5 (bottom) simulations based on results from the MPI-ESM. The black line represents the decadal variability of the Malvinas Current, after the application of a 10-years moving average on the time series from Fig. 2.8. The red line separates between the historical (1975 to 2009) and prognostic	

	(2010 to 2100) periods. All transports are in Sverdrups.	48
2.11	Comparison between the total ACC transport across 47° W and the Malvinas current transport across 45° S (see figure 2.1), calculated based on HAMSOM's (top) and the MPI-ESM (bottom) hist/RCP8.5 simulations. All transports are in Sverdrups (Sv). Bold lines represent the decadal variability on volume transports, and the blue shade on HAMSOM's scenario represents HAMSOM's internal variability based on the five ensembles. .	48
2.12	Decadal averages of sea surface temperature for the BMC region (red box in Fig. 2.1) on the 1980s, 2000s, 2030s, 2060s and 2090s, based on the hist/RCP8.5 simulation results from HAMSOM. The red dot represents the calculated confluence position within the designated decade based on the maximum temperature gradient over the 1000 m isobath. On the bottom right, the normalized confluence's seasonality within each decade. .	50
2.13	Normalized meridional latitude of the BMC (detrended) and the first and second expansion coefficients associated with the respective EOFs of the sea surface temperature, extracted based on HAMSOM's results. The region where the EOFs were extracted is indicated in Fig. 2.1 (red box).	51
2.14	Feature importance based on the three dominant features from each simulation (control and five ensemble members of the hist/RCP8.5).	52
3.1	Location of the South Brazil Bight, showing its bathymetry. The white dashed line marks the shelf break (200 m isobath).	60
3.2	T-S diagram of samples extracted along the SBB's shelf break for the Control and Hist/RCP8.5 scenarios. Samples related to the historical climatology (1980 to 2009) are represented by triangles, whereas samples related to the end of century climatology (2071 to 2100) are represented by squares. The color scheme represents the depth at which each data was extracted. The white cross is the centroid of each point distribution, for each evaluated period. Green, yellow and blue backgrounds portray the temperature and salinity boundaries for the Coastal Water, Tropical Water and South Atlantic Central Water, respectively.	62
3.3	Domain-averaged sea surface temperature (SST), mixed-layer depth (MLD) and upwelling velocity at the bottom of the mixed-layer (W_{upw}). Colored solid lines represent the different ensemble members, whereas the black	

	dashed line represents the median. The chosen domain is depicted in Fig. 3.1.	63
3.4	Historical climatology of the vertical velocity at the bottom of the mixed-layer (W_{MLD} - 1980 to 2009, left panels) for austral summer, winter and inter-annual scales and their respective projected change signals (EofC - Hist, right panels). Positive values for the climatologies indicate upward flow. Data is shown up to the 1000 m isobath, and the dashed white line identifies the 200 m isobath and marks the shelf break. Hashed regions in the projected change signals indicate where the difference is smaller than the control variability and therefore statistically not significant, and colors need to be interpreted in relation to the direction of the climatological flow. Arrows in the left panels represent the horizontal velocity field at the bottom of the mixed-layer. All values for the W_{MLD} are in meters per day.	64
3.5	Historical climatology of sea surface temperature (SST - 1980 to 2009, left panels) for austral summer, winter and inter-annual scales and their respective projected change signals (EofC - Hist, right panels). Data is shown up to the 1000 m isobath, and the dashed white line identifies the 200 m isobath and marks the shelf break. Hashed regions in the projected change signals indicate where the difference is smaller than the control variability and therefore not statistically significant. All values are in degree Celsius.	66
3.6	Historical climatology of the shelf's bottom temperatures (1980 to 2009, left panels) for summer, winter and inter-annual scales and their respective projected change signals (EofC - Hist, right panels). Data is shown up to the 1000 m isobath, and the dashed white line identifies the 200 m isobath and marks the shelf break. Hashed regions in the projected change signals indicate where the difference is smaller than the control variability and therefore not statistically significant. All values are in degree Celsius.	67
3.7	Historical climatology of sea surface salinity (SSS - 1980 to 2009, left panels) for austral summer, winter and inter-annual scales and their respective projected change signals (EofC - Hist, right panels). Data is shown up to the 1000 m isobath, and the dashed white line identifies the 200 m isobath and marks the shelf break. Hashed regions in the projected change signals indicate where the difference is smaller than the control variability and therefore not statistically significant.	68
3.8	Components of the potential vorticity conservation in the South Brazil	

	Bight calculated at the bottom of the mixed-layer for the inter-annual variability case during the historical period (1980 to 2009). Top figures are the relative vorticity (ζ , left) and its tendency (ζ_{XY} , right) and at the bottom are the absolute vorticity ($\zeta + f$, left) and the potential vorticity (Π , right). Streamlines over Π represent the flow, with the varying thickness as an indication of relative flow strength. Data is shown up to the 1000 m isobath, and the dashed white line identifies the 200 m isobath and marks the shelf break.	70
3.9	Top and middle panels show the wind speed climatology for the historical (1980 to 2009) and end of the century (2071 to 2100) periods over the subtropical South Atlantic, respectively. Bottom panel highlights the change signal between both periods. The black box represents the South Brazil Bight domain analyzed in this study (Fig. 3.1). The red filled contour around 30°S in the upper two panels marks the center of the South Atlantic Subtropical High (wind speeds less than 0.3 m s^{-1}). All values are in m.s^{-1}	72
3.10	Historical climatology of the offshore Ekman transport (1980 to 2009, left panels) of summer, winter and inter-annual scales and their respective projected change signals (EofC - Hist, right panels). Data is shown up to the 1000 m isobath, and the dashed white line identifies the 200 m isobath and marks the shelf break. Hashed regions in the projected change signals indicate where the difference is smaller than the control variability and therefore not statistically significant. All values are in $\text{m}^2.\text{s}^{-1}$	73
3.11	Historical climatology of the available potential energy (1980 to 2009, left panels) for summer, winter and inter-annual scales and their respective projected change signals (EofC - Hist, right panels). Data is shown up to the 1000 m isobath, and the dashed white line identifies the 200 m isobath and marks the shelf break. Hashed regions in the projected change signals indicate where the difference is smaller than the control variability and therefore not statistically significant. All values are in J.m^{-2}	75
3.12	At the top, Hovmöller diagram of the Brazil current transport (in Sverdrups) along the extension of the South Brazil Bight during the analyzed time period (1980 to 2100). At the bottom, differences between its climatological transport at the end of the century (EofC, 2071 to 2100) and the historical period (Hist, 1980 to 2009). The red solid line in the bottom graphic is the confidence interval calculated based on the control simulation. Samples within the red region are within our uncertainty range	

	based on the control. Negative differences indicate a strengthening of the BC transport whereas positive values indicate weakening, since the Brazil current flows southward.	76
4.1	Bathymetry along the Brazilian coastline (in meters). The shelf is sectioned in three sections to allow an easier visualization, and each lettered subplot is color-referenced on the general South America inset in subset A. For subplot C, the South Brazil Bight is the region between Cabo Frio and the Sta. Marta Cape, whereas the Southern Shelf extends beyond that to the end of the domain. The dotted line represents the 200 m isobath and marks the position of the shelf break.	83
4.2	Historical climatology and change signal for the austral summer (left panel) and winter (right panel) of the potential energy anomaly (ϕ_{PE} in J.m^{-3}) across the Brazilian shelf. Summer is defined as the averages for December, January and February, whereas for Winter is June, July and August. Warm (positive) values indicate increased stratification, whereas cold (negative) values indicates a shift towards well-mixed conditions. The shelf is sectioned in three sectors to allow an easier visualization, and each lettered sector is color-referenced on the general South America inset in subset A. The dotted line represents the 200 m isobath and marks the shelf break.	86
4.3	Historical climatology and change signal for the annual mean potential energy anomaly (ϕ_{PE} in J.m^{-3} , left panel) and the maximum pycnocline gradient ($\nabla \rho_{max}$ in kg.m^{-4} , central panel) and depth ($\nabla \rho_{depth}$ in m, right panel) across the Brazilian shelf. The shelf is sectioned in three sectors to allow an easier visualization, and each lettered sector is color-referenced on the general South America inset in subset A. The dotted line represents the 200 m isobath and marks the shelf break.	87
4.4	Cluster assignment using self-organizing maps (SOM) to model the change signal along the Brazilian shelf. Four test are shown, using 4, 6, 8 and 10 as the number of clusters to classify. The shelf is sectioned in three sectors to allow an easier visualization, and each lettered sector is color-referenced on the general South America inset in subset A (see Fig. 4.1). The dotted line represents the 200 m isobath and marks the shelf break.	88
4.5	Left axis show the time series of the potential energy anomaly (ϕ_{PE} in J.m^{-3} , black line), whereas the right axis show the trend ($\text{J.m}^{-3}.\text{year}^{-1}$, colored line) for each defined cluster. The trend is estimated with a one-year running window for every 30-year climatology between 1980 and 2100,	

	and referenced to the climatology's halfway year (e.g., 1994 for the period between 1980 and 2009). Red indicates higher stratification and blue indicates a shift towards more well-mixed conditions. Gaps are present where the trend is essentially zero. The dashed gray line represents the calculated historical average, considering the period between 1980 and 2009, and is related to the left axis.	89
4.6	Time series of the relative contribution of temperature (red, left axis) and salinity (right, blue axis) to the potential energy anomaly (in %) for each defined cluster. We would like to draw the readers' attention to both axes' ranges.	90
4.7	Mean and variance among model cells within each of the 6 clusters assigned by the SOM algorithm. Values are shown for the pycnocline strength and depth ($\nabla\rho_{max}$ in kg m^{-4} and $\nabla\rho_{depth}$ in m, respectively), sea surface temperature (SST in $^{\circ}\text{C}$), sea surface salinity (SSS) and potential energy anomaly (ϕ_{PE} in J m^{-3}).	91

List of Tables

2.1	Pearson correlation between the first and second expansion coefficients (EC) and the detrended time series of the meridional confluence position (BMC) and the volume transports of the Malvinas (MC) and Brazil (BC) currents. All correlations were significant with $p < 0.05$	52
-----	---	----

Chapter 1

Contextualization

1.1 Climate change in Brazil

Climate change studies have grown in importance over the last decade and been pushed to the forefront of discussions on environmental policies. Human influence cannot be overlooked any longer, as since the 1950s unprecedented changes are reported, and the atmosphere has experienced an average warming of 0.85°C , with the period between 2003 and 2012 undergoing a mean warming of 0.78°C . Ocean warming, specifically, dominates the increase in stored energy in the climate system, being responsible for 60% of the accumulated energy in the period from 1971 to 2010, for example. This is a direct consequence of changes in the radiative properties of the atmosphere through the emission of greenhouse gases (GHG) and aerosols, with the last three decades having been successively warmer than any previous decade since 1850 (Fig. 1.1 - IPCC, 2013, 2014). The consequences of anthropogenic climate change are even expected to accelerate after the end of the century (Randerson et al., 2015) under strong warming scenarios, emphasizing the importance of mitigating emissions in the long-term.

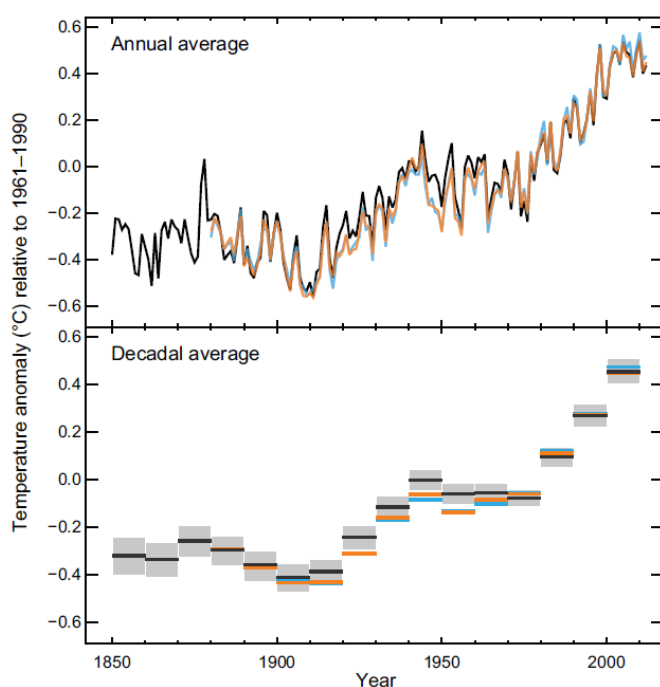


Figure 1.1: Combined land and ocean surface temperature anomaly between 1850 and 2012. Adapted from IPCC (2014).

Nevertheless, climate change can have pronounced regional variability which suggests different regional impacts within coastal systems (Marengo et al., 2012). In this light, the use of Regional Circulation Models (RCMs) to downscale climate effects and assess local impacts are the present days main tools (Holt et al., 2010; Marengo et al., 2012; Mathis and Pohlmann, 2014; Holt et al., 2018; Mathis and Mikolajewicz, 2020). The restricted, higher resolution, model domain of RCMs enables simulations to solve small-scale features at lower computational costs than global models (Snyder et al., 2003; Wang et al., 2010; Mathis et al., 2013), giving more information about regional/local impacts. For example, Liu et al. (2015) showed that for the Gulf of Mexico global models tended to overestimate

sea surface warming due to not being able to reproduce the weakening of the small scale Loop Current adequately. [Chou et al. \(2012\)](#) downscaled the HadCM3 results using the Eta-CPTec Model and were able to include small scale features into local climate patterns with close relation to observational data. [Cabré et al. \(2014\)](#) showed that the MM5 regional model, driven by the HadAM3H model, was able to reproduce the general features of present regional climate (precipitation and air temperature) adequately, although some bias was apparent. In essence, the use of these regional models enable scientists to refine our understanding of long-term climate impacts and provide more accurate predictions at regional levels.

In Brazil, a specific network has been created in 2007 to tackle anthropogenic climate change (Rede CLIMA). This network is devoted to the development of a local ESM, the Brazilian Earth System Model ([Nobre et al., 2012b](#)), and to evaluate the possible impacts of climate change on Brazil's economic and social aspects, as well as the expected impacts on the different natural environments (e.g., oceans, the coast, the tropical forests - [Arraut et al., 2013](#)). [Nobre \(2008\)](#) found evidence of a 1 °C increase in minimum temperatures, as well as a 0.75 °C increase on mean temperatures in the last 50 years, with reports indicating increased natural disasters and aridization of the northeastern part of Brazil. Since then, studies focused on the consequences of global warming to the Brazilian biomes and climate in general ([Lacerda and Nobre, 2010](#)).

In 2014, the PBMC (Painel Brasileiro de Mudanças Climáticas) published its first national assessment report (RAN - [PBMC, 2014](#)), following the structure of the IPCC's AR. It relies mostly on results and scenarios of the 4th AR and describes the expected impact of anthropogenic climate change to the Brazilian continental biomes. According to the RAN, the northern and northeastern regions are considered the most vulnerable, as decreases in precipitation are above global averages. The reduced precipitation seems to be triggered by a smaller moisture transport from the ocean towards the coast due to changes in wind patterns, brought about by increased sea surface temperatures. The consequences to the biomes can be summarized as follows:

- **Amazon** 40% to 45% decrease in precipitation and surface temperatures increases by up to 6 °C. Deforestation can accentuate these impacts, affecting the hydrological cycle and extending the dry season.
- **Caatinga** Up to 50% decrease in precipitation and increase in surface temperatures between 3.5 °C and 4.5 °C. Can lead to the desertification of this biome.
- **Cerrado** 35% to 45% decrease in precipitation and highest increase in surface temperatures (up to 5.5 °C). The seasonal variability within this biome is also expected to increase.

- **Pantanal** 35% to 45% decrease in precipitation and increase in surface temperature up to 4.5 °C.
- **Mata Atlântica** Highest decrease in precipitation in the northeastern portion of the biome (up to 35%), as opposed to the south/southeastern regions (up to 30%). Increase in surface temperature up to 4 °C.
- **Pampa** Only region with predicted increase in precipitation (up to 40%) and smallest increase in surface temperatures (up to 3 °C).

Similar results were also found by [Ramos da Silva and Haas \(2016\)](#) using a set of nested grids that allowed for a better representation of regional effects, increasing the confidence over these predictions. [Nobre et al. \(2012a\)](#) showed that a coupled ocean-atmosphere regional model was necessary to adequately reproduce the feedback mechanism between the sea surface temperature (SST) and the intensity of the South Atlantic Convergence Zone (SACZ), which tends to be underrepresented by global models. [Marengo et al. \(2012\)](#) focused on the SRES A1B scenarios to evaluate the effects of future climate projections on the river basins of the Amazonas, São Francisco and Paraná rivers, and found an overall reduction on precipitation rates in all basins as well as an increase in air temperature, and an overall weakening of the SACZ during austral summer.

Towards the coast, [Martins et al. \(2017\)](#) found changes in the profile of incoming significant wave heights along the Pernambuco coastline under a large sea level rise scenario (1 m), increasing the coastal vulnerability of the more exposed sections of the shoreline. Similar effects to the wave characteristics is also expected at the Santos Harbor in southeast Brazil ([Alfredini et al., 2014](#)). And in the south, both under the low and high emissions scenarios, [de Figueiredo et al. \(2018\)](#) found that coastal erosion would be mainly controlled by sea level rise as opposed to the sedimentary budget. According to their study, under continued emissions, coastal recession risk could be eight times higher than present rates. Not all results are essentially negative, though, as [Pereira et al. \(2013\)](#) found that global warming could increase wind power density along northeastern Brazil's coast.

Physical conditions along the Brazilian shelf will respond to changes on the atmospheric circulation over the tropical and subtropical South Atlantic, with the Northern Brazil Current and the Brazil Current acting as the interface between shelf waters and the deep ocean. With that mind, the South Atlantic Subtropical High is expected to migrate southward during the 21st century ([Rykaczewski et al., 2015](#); [Reboita et al., 2019](#)), as it adjusts to a more southern position of the westerlies ([Swart and Fyfe, 2012](#); [Wilcox et al., 2012](#); [Barnes and Polvani, 2013](#)) and to the widening of the Hadley cell ([Davis and Rosenlof, 2012](#); [Kang and Lu, 2012](#); [Hu et al., 2018](#)). This southward migration of the westerlies is also expected to increase the strength of the Agulhas Leakage ([Biastoch et al., 2009](#)) and the alongshore wind speeds over the subtropical South Atlantic ([Sydeman et al., 2014](#)).

Still based on ESMs, [Pontes et al. \(2014\)](#) carried out a multi-model reanalysis of results for the RCP8.5 scenario within the 5th AR and found a 40% increase in the Brazil Current volume transport south of 30°S and a southward migration of the Brazil-Malvinas Confluence of $\approx 1.2^\circ$ at the end of the century. Finally, [Toste et al. \(2018\)](#) downscaled results from HadGEM2-ES for the RCP4.5 scenario along the central and southeast Brazilian coastline, simulating two 10-year time slices (1995 and 2005 and 2090 and 2100). They found a smaller increase of the Brazil Current transport (17.5%) accompanied by a slight northward migration of its geographical origin, a mean sea surface temperature increase of 1.44 °C and a mean sea level rise of 0.78 m. But more importantly, their results showed substantial spatial heterogeneity along the coast, while results derived from Earth System Models (ESMs) tend to be homogeneous ([Capotondi et al., 2012](#); [IPCC, 2013](#); [Fu et al., 2016](#)). This highlights the importance of regional downscaling experiments when identifying the impacts associated with anthropogenic climate change along the Brazilian coastline.

1.2 Motivation and goal

The impacts of anthropogenic climate change to coastal regions is much more nuanced than global projections would suggest when regional processes are considered, as multiple studies have shown ([Snyder et al., 2003](#); [Holt et al., 2010](#); [Wang et al., 2010](#); [Marengo et al., 2012](#); [Mathis et al., 2013](#); [Praveen et al., 2016](#)). And this is also true along the Brazilian coastline, as the downscaling experiments from [Toste et al. \(2018\)](#) demonstrated. However, their study was limited, both in the spatial (central and southeastern Brazil) and temporal (two 10-year time slices) scales. A more complete analysis, exploring the effects of increased emissions on a climatological scale and along the whole coastline, remains as an open research question.

Approximately 25% of the Brazilian population lives along a coastline 8000 km long ([IBGE, 2011](#)). Along its shelf seas, the presence of crude oil deposits and a large reliance on fisheries at the industrial (southeastern and south regions) and artisanal (north and north-east regions) scales highlight its large economic and social importance ([Castro et al., 2006](#)). Fisheries, specially, are intrinsically connected to the ecosystem's health and will responds to changes in the dynamical forcings due to anthropogenic climate change, as was demonstrated by [Harley et al. \(2006\)](#). As an example, the intrusion of the colder and nutrient-rich South Atlantic Central Water has been shown to fuel primary production in south(east) Brazil ([Brandini et al., 2014](#)), being correlated to high zooplankton biomass ([Resgalla Jr et al., 2001](#)). This shelf intrusion, in turn, is essentially a response to surface Ekman forcing and shelf break processes ([Castro and Miranda, 1998](#); [Campos et al., 2000](#)), which depends on the overlaying atmospheric circulation and will be affected by the southward migration

of the South Atlantic gyre.

On a broader scale, the thermodynamical characteristics of the South Atlantic Central Water is dependent on the physical state of the water column at the Brazil-Malvinas Confluence, where this water mass is formed (Gordon, 1981; Sprintall and Tomczak, 1993). Changes in this region, therefore, can have an indirect impact in the Brazilian shelf's fertilization. Furthermore, sea surface temperature dipoles created around the Confluence have also been linked to the interannual variability of the South Atlantic Convergence Zone (Robertson and Mechoso, 2000), which influences precipitation in southeast Brazil. Even on more general terms, sea surface temperature variability has a strong correlation with overall precipitation over land (Nobre et al., 2012a), which directly affects crop yields.

Within this context, a proper understanding of anthropogenic climate change impacts' on the physical conditions of the Brazilian shelf requires the consideration of these large scale phenomena over the South Atlantic Ocean, combined with the representation of regional shelf processes. Our goal is to establish a modeling framework that takes into account both the aforementioned spatial scales. This can then be used to more accurately estimate the expected impacts of increased GHG emissions along the Brazilian shelf over the 21st century, hopefully acting as a basis for future adaptation measures, which are inherently regional steps.

1.3 Modeling framework

Our modeling framework employs the one-way coupling between the Max-Planck Institute – Earth System Model Mixed Resolution (MPI-ESM-MR - Giorgetta et al., 2013; Jungclaus et al., 2013) and a high-resolution domain of the South Atlantic Ocean implemented using the Hamburg Shelf Ocean Model (HAMSOM - Backhaus, 1985; Pohlmann, 1996, 2006). Our goal with this coupling is to analyze the upper-bound impacts of anthropogenic climate change, and put those results in perspective against natural conditions (i.e., without human influence). To accomplish this goal, we utilize results for the Representative Concentration Pathway (RCP) 8.5, which is a very high baseline anthropogenic-driven emission scenario with rising radiative forcing throughout the 21st century (van Vuuren et al., 2011). In this light, our simulations relied on both the combined Historical (1950 to 2005) + RCP8.5 (2006 to 2100) and the PI-Control (1950 to 2100) scenario runs (IPCC, 2014), for the anthropogenic and natural case studies, respectively.

Our HAMSOM application has a horizontal resolution of $1/12^\circ$ (≈ 10 km) and spans the region between 10°N and 54°S and between South America and Africa (19°E , Fig. 1.2). It has 28 vertical layers and a minimum surface depth of 5 m (lower bound depths at: 5 m, 15 m, 25 m, 40 m, 55 m, 75 m, 100 m, 140 m, 200 m, 280 m, 380 m, 500 m, 640 m, 800 m,

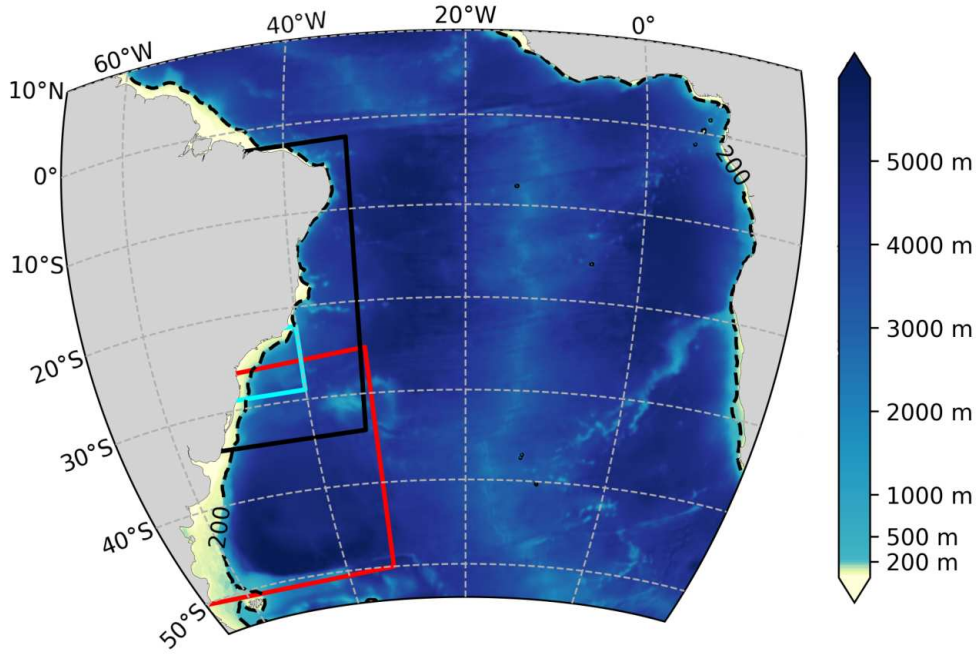


Figure 1.2: Bathymetry of the high resolution HAMSON domain. The red box indicates the subdomain for the Brazil – Malvinas Confluence analysis (Chapter 2), the cyan box indicates the subdomain for the South Brazil Bight analysis (Chapter 3), and the black box indicates the subdomain for the Brazilian shelf analysis (Chapter 4). The dashed black line is the 200 m isobath and roughly represents the shelf break location.

990 m, 1200 m, 1440 m, 1710 m, 2000 m, 2340 m, 2680 m, 3070 m, 3510 m, 4000 m, 4550 m, 5100 m, 5700 m and 6300 m), arranged on the staggered Arakawa-C grid. This vertical discretization is aimed at properly resolving the upper ocean flow but with a crude resolution of the deep circulation. With respect to the time scale, our simulation encompassed the period between 1975 to 2100 with a 25 years spin-up phase (between 1950 and 1974) to adjust the internal baroclinic fields to the boundary forcing. Time step during simulations was of 180 s.

At the surface, HAMSON requires input data of 2 m air temperature, sea level pressure, near-surface relative humidity, cloud cover, total precipitation and 10 m wind speed, which were extracted from the atmospheric component of the MPI-ESM (ECHAM6 - [Stevens et al., 2013](#)). At the lateral open boundaries, it requires input data for the sea surface height and 3D temperature and salinity profiles. 3D temperature and salinity profiles are also required to initialize the baroclinic model domain. In both cases, information was extracted from the ocean component of the MPI-ESM (MPIOM - [Jungclauss et al., 2013](#)). Systematic deviations in these input forcings, both for the atmosphere and the ocean, were corrected following the procedure described by [Mathis et al. \(2013\)](#) to ensure that they reflect the mean state of our current climate. In the case of the atmosphere, this bias correction was performed using the NCEP/NCAR reanalysis ([Kalnay et al., 1996](#)), whereas

SODA model data (Carton and Giese, 2008) was used for the ocean properties. Finally, freshwater inflow was obtained from the MPI-ESM and corrected based on WaterGAP model data (Döll et al., 2003).

A total of six simulations were performed, for the full analysis period. One of those simulations was reflective of the PI-Control conditions and is considered our control run. The remaining five simulations are all reflective of the combined Historical + RCP8.5 scenarios. At each of those simulations, however, initial conditions in the temperature and salinity fields were randomly modified within 1% of their base values. This is done to account for the internal variability of our modeling framework, providing a measure of uncertainty for our simulations. At the end, results from each simulation were stored as daily averages and consists of outputs for sea surface height, temperature, salinity and zonal and meridional current velocities.

1.4 Research outline

As demonstrated in section 4.6.1, the Brazilian shelf responds to regional process (e.g. Ekman and shelf-break upwelling, Plata plume dynamics) and large scale shifts in atmospheric and ocean dynamics over the South Atlantic Ocean. For this reason, our regional model domain comprehends the whole South Atlantic and aims to locally resolve the flow around the South Atlantic Subtropical High, and its consequences to the wind stresses along the Brazilian coastline and to the Brazil Current. With that in mind, we chose to take a process-driven approach when evaluating the impacts associated with anthropogenic climate change, using a strong warming scenario (RCP8.5) as our benchmark.

Chapter 2 explores the expected changes to the position and variability of the Brazil-Malvinas Confluence (red contour, Fig. 1.2). This is a region of high ocean productivity and strong mesoscale activity (Piola et al., 2000; Piola and Matano, 2017). It is not only responsible for the formation of the South Atlantic Central Water that is transported by the Northern Brazil Current and the Brazil Current (Gordon, 1981; Sprintall and Tomczak, 1993), but has also been linked to the position of an ocean front over the south Brazilian shelf (Piola et al., 2000). Over the last decade, studies have identified a poleward shift of its mean meridional position, correlating this behavior to changes in the latitude of separation of the Brazil Current (Goni et al., 2011), a southward migration of the latitude of maximum wind curl (Lumpkin and Garzoli, 2011), and to a weakening of the Malvinas Current (Combes and Matano, 2014b).

Pontes et al. (2014), when analyzing ESMs, found that this trend would even persist throughout the 21st century. Although they also found a decrease in the Malvinas Current over the same time scale, they did not find changes to the Antarctic Circumpolar Current

that could explain this weakening, nor did they analyze a control simulation to exclude the possibility of natural oscillations. As for the behavior of the Antarctic Circumpolar Current, ESMs show an inconsistent response to anthropogenic climate change (Gupta et al., 2009; Wang et al., 2011; Downes and Hogg, 2013), which raises questions in regards to the Malvinas Current long term response. To this effect, our goal in this chapter is to investigate the reasons behind the poleward shift of the Brazil-Malvinas Confluence, its possible relation to changes in the Antarctic Circumpolar Current, and whether this could be a reflection of natural variability or a direct impact of human influence.

Chapters 3 and 4 are focused on the effects of regional processes along the Brazilian shelf. Over the shelf, several water masses play a role in shaping its dynamics. Tropical Water ($>20^{\circ}\text{C}$ in temperature and >36.6 in salinity) dominates the surface layer and is transported in the first 200 m of the Northern Brazil Current and the Brazil Current. Closer to coastal systems (e.g., estuaries), the dilution of Tropical Water by the local freshwater inflow creates the Coastal Water, identifying region of freshwater influence. Just below the Tropical Water in both western boundary currents, South Atlantic Central Water ($<20^{\circ}\text{C}$ in temperature and <36.6 in salinity) generated at the Brazil-Malvinas Confluence is found (Castro et al., 2006; Piola et al., 2018). Additionally, over the southeastern and southern shelves, the equatorward intrusion of a freshwater plume associated with the Plata River discharge is also present, with the latitude of its intrusion dependent on southwesterly wind anomalies mainly driven by the passage of cold atmospheric fronts (Piola et al., 2000, 2005; Pimenta et al., 2005). The interplay of these water masses drives the stratification over the Brazilian shelf and is explored in Chapter 4, as we investigate changes to the pycnocline and the potential energy anomaly at the end of the century (black contour, Fig. 1.2).

Finally, the dynamics surrounding the intrusion of South Atlantic Central Water is an important fertilization mechanism of shelf waters along the Brazil Current pathway (Castro et al., 2006), specially over the South Brazil Bight (cyan contour, Fig. 1.2). In this region, this colder water mass intrudes along the shelf through two different physical mechanisms, driven by the Ekman forcing (Lima et al., 1996; Castro and Miranda, 1998; Castelao et al., 2004) and by shelf break interactions along the Brazil Current pathway (Campos et al., 1995, 2000; Silveira et al., 2000; Palma and Matano, 2009). The South Atlantic Central Water affects the northern sector of the South Brazil Bight year-round (Campos et al., 2000; Palma and Matano, 2009; Cerda and Castro, 2014), while having a stronger seasonal variability over the rest of the bight (Möller et al., 2008; Castro, 2014; Brandini et al., 2014). Understanding how anthropogenic climate change can impact the South Atlantic Central Water intrusion over a region under such a diverse dynamical setting highlights the importance of regional processes when evaluating future impacts and is explored in Chapter 3.

Chapter 2

Driving Mechanisms of the Variability and Long-term Trend of the Brazil-Malvinas Confluence during the 21st Century

This chapter has been published in *Climate Dynamics*:
de Souza MM, Mathis M, Pohlmann T (2019) Driving mechanisms of the variability and long - term trend of the Brazil – Malvinas confluence during the 21st century. Clim Dyn 53:6453–6468, doi: <https://doi.org/10.1007/s00382-019-04942-7>
<https://link.springer.com/article/10.1007/s00382-019-04942-7>

2.1 Abstract

Over the last decade, several studies have identified a southward drift of the mean meridional position of the Brazil-Malvinas confluence (BMC). Although this trend has been ascribed to different mechanisms, the most recent study found a reduction of the Malvinas current (MC) as the main reason behind it. It is unclear, however, how this mechanism would persist in the face of global warming and under projected increased winds over the Southern Ocean, as the response of the Antarctic Circumpolar Current (ACC) varies within different Earth System Models (ESM), ultimately impacting the MC. We ran a high-resolution ($1/12^\circ$) ocean model driven with results from the Max-Planck-Institute – ESM to verify how the confluence will respond to anthropogenic climate change, by downscaling results from the pre-industrial control and RCP8.5 scenarios. Our results show that the southward confluence shift is only persistent under anthropogenic forcing and is led by a reduction of the MC volume transport. This reduction of the Malvinas transport is induced by a shift of the main ACC flow closer to Antarctica's shelf, in response to a southward movement of the westerlies band, even if no long-term changes on the total ACC transport can be found. Our results corroborate previous evidence regarding the MC as the main responsible behind the observed BMC southward shift of the recent past but points toward anthropogenic climate change as the triggering mechanism, with various effects cascading from its impact on the Southern Ocean. This also has consequences for the BMC variability, whose amplitude reduces as we approach the end of the 21st century.

2.2 Introduction

The upper ocean circulation in the western South Atlantic is dominated by the Brazil-Malvinas Confluence's (BMC) dynamics. In this region, warm water carried by the Brazil Current (BC) from the tropics is met by colder and fresher water carried by the Malvinas Current (MC) from subpolar origins, creating a region of high potential vorticity and a strong eddy field (Piola and Matano, 2017). Satellite imagery of this region shows high chlorophyll-a concentrations, which are a consequence of both the mesoscale activity and the thermohaline structures at this frontal zone (Piola et al., 2000; Piola and Matano, 2017). Rings shed from both currents on the confluence region may affect the formation of water masses, influence the ventilation of the local thermocline and play a role on the distribution of heat and salt over the South Atlantic (Gordon, 1981; Campos et al., 1999a). Based on results from the Simple Ocean Data Assimilation (SODA - Carton and Giese, 2008), Yang and He (2014) proposed that changes in the upward eddy buoyancy flux on the decadal time scales might be related to the freshening/cooling of the Antarctic Intermediate Water, which spreads to all major ocean basins. In relation to the atmosphere, Robertson and Mechoso (2000) suggests that the sea surface temperature (SST) dipole created around

the BMC may act as a source of interannual variability of the South Atlantic Convergence Zone due to thermal inertia of the upper ocean, which influences precipitation in southeast Brazil.

Considering this widespread influence, understanding the BMC's variability across different time scales is an important factor in understanding the general dynamics in the western South Atlantic. On the annual and semi-annual scales, [Matano et al. \(1993\)](#) demonstrated the importance of the BC and the seasonality of the gyre-scale mass transport through a study combining modeling and altimetry data. They estimated the intra-annual variability of the BMC mean latitudinal position to be around 2° with a maximum northward and southward displacement during austral winter and austral summer, respectively, showing its correlation to the zonally-averaged wind stress curl. [Wainer et al. \(2000\)](#) showed a similar behavior on the intra-annual scale using a coupled ocean-atmosphere model, but also found a significant variability on the interannual scale and lower frequencies when tracking the maximum incursions of the 24°C and 17°C isotherms, related to the BC and MC respectively. [Zavialov et al. \(1999\)](#) used a blended set of historical SST data in the region to focus on the lower frequency variability between 1854 and 1994. Although limited to winter data, they showed that the maximum northward incursion of the 17°C isotherm had a significant decadal component and exhibited a general southward trend. Meanwhile, a general warming secular trend since 1940 was found in the confluence domain.

Since then, several studies have identified this southward trend on the BMC's mean meridional position, based on modeling studies, surface drifters and altimeter data ([Goni et al., 2011](#); [Lumpkin and Garzoli, 2011](#); [Combes and Matano, 2014b](#)). [Goni et al. \(2011\)](#) identified a southward shift of the confluence from its previous mean latitude in the range of 1.5°S between 1993 and 2008. Although they could not conclusively relate this shift to changes in transport of the BC or MC, they identified a change in the dominant periodicities from an annual to a bi-annual signal. [Lumpkin and Garzoli \(2011\)](#) analyzed the same years as [Goni et al. \(2011\)](#) and also found no long-term trends on the transports of both forcing currents. They found, however, a correlation between this southward BMC migration and the maximum basin-averaged wind stress curl. This could indicate that this southward shift might also respond to the South Atlantic Gyre strength and location on lower frequencies, similar to how a correlation was found by [Matano et al. \(1993\)](#) on the seasonal time scale. Furthermore, they suggested that the correlations found between the mean confluence position and the SST fluctuations in the area might point towards the Agulhas Leakage as a forcing mechanism. [Combes and Matano \(2014b\)](#) used a high-resolution coupled regional model approach to fully comprehend the behaviour of the BMC in response to variations on the BC and the MC as well as the atmospheric forcing. Their model results suggest that this southward shift happened mostly abruptly during 1999-

2000, as opposed to a steady trend. This shift seems to be driven by a weakening of the Southern Ocean circulation, as no significant change in the maximum wind stress curl was found in the 1998-2002 period. This would signify that changes in the MC transport are responsible for the southward drift, responding to variations of the Antarctic Circumpolar Current (ACC). Nevertheless, both [Combes and Matano \(2014b\)](#) and [Lumpkin and Garzoli \(2011\)](#) mention the incoherent response of the MC and the Southern Ocean circulation to the apparent overall strengthening of the westerlies demonstrated by the Southern Annular Mode index (SAM - [Marshall, 2003](#)). To this point in particular, [Combes and Matano \(2014b\)](#) showed a weakening of the westerlies over the South Atlantic portion of the Southern Ocean after the 2000s that could justify the abrupt BMC shift.

It is important to note, however, that the response of the ACC to increased greenhouse gas concentrations is not consistent in future climate projections, showing a large scatter across a broad range of Earth System Models ([Gupta et al., 2009](#)). [Wang et al. \(2011\)](#) analyzed results from the Intergovernmental Panel on Climate Change (IPCC) Fourth Assessment Report (AR4) and found that the poleward shift of the subtropical gyres could lead to a narrowing of the ACC, which would limit the increase in the barotropic mass flow and reduce the transport of the ACC's northern flank. They also found a dependence of the ACC transport on the model's stratification at high latitudes. In several models, increased wind speeds over the Southern Ocean led to enhanced parametrized eddy-induced transport. This tends to flatten isopycnal surfaces and reduce the upper layer meridional gradients, weakening the ACC. In a more recent paper based on models from the AR5, [Downes and Hogg \(2013\)](#) found these buoyancy fluxes to dominate the response of the ACC in compensating wind stresses. In this context, the incoherent ACC response to the increased SAM index found by [Combes and Matano \(2014b\)](#) may be realistic. Their found dependency between the BMC's south drift and the weakening of the MC might be a robust feature even in the face of a strengthening atmospheric circulation over the Southern Ocean. If this is the case, ultimately, the observed BMC southward migration might be a response to increased greenhouse gas emissions and a large-scale reflection of global climate change.

In this light, our goal is to determine whether the previously reported net southward displacement of the BMC can be attributed to anthropogenic climate change. Furthermore, we aim to discern what effects this man-made contribution might have had to the general variability in the Brazil-Malvinas confluence region and try to separate the contribution of different forcing mechanisms to the confluence's low-frequency variability. To this end, we utilize a regional, high-resolution ocean model of the South Atlantic forced by results from the global Earth system model MPI-ESM ([Jungclaus et al., 2013](#)). By analysing a scenario under a strong climate signal (RCP8.5) and comparing it to a scenario forced by pre-industrial control conditions, we show how this robust southward trend on the BMC

is related to increased greenhouse gas emissions due to changes in the Antarctic Circumpolar Current main pathway. Subsequently, we utilize a gradient-boosting decision tree algorithm to distinguish between the contributions of the BC and MC currents, as well as different local and remote forcing mechanisms, to the confluence's natural variability.

2.3 Methods

The model system we employed for our study consists of a high-resolution model covering our region of interest and a general circulation model, which provides boundary and atmospheric forcing data. The latter information for the large-scale state of both the ocean and the atmosphere is derived from the coupled MPI-ESM (Max-Planck Institute – Earth System Model) simulations in mixed resolution (MR) performed for the Coupled Model Intercomparison Project phase 5 experiments (CMIP5) (Giorgetta et al., 2013; Jungclauss et al., 2013). For the high-resolution domain, the Hamburg Shelf Ocean Model (HAMSOM) is utilized as described below. Our test cases are based on simulations for the representative concentration pathway 8.5 (RCP8.5) combined with the MPI-ESM historical run (Hist) and the pre-industrial run (control), according to the definitions from the IPCC (2014). Using these contrasting scenarios allows us to address an upper bound limit to these anthropogenic effects among the IPCC RCPs. Initial conditions were extracted from the MPI-ESM ocean component. In the case of the Hist/RCP8.5 scenario, five ensemble members of the whole simulation period were produced. For each ensemble member, the initial 3D temperature and salinity fields of HAMSOM were randomly modified within 1% of their base values to account for HAMSOM's internal variability, while the forcing from the parent global model remained unchanged.

The atmospheric forcing data is derived from the atmospheric component (ECHAM6) of MPI-ESM (Stevens et al., 2013) and utilizes inputs for 2 m air temperature, sea level pressure, near-surface relative humidity, cloud cover, total precipitation and 10 m wind speed. These outputs were available as 6-hourly (air temperature, sea level pressure and 10 m wind speed) and daily (cloud cover, total precipitation and near-surface relative humidity) data and linearly interpolated to HAMSOM's timestep of three minutes. Oceanic boundary conditions are derived from the ocean component (MPIOM - Jungclauss et al., 2013) and corresponds to the sea surface height and 3D temperature and salinity profiles. These outputs were available as monthly means and were also linearly interpolated to the model time step, considering the monthly value at the middle of the pertaining month.

2.3.1 The HAMSOM model

HAMSOM is a three-dimensional, baroclinic, free surface, shallow-water equations model. It relies on the hydrostatic and Boussinesq approximations and is defined based on Z-

coordinates on the staggered Arakawa C-grid. To allow for more lenient time steps, it solves the terms describing gravity waves in the shallow-water equations and the vertical diffusion of momentum, temperature and salinity implicitly (Backhaus, 1985). The advection of temperature and salinity is formulated with a second order Lax-Wendroff scheme (Daewel and Schrum, 2017), while the advection of momentum is formulated using the component upstream method. The semi-implicit formulation leads to an elliptical partial differential equation that is solved using the SOR “red-black” method (Pohlmann, 2006). Still according to Pohlmann (2006), the vertical eddy viscosity is parameterized using the Kochergin (1987) method and is dependent on the vertical velocity gradient and the water column stability. A full description of this parametrization and its adaptation to the HAMSOM model can be found in Pohlmann (1996). The Smagorinsky scheme (Smagorinsky, 1963) is employed for the horizontal viscosity and is based on the horizontal velocity shear.

Regarding the boundary behavior, closed boundaries are defined under a semi-slip and zero flux condition. At open boundaries a zero gradient is enforced and a Sommerfeld radiation scheme is applied for outflowing temperature and salinity. River inflow is treated as a temperature, salinity and volume change at the respective model cell. Surface exchange flows are calculated through bulk-formulas and a quadratic stress law is applied at the bottom boundary (Pohlmann, 2006).

2.3.2 Model setup

The model domain comprises the South Atlantic Ocean between South America and Africa (10° N and 54° S and 69° W and 19° E, approximately, Fig. 2.1). This model has a horizontal resolution of 1/12° with 28 vertical layers and a minimum depth of 5 m (lower bound depths at: 5 m, 15 m, 25 m, 40 m, 55 m, 75 m, 100 m, 140 m, 200 m, 280 m, 380 m, 500 m, 640 m, 800 m, 990 m, 1200 m, 1440 m, 1710 m, 2000 m, 2340 m, 2680 m, 3070 m, 3510 m, 4000 m, 4550 m, 5100 m, 5700 m and 6300 m). The choice to limit the model’s southern boundary and not to locally resolve the ACC inside the domain was twofold: first, we could not fully resolve the ACC due to only simulating a portion of the Southern Ocean; second, due to the lack of ice dynamics in HAMSOM. The first point would mean that we still incorporate the ACC flow from the MPI-ESM via the Drake Passage. The second would mean that buoyancy modifications that could affect the ACC due to the warming climate could not be properly considered and were shown to be dominant by Downes and Hogg (2013) on this large-scale current. Since properly resolving the ACC would require a fully coupled global model, we choose to rely on the boundary response of the MC from the global model, which could take a greater range of parameters into account, and fully resolve the flow over the South Atlantic. The vertical discretization is aimed at properly resolving the upper ocean flow but with a crude resolution of the deep circulation. The sep-

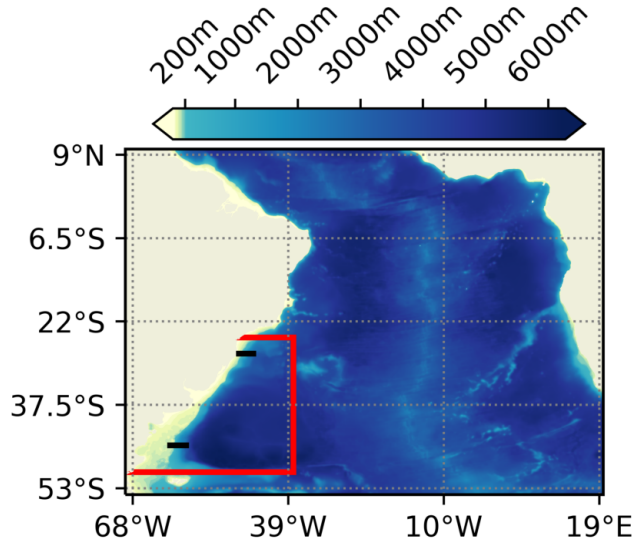


Figure 2.1: Bathymetry of the HAMSON domain. The red box indicates the subdomain for the Brazil – Malvinas confluence, the focus of our study. The two black transects at 29° and 45° S are the locations where the volume transport estimates for the Brazil and Malvinas currents were made.

aration depth at the lower bounds also takes into account the transition between different water masses, namely the Tropical Water (upper 50 m), the South Atlantic Central Water (500 m), the Antarctic Intermediate Water (1200 m), the North Atlantic Deep Water (4000 m) and the Antarctic Bottom Water (Campos et al., 1999a). The horizontal viscosity is parametrized (as discussed above) and ranges between $10^2 \text{ m}^2 \text{ s}^{-1}$ to $10^4 \text{ m}^2 \text{ s}^{-1}$, while the vertical viscosity ranges between $10^{-5} \text{ m}^2 \text{ s}^{-1}$ to $10^{-2} \text{ m}^2 \text{ s}^{-1}$.

The simulation comprehends the period from 1975 to 2100 and a spin-up between 1950 and 1974. This spin-up is necessary to ensure a stable potential energy field in the domain due to the employed bias correction of the atmospheric and oceanic forcing data at the open boundaries, and to let the boundary conditions adapt to the higher resolution domain and the regional ocean model. This still provides us 35 years during the historic period (1975 to 2009) and an 90 years prognostic period (2010 to 2100). The choice of the period between 2009 and 2010 to separate between historical and prognostic time scales was defined based on the end period applied during the bias correction, explained below.

To account for systematic deviations in the forcing data, both the atmospheric and ocean boundary data were corrected using bias masks. For the control simulation, this translates into the introduction of anthropogenic climate change in its mean state variables, as perceived by the currently available climatologies used to correct this data. This means that, at the end of the historical period, both the hist/RCP8.5 and the control have an equivalent mean state that is reflective of our current climate. As both scenarios develop under the prognostic period, however, the climate signal is stable in the control whereas it continuously increases in the hist/RCP8.5. All atmospheric data were corrected using NCEP/NCAR reanalysis data (Kalnay et al., 1996). Sea surface height is corrected at the boundaries using AVISO satellite data and the 3D temperature and salinity profiles are corrected using SODA results (Carton and Giese, 2008). A ten years average of monthly

model data (2000 to 2009) is compared with the reanalysis data based on a geospatial grid. A spatially variable 2D map and profiles at every active boundary (north, south and east) are created for the twelve months, containing the deviations between both data sources. These deviation profiles are then linearly interpolated in time and added to every boundary forcing over the full simulation period, except for the wind speed corrections. In the case of the wind speed, the bias mask was applied multiplicatively to correct only for the proper average magnitudes and avoid disturbing the spatial patterns. This type of bias correction to forcing fields coming from lower resolution models has also been performed on other downscaling experiments (Gabioux et al., 2013; Mathis et al., 2013). The freshwater inflow from continental sources is also obtained from MPI-ESM and corrected based on the results of the WaterGAP model for the whole domain (Döll et al., 2003). For reference, the averaged (\pm one standard-deviation) Amazon and La Plata river discharges were $44\,449.3 \pm 3633.2 \text{ m}^3 \text{ s}^{-1}$ and $6935.6 \pm 1076.2 \text{ m}^3 \text{ s}^{-1}$, respectively, integrated over one historical climatology (1980 to 2009).

2.3.3 Model output and data analysis

HAMSOM's main output consists of daily averages of sea surface height, temperature, salinity and zonal and meridional current velocities. Since our focus is on understanding the interannual to decadal variability on the Brazil-Malvinas confluence, we filter out all intra-annual variability to better highlight the desired scales. First, all data is monthly-averaged. Second, a 12-months running mean filter is applied. All proceeding methods are applied on these filtered time series. When detrending is necessary, e.g. before extracting empirical orthogonal functions (EOFs), a least-square fit is utilized and applied on the historical and prognostic periods independently. As a representative of the confluence's dynamics, the mean confluence position was calculated following Goni et al. (2011) and defined as the maximum surface temperature gradient along the 1000 m isobath over the confluence region (25° to 45° S, 35° to 70° W). Spatial patterns of variability are extracted using the EOF technique and were based on the whole time series.

Additional time series are computed to represent remote forcing mechanisms that might influence the BMC and were calculated based on monthly outputs from the global model. Furthermore, all indexes are then referenced to the historical period. The Niño 3.4 index was calculated according to the recommendations from the NCAR/UCAR Climate Data Guide and Trenberth (1997). The SAM index was calculated as the leading EOF of the 700 hPa geopotential height south of 20° S as suggested by the National Oceanic and Atmospheric Administration (NOAA) and Ho et al. (2012). The strength and relative position of the South Atlantic Subtropical High (SASH) is calculated as the leading EOF of the 850 hPa geopotential height for the region between the Equator and the South Pole and 70° W and 20° E (Sun et al., 2017). Lastly, the strength of the Agulhas Leakage (AgL)

is computed based on the eulerian transports over the GoodHope line, of waters with temperature over 14.6 °C and salinity over 35.33 (Ansorge et al., 2005; Renault et al., 2017), and its importance to the BMC was previously questioned by Lumpkin and Garzoli (2011).

2.3.4 Gradient-boosting decision tree

We utilize a gradient-boosting decision tree algorithm called LightGBM (Ke et al., 2017) to better understand the dynamics between the BC and MC at the confluence zone. This algorithm uses an ensemble of regression trees that are trained consecutively by fitting the residual errors of predictions at each instance as an input feature to the next iteration (Friedman, 2001). LightGBM finds the optimal nodes along the tree's development by using a histogram-based approach and binning the input data to reduce its complexity. These splits are then based on the variable that explains the most variance at that node, providing the best predictions. A complete description of these methods and the related algorithms can be found on Ke et al. (2017).

Data for the whole simulation time scale (1975 – 2100) is bundled together and 70% of it ($n = 1064$ points) is randomly sampled to train and cross-validate LightGBM's parameters. The remaining 30% ($n = 448$) are used to validate the resulting decision tree. The algorithm is applied for each simulation (control and five realizations of the hist/RCP8.5 scenario) independently. The algorithms' target feature is the meridional position of the BMC. The main input features are the BC and MC transports, the local wind stresses averaged and the latitude of the maximum wind stress curl over the confluence area (Fig. 2.1, in red), and the calculated remote forcing indexes for the El Niño Southern Oscillation (Niño 3.4), the westerlies over the Southern Ocean (SAM) and the SASH strength and position, as well as the AgL volume. The location and width of the BC and MC transport transects were chosen based on the climatological mean kinetic energy plots and we ensured that this position did encompass the full currents during the whole simulation period. All these input features are detrended using a simple least-square fit. Since our number of variables is small and we expect non-linear effects to also have a large role in determining the confluence behavior, we expand the input features by including all second-order polynomial interactions of these variables in the analysis explicitly (e.g. interaction between the Brazil and Malvinas currents), for a total of 36 input features. Afterwards, each feature importance is calculated based on a permutation approach using the eli5 Python library (<https://github.com/TeamHG-Memex/eli5>). By reshuffling each feature and running them along the trained model, one can determine that feature's impact to the overall algorithm performance (Friedman, 2001). A similar procedure to the one employed in eli5 is described in Breiman (2001).

2.4 Evaluation of model results

Results from the HAMSOM Hist/RCP8.5 simulation were compared to data from various sources to assess the quality of the high-resolution simulation. Monthly climatologies (1985 to 2016) of ocean temperature and salinity at a 0.25° resolution were obtained from the Integrated Climate Data Center (ICDC – Hamburg University) and represents the WOCE/Argo Global Hydrographic Climatology (WAGHC) (Gouretski, 2018). For this comparison, HAMSOM results were upsampled at the same horizontal resolution as the WAGHC dataset. This reference dataset was also used to compare our simulation results along the vertical scale, creating a climatological, zonally-averaged, meridional profile of the modelled domain. To evaluate the overall circulation, surface current data from an array of surface drifters was obtained from the Global Drifter Program (GDP) at the National Oceanographic and Atmospheric Administration's Atlantic Oceanographic and Meteorological Laboratory (NOAA/AOML). For all properties, HAMSOM performance was assessed through 2D and time series plots, spatial correlation between model and data and the calculation of the root-mean-squared error (RMSE). All comparisons were made based on monthly averages integrated over the same time period as the comparison dataset and retain the seasonal signal. The intra-annual filter was not applied when validating the model.

2.4.1 Temperature

Climatological sea surface temperature showed good agreement between HAMSOM and the WAGHC climatology (Fig. 2.2) with a spatial RMSE of $1.33 \pm 0.18^\circ\text{C}$. Best agreement was found during the austral summer and worst during austral winter, although still below a RMSE of 1.65°C and with a correlation coefficient higher than 0.98 throughout all months. Of note is the intrusion of cold water along the Brazilian coastline during austral winter, which is in agreement with behaviour previously described for the region (Campos et al., 1999a), and the appearance of a cold tongue along the Equator, induced by strong stratification in the upper-ocean and the equatorial upwelling (Wan et al., 2011). For the BMC inset (red frame in 2.1), spatial statistics between datasets were similar to the results found for the general South Atlantic, with a RMSE of $1.37 \pm 0.18^\circ\text{C}$ and correlation higher than 0.96 for all months.

In the vertical, the mixed layer is well represented and shallower at the equatorial region, representing the effects of the equatorial upwelling (Fig. 2.3). Nevertheless, the WAGHC data suggest a stronger stratification than what can be found in HAMSOM's results, with an overall negative bias indicating higher temperatures in HAMSOM in the upper ocean. The exception is around the BMC/AgL latitude range, where a warm bias indicates lower HAMSOM temperatures. Overall, the meridional temperature profile is

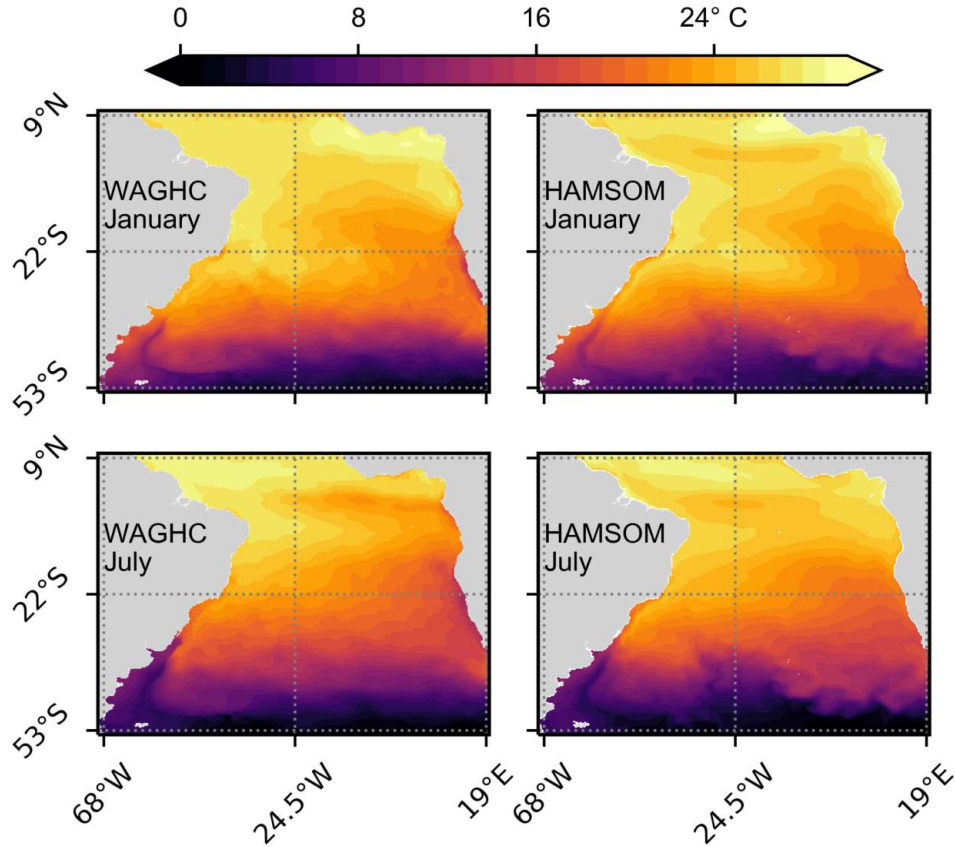


Figure 2.2: Sea surface temperature comparison between the WOCE/Argo Global Hydrographic Climatology (WAGHC - left) and HAMSOM (right) during austral summer (top) and winter (bottom), averaged over 1985 to 2016.

well reproduced, with a 0.99 correlation and a RMSE of 0.8 °C between both datasets.

2.4.2 Salinity

Regarding surface salinity, spatial RMSE and the correlation coefficients were 0.85 ± 0.15 and 0.77 ± 0.05 , respectively, with similar performance during austral summer and winter (Fig. 2.4). Nevertheless, HAMSOM showed a fresher ocean at the northern portion of the South Atlantic Subtropical Gyre and a slightly fresher Southern Ocean. On the northern portion, the influence of the Amazon Plume can be distinguished in both the model results and the climatology, specially during winter, as well as the lower salinity tongue associated with the Equatorial upwelling during summer. In regards to the BMC inset (red frame in 2.1), spatial RMSE and the correlation coefficients were 0.91 ± 0.18 and 0.76 ± 0.09 , respectively, showing a compatible performance in comparison to the general South Atlantic.

The vertical meridional salinity profile showed an overall positive bias of up to 1 (Fig. 2.5), also reflecting the fresher HAMSOM results found along the surface. The position of

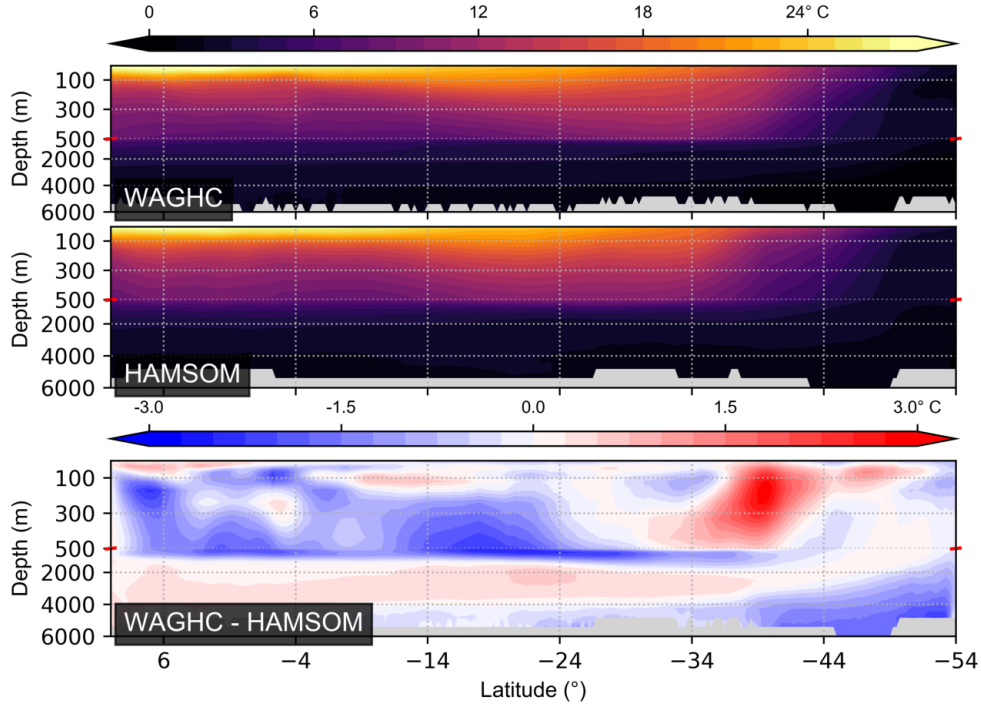


Figure 2.3: Zonally-averaged meridional temperature profile of the modelled domain based on the WOCE/Argo Global Hydrographic Climatology (WAGHC - top) and the HAMSOM model (center). At the bottom, the differences found between both datasets. All units are in °C and the red dash along the vertical axis indicates where the scale is fragmented to highlight the upper ocean (0 m to 500 m). Both datasets are averaged over 1985 to 2016.

the maximum salinity core is well represented and reflects the center of the Subtropical High. The lower salinity at the interface with the Southern Ocean can be seen in both datasets. At higher depths, differences found were smaller than 0.5. Overall, the correlation between both meridional profiles was 0.93, with a RMSE of 0.27.

2.4.3 Surface circulation

Surface circulation was evaluated based on the mean and turbulent kinetic energies per unit mass calculated based on the simulated surface velocity fields and observed tracers drift (Fig. 2.6), following the procedure described by Oliveira et al. (2009). The study area was initially divided into 0.5° cells where the average drifter velocity was calculated from the array of available tracks and then interpolated onto the same HAMSOM grid with a horizontal resolution of 0.5° , averaged over 2000 to 2016. In this case, the standard deviation of the velocity fields reflects the variability of the surface circulation and is used to calculate the turbulent kinetic energy. The spatial correlation score shows a fair agreement in terms of the mean kinetic energy ($r = 0.58$) and a poor agreement for the turbulent part ($r = 0.2$), although at the BMC inset (red frame in 2.1) this turbulent correlation is slightly

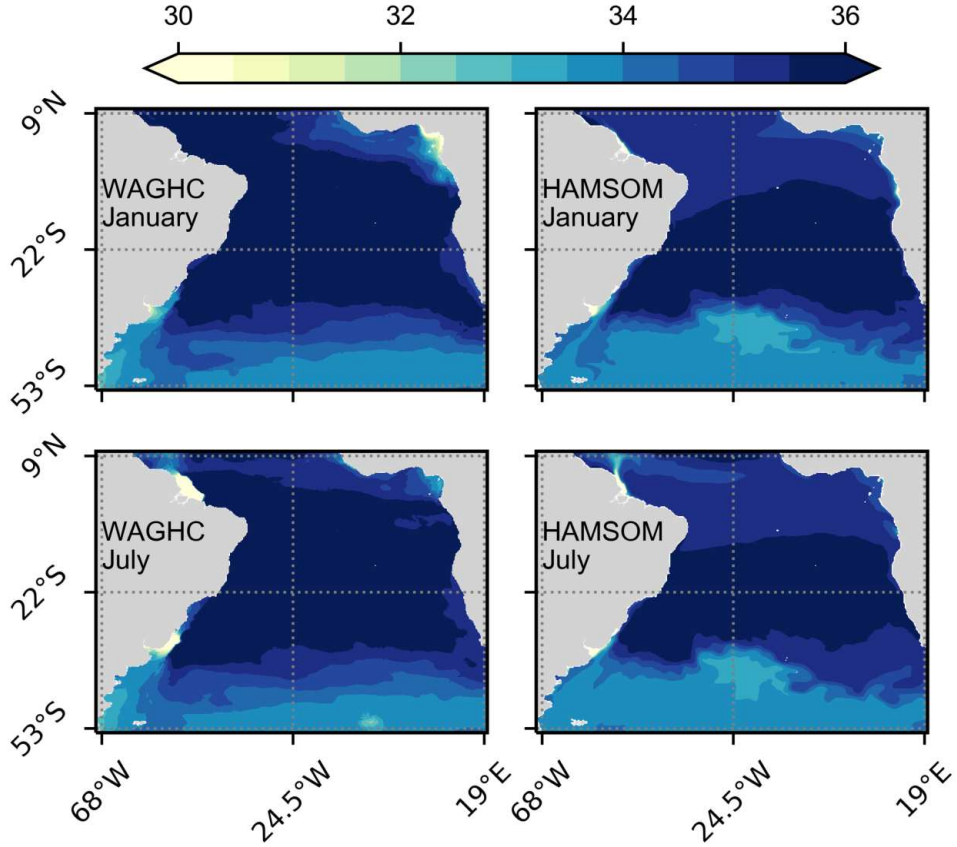


Figure 2.4: Sea surface salinity comparison between the WOCE/Argo Global Hydrographic Climatology (WAGHC - left) and HAMSOM (right) during austral summer (top) and winter (bottom), averaged over 1985 to 2016.

higher than for the general South Atlantic (0.31).

Even though our simulations are eddy-resolving at a horizontal resolution of $1/12^\circ$, the proximity to the eastern boundary does not allow the proper turbulence to develop around the AgL region, meaning the behavior is mainly determined by the inflow boundary conditions. We did not include additional dampening in this region, e.g. the reduction of inflow gradients, to avoid introducing spurious interactions since this is not a target process for our simulation. At the BMC area, the lower branch of the Zapiola anticyclone is not properly resolved in HAMSOM, translating into a stronger South Atlantic current and lower overall turbulence in the BMC inset (Fig. 2.1). This could be due to insufficient bottom friction associated with a coarse vertical discretization of the deep ocean, since [de Miranda et al. \(1999\)](#) and [Combes and Matano \(2014a\)](#) found that the proper reproduction of this feature is sensitive to the bottom friction parametrization. Nevertheless, it does not impact the calculation of the position of the BMC, since this depends mainly on the horizontal temperature gradient between the BC and MC. Still, the main features discerned between HAMSOM and the drifters are comparable, specially the position of the Brazil-Malvinas Confluence, the western boundary currents, the South Atlantic cur-

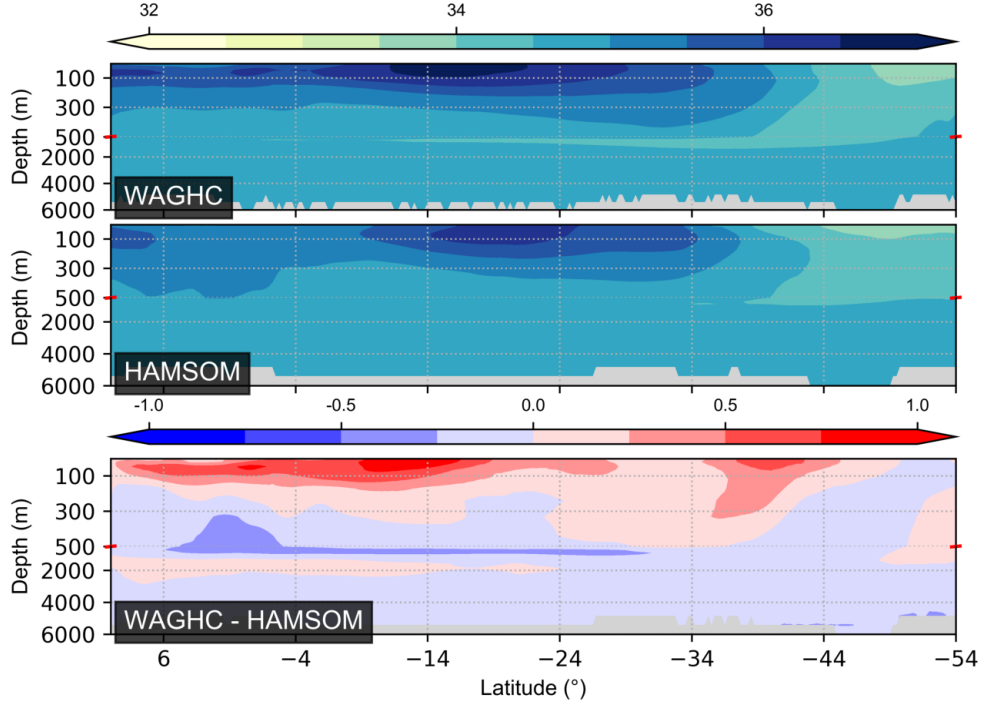


Figure 2.5: Zonally-averaged meridional salinity profile of the modelled domain based on the WOCE/Argo Global Hydrographic Climatology (WAGHC - top) and the HAMSOM model (center). At the bottom, the differences found between both datasets. The red dash along the vertical axis indicates where the scale is fragmented to highlight the upper ocean (0 m to 500 m). Both datasets are averaged over 1985 to 2016.

rent and the Equatorial Current. Also, the mean kinetic energy values found herein are in agreement with the findings of [Kjellsson and Zanna \(2017\)](#) when utilizing a high-resolution ocean model.

2.4.4 Boundary current transport and the Brazil-Malvinas confluence

For the confluence region, we utilized the validation period between 1993 and 2008. This allows our derived trends and time series to better reflect the same time scale used on the related referenced work. The volume transport of the Malvinas Current shows a similar seasonal cycle as found by [Spadone and Provost \(2009\)](#), with a maxima occurring at the end of the austral autumn (Fig. 2.7). They estimated the mean Malvinas transport to be of 34.3 ± 7.4 Sv, similar to the 35.8 ± 8.2 Sv obtained with HAMSOM at a transect at 45° S (see Fig. 2.1 for transect locations). Our estimate of the mean Brazil Current transport at 29° S of 17.5 ± 4.6 Sv is within one standard deviation of the estimated transport of 9.7 ± 6.3 Sv of [Gabioux et al. \(2013\)](#) and references therein. They also found stronger transport anomalies of the BC during austral spring when no data assimilation is employed in the modelling scheme, which is compatible with our results. The seasonal variability on the BMC latitudinal position is well reproduced. The maximum southward incursion hap-

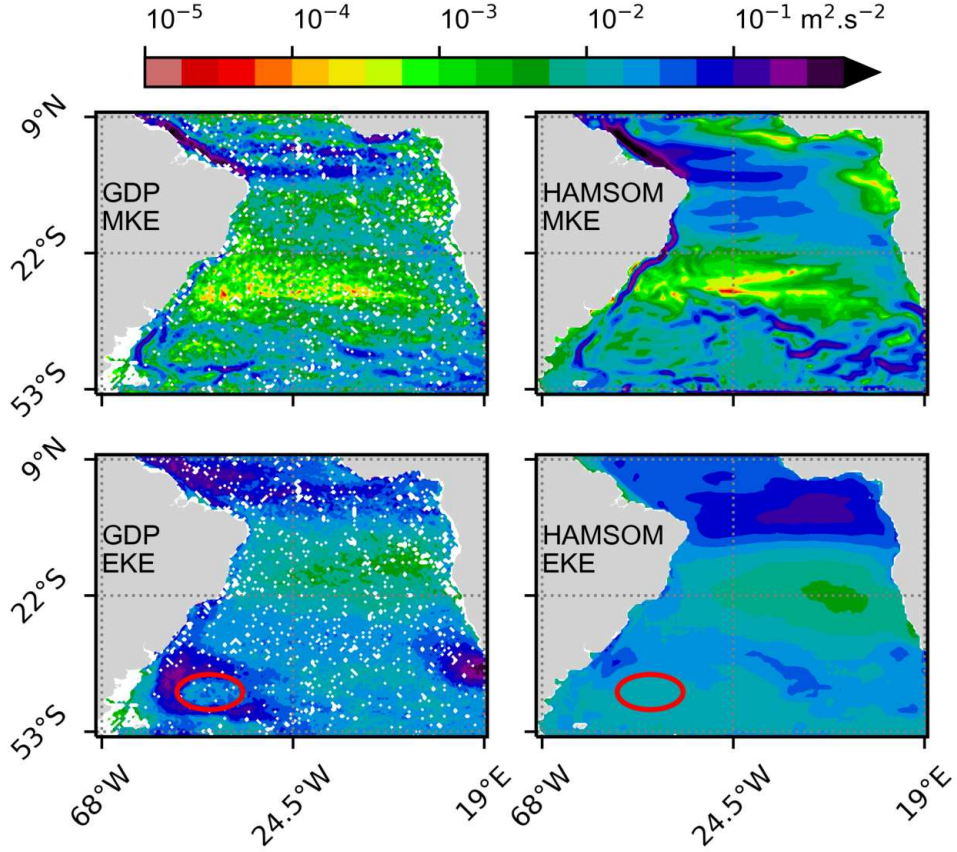
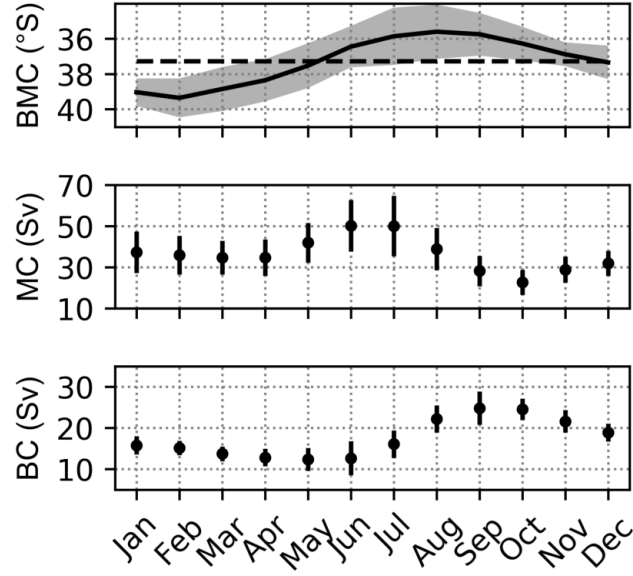


Figure 2.6: Surface mean kinetic energy (upper panels) and turbulent kinetic energy (bottom panels), in $\text{m}^2 \text{s}^{-2}$, calculated based on the binned surface drifter tracks from the Global Drifter Program (GDP - left) and HAMSOM's (right) u- and v-velocity components for the period between 2000 to 2016. The red ellipses in the bottom images highlights the location of the Zapiola anticyclone.

pens during austral summer and the maximum northward incursion during austral winter, while showing the same tendency to linger towards its northern extreme as found by [Matano et al. \(1993\)](#). Lastly, with regards to the confluence southward shift, we found a trend of $-0.82 \pm 0.06^\circ$ per decade over our historical time period. This value is in line with what has been previously reported for the BMC ([Goni et al., 2011](#); [Lumpkin and Garzoli, 2011](#); [Combes and Matano, 2014b](#)).

Figure 2.7: Monthly averages obtained from HAMSON of the Brazil-Malvinas confluence latitudinal position (top), and of the Malvinas (middle) and Brazil (bottom) current transports in Sverdrups \pm one standard deviation. On the top panel, the dashed line indicates the overall average position of the confluence during the validation time window (1993 to 2008).



2.5 Results and discussion

2.5.1 The Brazil-Malvinas confluence southward drift

During the historical period, both the control and hist/RCP8.5 simulations show the same southward drift of the confluence towards an equilibrium at around 37° S (Fig. 2.8). This was expected in both cases, since we corrected the mean state of the ocean and atmosphere towards the observational data using a bias correction. Following the end of the historical into the prognostic period, however, we see differences between both simulations. While the control shows no statistically significant long-term trend for the last 90 years (2010 – 2100), the hist/RCP8.5 scenario shows a persistent southward shift (-0.44° per decade) on the mean confluence position (Figs. 2.7 and 2.10). The same behaviour is apparent in the strength of the MC, only presenting a persistent weakening trend in the hist/RCP8.5 simulation (-1.08 Sv per decade) and leading to a significant decrease of almost 25% of its mean volume transport at the end of the 21st century (mean transport between 1981 – 2010: 38.6 Sv; between 2071 – 2100: 30 Sv). By contrast, no significant trends were found in the BC, staying at its estimated mean volume transport of 18.3 ± 1.3 Sv.

Our domain does not allow us to resolve the volume transport of the ACC directly. For this reason, we calculate the ACC transport at the Drake passage (same location as Combes and Matano, 2014b) directly from the MPI-ESM results (Fig. 2.8). During the prognostic period, both the hist/RCP8.5 and the control simulations show similar decreasing trends for the ACC of -0.25 and -0.34 Sv per decade, respectively. This would point towards an effective trend of $+0.09$ Sv per decade in the hist/RCP8.5 simulation, if we consider the control trend as a measure of model drift, indicating little overall change to the ACC strength over the 21st century in MPI-ESM. Nevertheless, only during the hist/RCP8.5

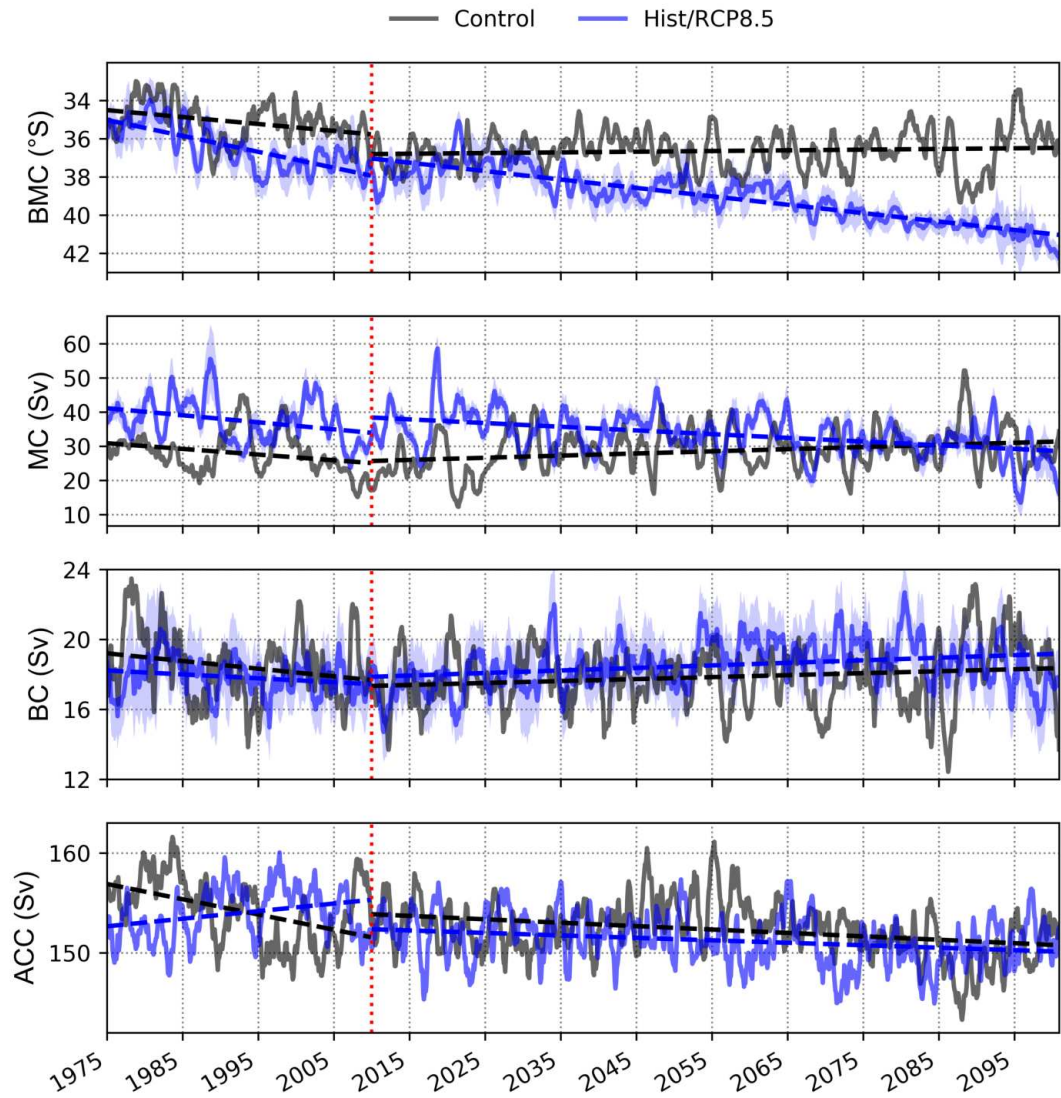


Figure 2.8: Time series of the Brazil-Malvinas confluence latitude (BMC) and the volume transports of the Malvinas and Brazil currents (at the transects defined on Fig. 2.1, based on HAMSOM) and the Antarctic Circumpolar current across the Drake Passage (based on MPI-ESM). The BMC is calculated based on the maximum temperature gradient over the 1000 m isobath, following the methodology from Goni et al. (2011), while the ACC is calculated based on the results from the MPI-ESM. The red line separates between the historical (1975 to 2009) and prognostic (2010 to 2100) periods, and the dashed lines are the calculated trends within those time intervals. The blue shade on the hist/RCP8.5 scenario represents HAMSOM's internal variability based on the five ensemble members.

simulation does the confluence migrates further south within the regional model, while being stable during the control. These results reinforce the findings from [Combes and Matano \(2014b\)](#) that the strength of the MC is the main driving mechanism controlling the confluence meridional position. More than that, it underlines its inconsistency in relation to the overall volume transport of the ACC and its long-term response to climate change.

2.5.2 Response of the Malvinas Current to the Antarctic Circumpolar Current variability

The connection between the MC's volume reduction and the long-term behaviour of the ACC paints an unclear picture. Even more so when we consider the estimated increase on the Southern Ocean atmospheric circulation. This increase is verified by the increasing SAM index ([Marshall, 2003](#)) and its projected increase into the future ([Zheng et al., 2013](#)), and is also valid for the RCP8.5 results from the MPI-ESM (not shown). [Lumpkin and Garzoli \(2011\)](#) had previously found a strong relation between the confluence's position and the southward shift of the maximum wind stress curl, which is related to the position of the westerly wind belt. We calculated the difference between our historical and the end of the prognostic period on sea level pressure and wind velocities over the Southern Ocean based on the MPI-ESM. For the control simulation, no strong changes are found (Fig. 2.9, top panels). For the hist/RCP8.5 simulation, on the other hand, we can see a decrease on sea level pressure along the coastline of Antarctica and a general increase on zonal wind speeds (Fig. 2.9, lower panels). This is consistent with the southward migration of the westerlies belt associated with positive SAM phases ([Marshall, 2003](#)) and reinforces the relation found by [Lumpkin and Garzoli \(2011\)](#) between the confluence and the latitude of the maximum wind stress curl.

Concerning the ACC, [Wang et al. \(2011\)](#) showed that increasing westerlies over the Southern Ocean can lead to a reduction of the ACC's northern flank on some CMIP3 models, which was compensated by an increase in transport along the Antarctic shelf. To see how this increase in wind circulation (seen on Fig. 2.9) could affect the ACC, we first calculated the zonal transport anomaly and found a local maximum at the South Atlantic sector of the Southern Ocean, centred around 47° W (not shown). A Hovmöller diagram of the depth-integrated transport across this longitude shows a mode shift in the ACC main pathway, at around 60° S (Fig. 2.10). In the hist/RCP8.5, the transport at this latitude continually increases along the 21st century, predominantly after 2050, in congruence with the steady decrease of the MC. This connection to the MC is clearer when we consider the control simulation, however. Pulses of stronger transport at 60° S mirror moments when the MC transport decreases, and the MC intensifies as the ACC flow reduces at 60° S and increases at 57° S. With this relationship in mind, the suggested mechanism is as

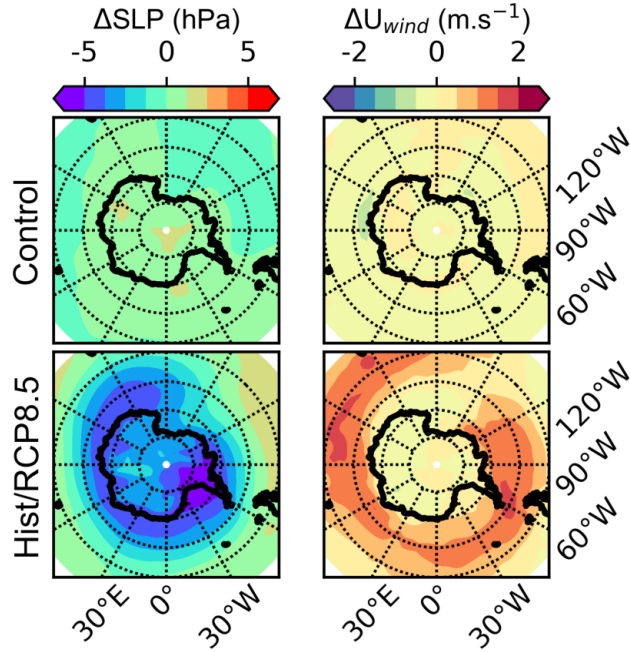


Figure 2.9: Differences on sea level pressure (SLP – left) and zonal wind velocities (U – right) for the control (top) and hist/RCP8.5 (bottom) simulations based on results from the MPI-ESM. The differences reflect the change between the end of the 21st century (2071 to 2100) and the historical period climatology (1981 to 2010).

follows: as the main ACC pathway shifts to a position closer to Antarctica's shelf, the weaker northern branch of the ACC leads to a reduced MC transport. Then, since the MC is supposed to be the controlling forcing of the BMC meridional position, the confluence migrates southward.

Apart from the results concerning the connections between the ACC and the MC and its effect on the BMC, the effects of a higher resolution on simulating the MC are also evident (Fig. 2.11). Although both time series show a similar decadal variability (Fig. 2.11, black lines), the MPI-ESM shows higher variability in the interannual scale. Of note is the MPI-ESM MC's increase between 2035 to 2055. While this is in line with the decrease on the ACC transport across 47° W and related to the feedback mechanisms between the MC and the ACC, the lack of a correspondent increase in HAMSOM's MC points towards the importance of mesoscale features in limiting some of these interannual oscillations. Further studies on the importance of mesoscale activity on the MC could shed better light on this relation. For example, [Yang and He \(2014\)](#) showed how upward eddy fluxes in the BMC region can play an important role in transforming the Antarctic Intermediate Water.

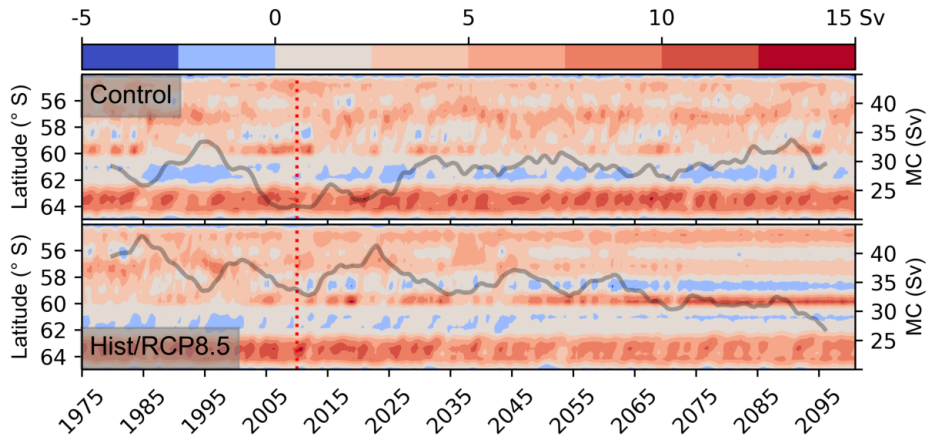


Figure 2.10: Hovmöller diagram of the depth-integrated transport of the Antarctic Circumpolar Current across 47° W for the control (top) and hist/RCP8.5 (bottom) simulations based on results from the MPI-ESM. The black line represents the decadal variability of the Malvinas Current, after the application of a 10-years moving average on the time series from Fig. 2.8. The red line separates between the historical (1975 to 2009) and prognostic (2010 to 2100) periods. All transports are in Sverdrups.

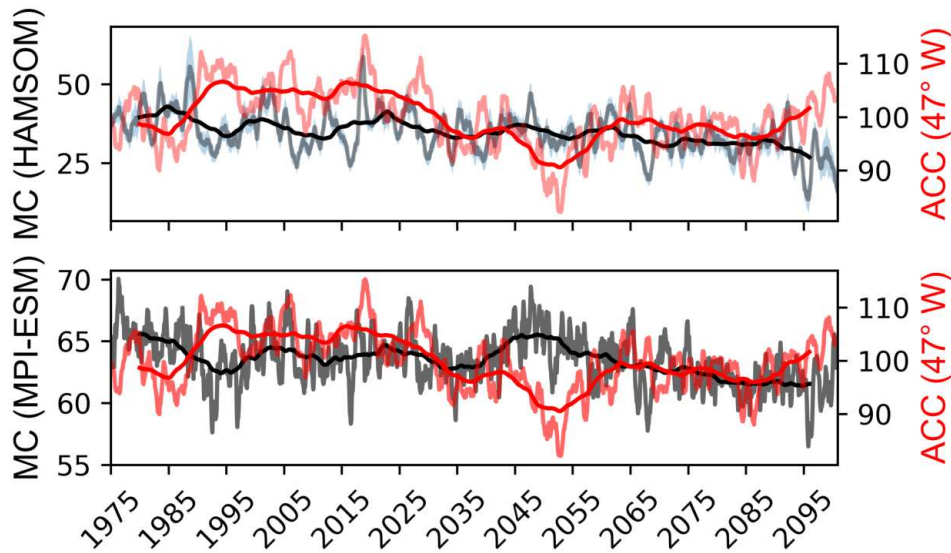


Figure 2.11: Comparison between the total ACC transport across 47° W and the Malvinas current transport across 45° S (see figure 2.1), calculated based on HAM-SOM's (top) and the MPI-ESM (bottom) hist/RCP8.5 simulations. All transports are in Sverdrups (Sv). Bold lines represent the decadal variability on volume transports, and the blue shade on HAM-SOM's scenario represents HAM-SOM's internal variability based on the five ensembles.

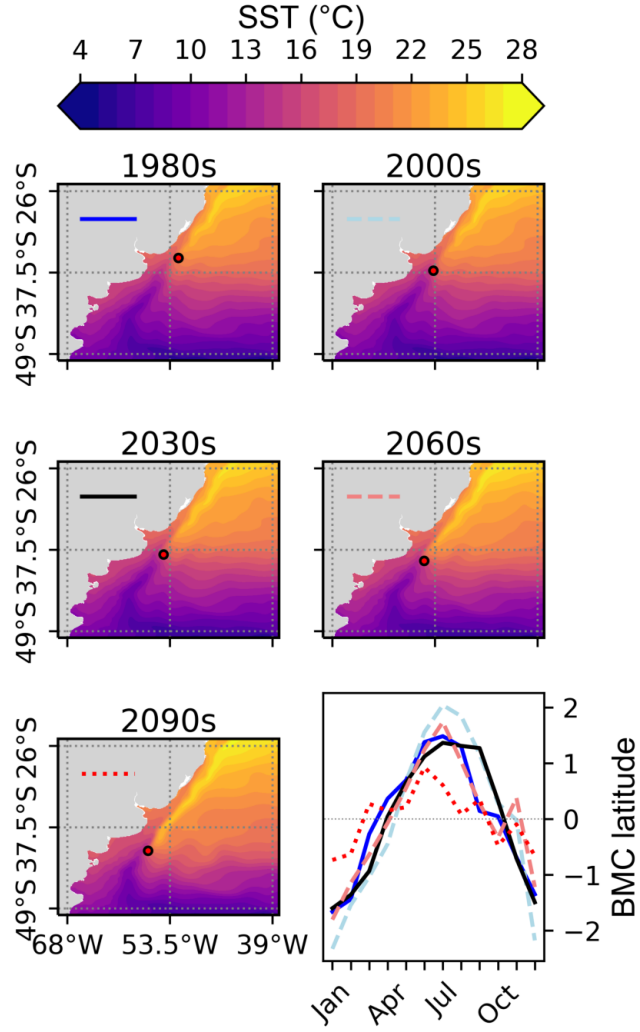
2.5.3 Natural variability of the Brazil-Malvinas confluence

We average the BMC position over different decades of the hist/RCP8.5 simulation. Within each of these decades (1980s, 2000s, 2030s, 2060s, 2090s), we calculate the BMC's seasonality (Fig. 2.12). As the confluence moves further south, we see a reduction of the amplitude of its intra-annual variability and there is a slight shift in the period of maximum northward intrusion, which is reached in June instead of July/August (Matano et al., 1993). This reduction in variability is also apparent on the interannual scale (Fig. 2.13) and seems to be related to a similar reduction on the MC's own variability (Fig. 2.8).

After removing the long-term effects of the climate trend using a least-square fit, we analyze the underlying variability at the BMC based on the filtered time series. An EOF analysis of the detrended SST fields in this region (Fig. 2.1, red box) for both the control and the ensemble mean of the hist/RCP8.5 simulations show this relation further (Fig. 2.13). In the control simulation, the first and second EOFs explain 25% and 15.3% of the total variance and its expansion coefficients (ECs), which represent the EOF's temporal variability, have a 0.65 and 0.57 correlation ($p < 0.05$, Tab. 2.1) to the BMC. If we sum both ECs, its correlation to the BMC position increases to 0.87 and would account for approximately 40% of the total variance. Both EOFs also show general temperature changes across the chosen confluence region subset. This is evidenced by the negative and positive anomalies outside the confluence's core in the first and second EOFs, respectively. In the hist/RCP8.5 ensemble members, however, only the second EOF has a reasonable correlation to the BMC position ($0.53 \leq r \leq 0.74$, $p < 0.05$), explaining 18.2% of the ensemble mean's total variance. The first EOF explains 25.2% of the variance and seems to be regionally focused on the variability of the MC across most of the ensemble members, with correlations of up to 0.42. The second EOF, on the other hand, has a stronger negative correlation with the BC variability. Summing up both ECs, in this case, does not change the correlation to the BMC when compared to the second EOF alone. The same separation between the MC and BC's influence cannot be made for the control simulation, since in both cases its correlation to the BC is small (Tab. 2.1). This shows that variations over the MC portion of the BMC dominates the variability in this region under our strong climate scenario.

It is important to note, however, that these correlations to the forcing mechanisms are rather moderate, never exceeding 0.5. In part, this could be due to secondary variability mechanisms affecting the SST that are not reflected on the MC and BC current transport, since these properties do not depend on surface temperature to be derived. Or could also be due to these EOF patterns being a reflection of a combination of driving mechanisms, of which the MC and BC would be a part of. Since there is no easy way to make this distinction between different forcing mechanisms, we employed a gradient-boosting decision tree (GBDT) algorithm to disentangle the relative contribution of each input feature in

Figure 2.12: Decadal averages of sea surface temperature for the BMC region (red box in Fig. 2.1) on the 1980s, 2000s, 2030s, 2060s and 2090s, based on the hist/RCP8.5 simulation results from HAMSON. The red dot represents the calculated confluence position within the designated decade based on the maximum temperature gradient over the 1000 m isobath. On the bottom right, the normalized confluence's seasonality within each decade.



determining the natural variability of the BMC (see methods' section d. for a description of inputs). The use of a GBDT is similar to how clustering is employed to detect similarity between samples based on a set of characteristics. But instead of having multiple samples, we have a single target property to be predicted, i.e. the BMC position. In this context, those characteristics represent the local and remote forcings we assume to impact the confluence's dynamics. After training the algorithm based on a randomly-sampled subset of our data (70%, $n = 1064$ points), the algorithm was validated against the remaining 30% for each simulation independently. The resulting GBDT prediction had a 0.84 ± 0.01 correlation to HAMSON's modelled BMC with a RMSE of $0.40 \pm 0.02^\circ$ for the hist/RCP8.5 ensemble members, and a correlation of 0.78 with a RMSE of 0.62° for the control run.

Based on the trained algorithm, we calculate each feature's importance using a permutation technique and gathered the three most important features from each simulation. Since those three features were not the same across all simulations, a total of 10 from the 36 individual features are presented. The remaining features had, in general, less than 5% importance on any given simulation. These 10 features were then sorted based on their

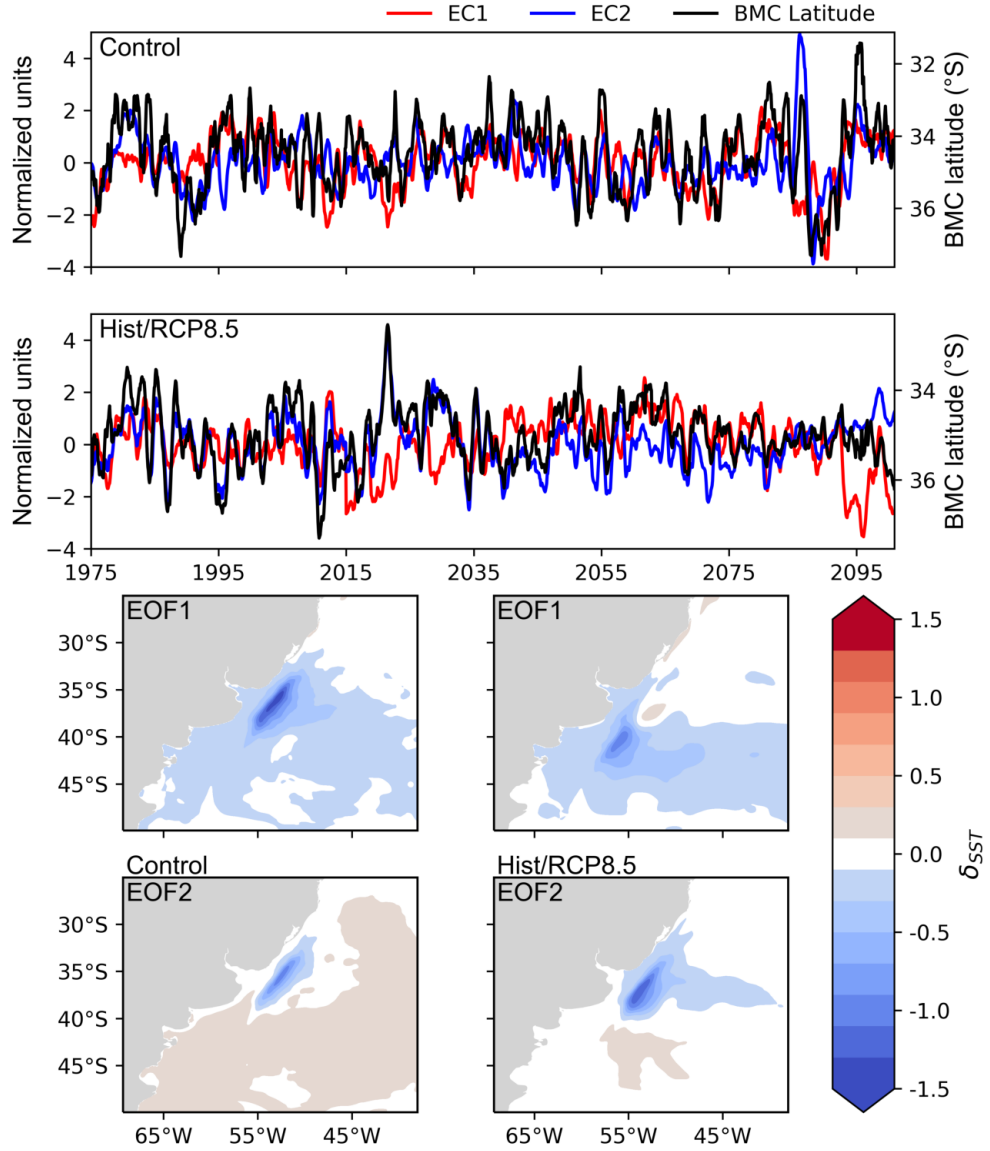


Figure 2.13: Normalized meridional latitude of the BMC (detrended) and the first and second expansion coefficients associated with the respective EOFs of the sea surface temperature, extracted based on HAMSON's results. The region where the EOFs were extracted is indicated in Fig. 2.1 (red box).

mean overall importance for the hist/RCP8.5 ensemble members (Fig. 2.14).

In agreement with the EOF analysis, the variability of the MC dominates the GBDT prediction in three out of five of the hist/RCP8.5 scenarios, with the non-linear interaction between the BC and MC dominating the first ensemble member (hist/RCP8.5_1) and as the second most important feature in most simulations. In essence, these reflect the main modes of variability extracted with the EOFs for the ensemble mean of the scenarios under the climate forcing (Fig. 2.13, right panels), but can be directly related to the BMC variability as opposed to the SST. The effect of the wind stress curl over the BMC region

Table 2.1: Pearson correlation between the first and second expansion coefficients (EC) and the detrended time series of the meridional confluence position (BMC) and the volume transports of the Malvinas (MC) and Brazil (BC) currents. All correlations were significant with $p < 0.05$.

	Correlation with EC1			Correlation with EC2		
	BMC	MC	BC	BMC	MC	BC
Control	0.65	0.34	-0.03	0.57	-0.19	-0.13
Hist/RCP8.5_1	0.48	0.42	0.09	0.53	0.13	-0.36
Hist/RCP8.5_2	0.41	0.40	0.06	0.65	0.21	-0.41
Hist/RCP8.5_3	0.13	0.30	0.22	0.74	0.33	-0.41
Hist/RCP8.5_4	0.31	0.35	0.18	0.73	0.26	-0.34
Hist/RCP8.5_5	0.36	0.37	0.18	0.67	0.18	-0.39

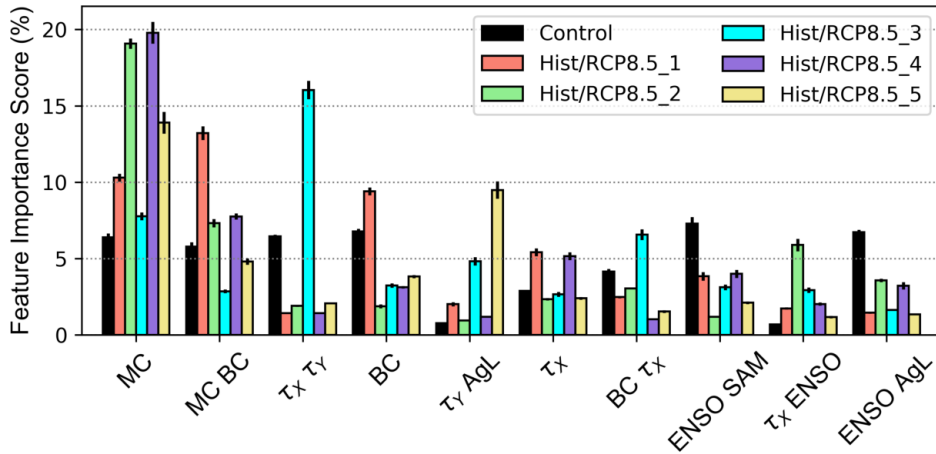


Figure 2.14: Feature importance based on the three dominant features from each simulation (control and five ensemble members of the hist/RCP8.5).

and the linear variability of the BC are the next dominating features. Their interaction with the BMC has been described by previous authors (Wainer et al., 2000; Goni et al., 2011; Lumpkin and Garzoli, 2011), both on seasonal and interannual time scales, although our results here are only related to the interannual component. It is also important to stress that the wind stress curl was the dominant feature for the third ensemble member (hist/RCP8.5_3), which showed the smaller correlation between the EC1 and the MC variability (Tab. 2.1). This could be an indication that, under some circumstances, local wind effects over the confluence region can exert a significant control over the BMC variability. Nevertheless, the MC was still the second dominant feature for this ensemble member. In contrast, the effects of these features (MC, BC and wind stress curl) in the control simulation are virtually the same when their standard deviation is considered, without a clear

dominant forcing. Furthermore, applying the trained algorithm to the historical period of the hist/RCP8.5 simulations only (not shown) reveals a similarly balanced dominance across these features, which could explain why different authors found evidences pointing to all of the three mechanisms (Goni et al., 2011; Lumpkin and Garzoli, 2011; Combes and Matano, 2014b). In combination, these results reinforce ours and Combes and Matano (2014b) findings regarding the influence of the MC on controlling the natural variability at the confluence region and strengthens our argument of climate change being the dominant factor affecting the MC, growing in importance as atmospheric greenhouse gas concentrations increase.

Among the remote effects, ENSO and the Agulhas leakage (AgL) dominated. Specially concerning the control, interactions with ENSO had about the same importance as the local effects (MC, BC and wind stress curl). This behavior is in line with the extracted EOFs and could explain the negative/positive dichotomy between the control's first and second modes of variability, as the impact of a large-scale atmospheric mode such as ENSO would affect the whole confluence region. This points to a reduction of the impact of such large-scale forcing under a strong climate scenario, when the local effects become more prominent. As far as the mechanism, Rodrigues et al. (2015) showed how El Niño events can trigger positive phases of the South Atlantic subtropical dipole mode (SASD). During this phase, positive SST anomalies develop in the Southwestern Atlantic and are accompanied by a southward shift of the SASH and a weakening of the westerlies (Morioka et al., 2011). The strengthening of the SST gradient in this region has also been found to dominate the quasi-decadal variability (7 to 10 years) of the subpolar and subtropical oceanic frontal zones (Kazmin, 2017) in the South Atlantic. This periodicity, along with a bi-annual signal, was found to be important at the BMC by Combes and Matano (2014b), using a wavelet analysis. Applying the same wavelet procedure to our BMC time series yields similar 2- and 7-years high-energy periodicities (not shown). This demonstrates how the ENSO connects to the dynamics of the confluence, especially considering that the non-linear interaction between ENSO and the SAM was the dominant ENSO related feature. Regarding the AgL, the dominant related feature in the GBDT analysis is its non-linear interaction with the meridional wind stress (τ_Y). In this case, however, it is likely that the captured relation in this interaction is not a direct response mechanism between the BMC and the AgL, as Biastoch et al. (2009) showed how the poleward shift of the westerlies would lead to an increase of the Agulhas leakage. Instead, both properties would be responding to the variability of the atmospheric circulation over the Southern Ocean. Nevertheless, the lower importance given by the GBDT to the SAM and SASH index does not necessarily mean a weaker connection of these atmospheric modes to the BMC. It can be that these features are somewhat redundant in relation to others (e.g., the SASH and the BC) and/or affect the confluence indirectly (e.g., the SAM and the MC). In these circumstances, the GBDT

algorithm can help identify which parameters warrants a closer look and help to identify important interactions.

2.6 Conclusions

We investigated how a mode shift in the main pathway of the Antarctic Circumpolar Current under a warming climate might be the underlying cause for the confluence's southward shift over the last decades, and how this would persist throughout the 21st century under a continued scenario of increasing greenhouse gas emissions. Our simulations indicate that as the ACC's main flow shifts closer to the Antarctic shelf, the reduction on its northern branch leads to a reduction of the Malvinas current transport. As the MC weakens, the mean meridional position of the Brazil-Malvinas confluence drifts further southward, reaching $42.2 \pm 0.7^\circ$ S at the end of the century. This behavior is consistent even in the face of a strengthening atmospheric circulation over the Southern Ocean. The weakening of the MC also impacts the seasonal and interannual variability of the BMC front, reducing its amplitude. This impact on the MC volume transport is significant as the main SST variability mode when extracting the EOFs at the confluence region, accounting for 25% of the total SST variance. This same variability mode cannot be seen on a simulation without any anthropogenic climate forcing, in which the BMC's dynamics dominates both the first and second EOFs, and the orthogonal source of variability seems to be related to ENSO.

We also showed how a machine learning algorithm can provide insight when dealing with non-linear physical processes. The model was able to accurately estimate the position of the confluence based on a limited set of local (BC and MC volume transports and decomposed wind stress curl) and remote (Agulhas leakage, ENSO, SAM and SASH) forcing parameters and its interactions. The fact that features that have been discussed by other studies to exert a strong effect on the BMC's dynamics dominates the feature importance of the GBDT grants reliability to its usage, and some of the captured non-linear interactions, as exemplified by the ENSO-SAM relation, have strong support in published literature ([Morioka et al., 2011](#)). This method was also able to capture nuances in the forcing mechanisms among ensemble members, indicating its effectiveness in distinguishing between the BMC's sources of variability.

Our model experiments indicate that under increasing atmospheric greenhouse gas concentrations the dominant driving mechanism of the BMC variability will become the MC and its non-linear interaction with the BC, followed by the effects of the local wind stress curl and the variability of the BC itself. Large scale effects, such as ENSO, can be considered a secondary variability source, whose influence is reducing under anthropogenic climate change.

Chapter 3

Possible Impacts of Anthropogenic Climate Change to the Upwelling in the South Brazil Bight

This chapter has been published in *Climate Dynamics*:
de Souza MM, Mathis M, Mayer B, Noernberg MA, Pohlmann T (2020) Possible impacts of anthropogenic climate change to the upwelling in the South Brazil Bight. Clim Dyn 55:651–664, doi: 10.1007/s00382-020-05289-0

<https://link.springer.com/article/10.1007/s00382-020-05289-0>

3.1 Abstract

Anthropogenic climate change is expected to strengthen upwelling events worldwide, driven by an increase of upwelling-favorable winds. However, Earth System Models (ESM) tend to underestimate regional processes due to their coarse grid resolution, which can lead to local biases. We use a high-resolution ocean model ($1/12^\circ$) forced by results from the Max-Planck-Institute-ESM to analyze the impact of the RCP8.5 emission scenario on the upwelling of South Atlantic Central Water (SACW) in the South Brazil Bight (SBB). We find a stronger Ekman forcing and a higher spread of SACW over the shelf, but this does not translate into higher vertical velocities at the bottom of the mixed-layer in the end of the century. The increased winds' effect is essentially balanced by an increase in water column stability due to the surface warming. This is particularly important during austral summer, when this process tends to weaken the upwelling. Vertical velocities decrease significantly along the shelf break. Here, the upwelling regime is governed by the Brazil Current (BC) and slight changes in transport induce large responses in upwelling strength. The consequences are increased sea surface temperatures over most of the shelf, although mitigated by the SACW upwelling and kept below global projections. However, temperatures decrease along Cabo Frio. In this region, shelf break upwelling dominates and is enhanced by a local increase in the BC transport. This highlights the importance of regional processes and, more specifically, of changes in the BC transport for the upwelling in the SBB.

3.2 Introduction

The South Brazil Bight (SBB) is located between Cabo Frio and the Santa Marta Cape (23° to 28.5° S, Fig. 3.1) (Castro and Miranda, 1998). Its most striking characteristic is an abrupt change in coastline orientation, from NE-SW to E-W in the Cabo Frio region. This is accompanied by a progressively larger continental shelf, extending over 200 km at its central portion before reducing back to approximately 70 km at the Santa Marta Cape (Piola et al., 2018). Campos et al. (1995) conducted one of the first studies regarding the thermodynamic state and circulation in the SBB, based on an array of CTD measurements and geostrophic calculations. Based on their analysis, the SBB water mass is mainly composed of Tropical Water (TW: $>20^\circ\text{C}$ and salinity >36.4), South Atlantic Central Water (SACW: $<20^\circ\text{C}$ and salinity <36.4) and Coastal Water (CW). The latter is a result of the dilution of ocean water by the local freshwater discharge from several estuarine systems in this region. It is also affected by the intrusion of colder and fresher water associated with the Plata River (Campos et al., 1996), with its plume having been identified up to 24° S (Piola et al., 2005) within the SBB. This intrusion happens mostly during winter and is driven by southwesterly wind anomalies associated with cold fronts (Piola et al., 2005;

Pimenta et al., 2005), and to a lesser extent to very high discharge periods during El Niño events (Campos et al., 1999b).

At the shelf-ocean interface, the SBB dynamics is dominated by the Brazil Current (BC) (Campos et al., 1995, 2000; Silveira et al., 2000). The predominantly southwestward flow associated with the BC is composed of TW in the upper 200 m of the water column, followed by SACW until 750 m and Antarctic Intermediate Water (AAIW) down to 900 m (Campos et al., 1995). Of note is that the sudden change in coastline orientation creates intense meso-scale activity along the main BC flow, with a general conversion of eddy- to mean-kinetic energy (Oliveira et al., 2009). This meso-scale activity has been suggested to induce shelf break upwelling in the region, through the development of cyclonic meanders that propagates southward from Cabo Frio (Campos et al., 2000; Castelao et al., 2004; Castro et al., 2006). These meanders would be formed due to barotropic shear instabilities associated with topographic Rossby waves (Silveira et al., 2000) developed along the BC. Palma and Matano (2009), however, suggested that this shelf break upwelling is rather a consequence of coastal geometry. They argued that changes in bottom topography would modify the meridional pressure gradient along the BC pathway and induce inshore flow in the bottom boundary layer. This process would be independent of the meso-scale activity and account for the differences in the effectiveness of the SACW upwelling in the northern and southern portions of the SBB.

Aside from the upwelling of SACW related to the BC dynamics, the SBB is characterized by the presence of a second upwelling regime that affects the region year-round (Campos et al., 2000; Palma and Matano, 2009). This second regime is controlled by the wind-driven Ekman transport. In this region, wind-driven upwelling is favorable throughout the year due to persistent northeasterly winds associated with the South Atlantic Subtropical High (Castro and Miranda, 1998; Lima et al., 1996; Castelao et al., 2004). This process is most effective during austral summer, when Cerda and Castro (2014) found SACW volumes on the shelf twice as large as for the TW and Campos et al. (2000) found the SACW signal as close as 50 km to the coastline, retreating closer to the shelf break (depths >100 m) during winter. These seasonal differences are mainly a consequence of the passage of cold atmospheric fronts during winter, bringing strong southerly winds to the region (Castro and Miranda, 1998). Möller et al. (2008) also demonstrated how this seasonal wind variability controlled the water mass distribution along the Southern Brazilian shelf, south of the SBB, being responsible for the SACW upwelling at the Santa Marta Cape.

The SBB also has large economic importance for Brazil. It is the location of some of the largest crude oil deposits (Santos Bay) available for exploration, and very productive fisheries grounds that fuel local and international markets (Castro et al., 2006). On an ecological sense, Brandini et al. (2014) demonstrated how the SACW intrusion improved light

conditions for phytoplankton growth and provided missing nutrients (especially nitrate), fueling primary production at the base of the euphotic zone. They also proposed that the periodical intrusion and regression of SACW due to the wind-driven Ekman transport was used throughout the diatoms life cycle to maintain a presence within this nutrient-rich environment, contributing to the formation of a deep chlorophyll maximum at the SACW/(TW, CW) interface. However, anthropogenic climate change has been shown to impact the ecological state of affected regions due to the ecosystem's response to abiotic changes (e.g. temperature and sea level rise) and to emergent ecological responses (e.g. zonation patterns and biogeographical ranges) (Harley et al., 2006). Recently, Brandini et al. (2018) stressed how understanding climate change's impacts on the SBB is crucial for better management of its coastal tourism and aquaculture.

Notwithstanding, no long-term studies are available in this region about the impacts of a changing climate under increasing atmospheric greenhouse gas (GHG) concentrations. Analysis of current observational data as well as future projections based on global Earth system models predict an overall expansion of the Hadley circulation (Davis and Rosenlof, 2012; Hu et al., 2018) and a southward migration of the sub-polar jets (Barnes and Polvani, 2013), with an accompanying southward migration of the Southern Hemisphere atmospheric circulation (Kushner et al., 2000; Rykaczewski et al., 2015). Under these conditions, a larger portion of the SBB could be under the influence of the stronger NE winds that favors upwelling conditions year-round. These could lead to an increase in the upwelling's strength and/or persistence. Similar effects have been found across different locations, both on the global (Sydeman et al., 2014; Wang et al., 2015) and regional (Snyder et al., 2003; Miranda et al., 2013; Praveen et al., 2016; Sousa et al., 2017) scales. More recently, Varela et al. (2018) identified cooling trends north of the SBB when compared to the adjacent open ocean, based on a global analysis of AVHRR data from 1982 to 2015. They linked this SST decrease to a reinforcement of upwelling favorable winds but did not investigate further potential changes in the course of future scenarios. Nevertheless, despite the usefulness of global climate models in providing a general picture of the expected impacts of increased GHG concentrations, their ability to properly represent regional processes is limited due to their coarse resolution (Wang et al., 2010; Snyder et al., 2003). This can lead to biased responses on the regional scale due to the underrepresented local processes (Praveen et al., 2016).

In the present study, we conduct an investigation of potential climate impacts on the two upwelling regimes in the SBB that takes into account meso-scale processes in the ocean circulation. This is carried out by downscaling results from a global Earth system model (MPI-ESM-MR, Giorgetta et al., 2013) using a regional ocean model (HAMSOM) of higher grid resolution, under a strong warming scenario (RCP8.5 - IPCC, 2014). This approach allows for an estimation of the upper-bound effects associated with anthropogenic climate

change and the influence of this external forcing to the SBB, as well as to the mechanisms governing both upwelling regimes.

3.3 Methods

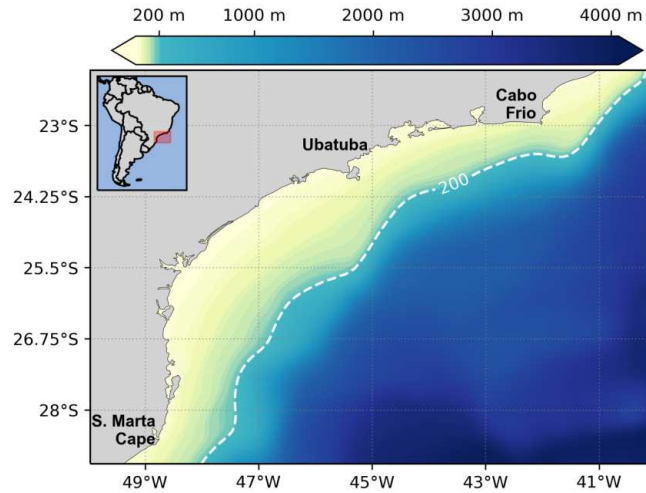
In this study, we utilize the outputs of a large-scale Earth system model (MPI-ESM-MR, Max-Planck Earth System Model - Mixed Resolution ([Giorgetta et al., 2013](#))) in the context of the Coupled Model Intercomparison Project Phase 5 (CMIP5) to provide boundary conditions (atmosphere and ocean) for a high-resolution domain ($1/12^\circ$) spanning the whole South Atlantic (10° N and 54° S and 69° W and 19° E, approximately). The high-resolution simulations have been performed using the HAMSOM model (HAMBurg Shelf Ocean Model - [Backhaus, 1985](#); [Pohlmann, 1996, 2006](#)) and focus on properly resolving the upper ocean flow with a crude resolution of the deep ocean circulation. All forcing data has been bias-corrected using a combination of AVISO satellite information, 3D temperature and salinity profiles from SODA ([Carton and Giese, 2008](#)) and atmospheric data from the NCEP/NCAR reanalysis dataset ([Kalnay et al., 1996](#)). For a detailed description of the model configuration and setup and the model evaluation see [de Souza et al. \(2019\)](#).

Our total simulation period ranges from 1950 to 2100 with the interval between 1950 and 1974 reserved to spin-up the model, necessary due to the bias-correction and the increased horizontal resolution compared to the global model. The remaining 125 years are then separated into a historic (35 years, from 1975 to 2009) and prognostic periods (90 years, from 2010 to 2100). In order to characterize the impacts of climate change as an upper-bound effect in the SBB, we utilize MPI-ESM model results reflecting the representative concentration pathway 8.5 (RCP8.5, defined from 2005 onward) combined with the historical run (Hist, defined until 2004), and contrasting against pre-industrial GHG levels (Control) ([IPCC, 2014](#)). For the combined Hist/RCP8.5 simulations, five ensemble members have been produced. These ensemble members reflect random modifications (within 1% of their base values) to the initial temperature and salinity fields of our high-resolution simulations and account for the regional model's internal variability.

HAMSOM's results are saved as daily averages throughout the whole simulation and consist of data on sea surface heights, temperature, salinity and zonal and meridional current velocities. Seasonal patterns are analyzed by comparing austral summer (December, January and February - DJF) and winter (June, July and August - JJA) climatologies, derived from monthly-averaged data. Because we are also interested in the long-term effects associated with anthropogenic climate change, all seasonal variability is then removed by applying a 12-months running mean, yielding the inter-annual signal.

Our analysis focuses on the SBB region (Fig. [3.1](#)), limited offshore by the continen-

Figure 3.1: Location of the South Brazil Bight, showing its bathymetry. The white dashed line marks the shelf break (200 m isobath).



tal shelf break (depths <200 m). Long-term climate effects are estimated by comparing time slices representing the end of century (EofC: 2071 to 2100) and the historical (Hist: 1980 to 2009) climatologies. These projected change signals are then compared with the variance of the Control simulation to assess statistical significance. To derive a robust and representative variance of the Control scenario, we calculate all possible 30-year climatologies, starting from 1980 until 2071. The standard-deviation from these climatologies is then multiplied by $\sqrt{2}$ to double the variance and increase confidence in the calculated changes, and by 1.96 to ascribe a significance level of 95%. When the projected change signal is stronger than this boosted Control variance, we can consider the found differences statistically significant, while accounting for the possibility of model drift within the simulations. This process follows the methodology described by Mathis et al. (2018).

Traditionally, the intrusion of SACW in the SBB is estimated based on vertical temperature profiles and isotherm depth (17 °C to 20 °C, Campos et al. (1995); Castelao et al. (2004); Brandini et al. (2014); Castro (2014); Cerda and Castro (2014)), with modeling studies complementing these with bottom velocities (Palma and Matano, 2009) or vertical velocities at specified depths (Campos et al., 2000). Unfortunately, changes in temperature and salinity due to increased GHG emissions are expected to have a measurable effect in the upper 700 m of the Earth's ocean (IPCC, 2013), which would make separating changes in the isotherm position from the increased warming complicated in the depth range of the continental shelf (~200 m). To evaluate this possibility in the SBB, we extracted all temperature and salinity data along the shelf break (white dashed line in Fig. 3.1) for the Control and Hist/RCP8.5 scenarios and plotted them in a T-S diagram for the historical and end of century climatologies (Fig. 3.2). Based on this diagram, we can see that no significant modifications on the water masses distribution is found during the Control simulation and the centroid of each climatology overlaps (white X in Fig. 3.2). At the same time, there is a clear shift in both properties for the Hist/RCP8.5 scenario, affecting the whole water column. Based on these results, estimating the SACW's change signal over

the SBB based on water mass characteristics would lead to uncertainties due to the general temperature and salinity increases expected under a warming climate.

As an alternative, changes to the SACW upwelling are estimated based on the vertical velocity at the bottom of the mixed-layer (W_{MLD}). The bottom-parallel flow associated with the upwelling at the shelf break is proportional to the vertical velocity over the shelf, while the upwelling associated with the meso-scale regime directly over the shelf break would have a clear vertical influence that should also be captured at the mixed-layer. This way, we can represent both upwelling regimes described in the literature for the SBB using a single reference property. The mixed-layer depth (MLD) was calculated based on the temperature difference criteria, using a threshold of -0.5°C when compared to the sea surface temperature (SST), as first proposed by [Levitus \(1983\)](#). This ensures that the calculated W_{MLD} is physically consistent throughout the simulation period, always representing changes in the vertical transport at the top of the thermocline. In case the calculated MLD is deeper than the total depth at the cell (possible close to the shoreline), all interpolated values at those cells are set as undefined for that time step and not considered in further calculations.

3.4 Results

3.4.1 Ensemble evaluation

To verify the quality of our ensemble simulations and evaluate the impact of the system's internal variability on the model results, we calculate the domain-averaged (area of Fig. 3.1) SST, MLD and the upwelling velocities at the bottom of the mixed-layer (W_{Upw}) for all five ensemble members as well as for the median of all ensembles. In this case, the median was chosen in order to ensure that the generated dataset is comprised of information found in at least one of the ensemble members.

For all evaluated variables, the median preserved the dominating frequency range of the time series (Fig. 3.3). Among these properties, the highest ensemble spread is found for W_{Upw} . This is attributed to slight differences in the spatial upwelling spread over the seasonal scale within ensemble members. Nevertheless, there is a 0.92 ± 0.01 correlation between each individual simulation and the median. Based on these results, uncertainties associated with the internal variability within our simulations can be disregarded, and the calculated median based on the ensemble members can be used as a representative case for the Hist/RCP8.5 scenario. This reflects the strong influence of the external forcing global model on the ensemble spread, which has also been shown for coupled ocean-atmosphere downscalings for the Northwest European shelf ([Mathis et al., 2018](#)).

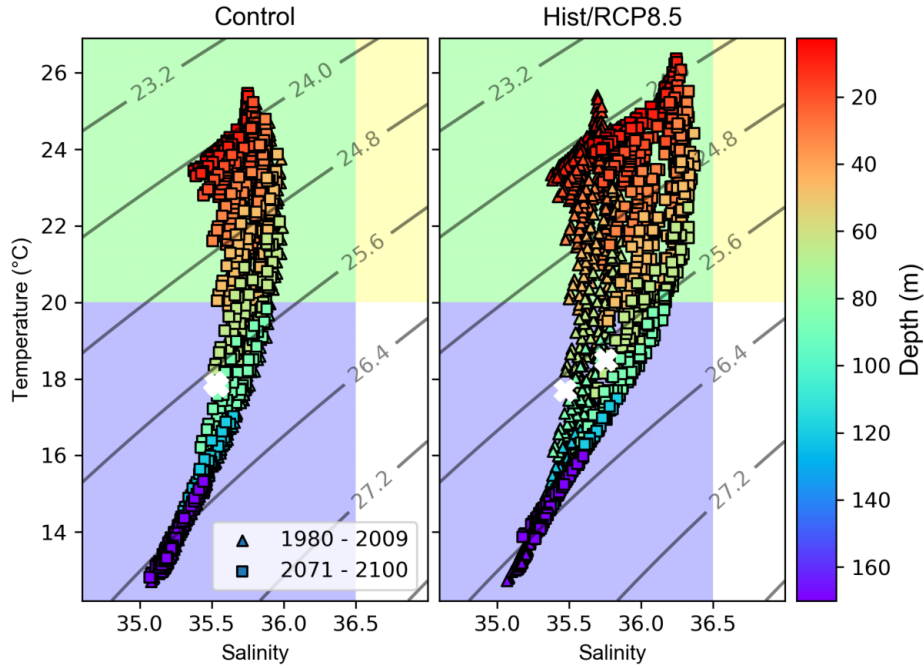


Figure 3.2: T-S diagram of samples extracted along the SBB's shelf break for the Control and Hist/RCP8.5 scenarios. Samples related to the historical climatology (1980 to 2009) are represented by triangles, whereas samples related to the end of century climatology (2071 to 2100) are represented by squares. The color scheme represents the depth at which each data was extracted. The white cross is the centroid of each point distribution, for each evaluated period. Green, yellow and blue backgrounds portray the temperature and salinity boundaries for the Coastal Water, Tropical Water and South Atlantic Central Water, respectively.

3.4.2 Climatic impacts in the SBB

As expected, a clear seasonal signal of the upwelling was found across the SBB under present-day climatic conditions (Fig. 3.4, left panels). This, however, is restricted to the middle and inner shelf regions. During austral summer, upwelling dominates the bottom of the mixed-layer in the central and southern parts of the SBB, with the process being interrupted during winter by the advances of cold atmospheric fronts from the south. The higher upwelling than downwelling rates lead to a dominant upwelling pattern in the inter-annual scale, stronger around the Santa Marta cape (refer to Fig. 3.1 for the location). In contrast, a dipole structure can be seen along the shelf break and the northern sector (i.e., the Cabo Frio region). This dipole structure seems to have a strong correlation with the bottom topography at the shelf break, with downwelling cores followed by upwelling cores as the BC flows south along the ridges. This structure shows a weak seasonality and, essentially, acts as a shelf boundary to the general upwelling found during summer for most of the SBB. At Cabo Frio, specifically, this upwelling extends throughout the whole shelf, leading to stronger upward flow when compared with the remaining of the SBB coastline.

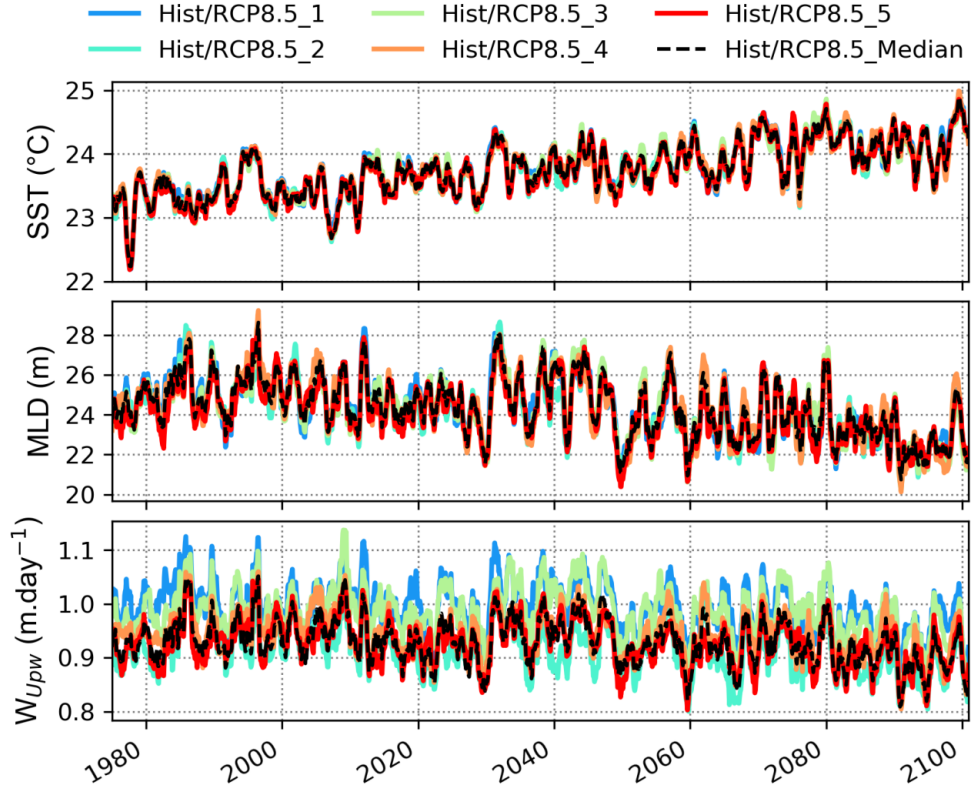


Figure 3.3: Domain-averaged sea surface temperature (SST), mixed-layer depth (MLD) and upwelling velocity at the bottom of the mixed-layer (W_{Upw}). Colored solid lines represent the different ensemble members, whereas the black dashed line represents the median. The chosen domain is depicted in Fig. 3.1.

These results reflect the coexistence of two different upwelling regimes on the inner shelf and along the shelf break of the SBB (Campos et al., 2000).

Anthropogenic climate change impact on the upwelling is assessed through the calculation of the change signal (Fig. 3.4, right panels). We find a statistically significant decrease of the upwelling strength along the shelf break during all periods, showing a weakening of the dipole structure - i.e., positive values of the change signal are associated with downwelling cores and vice-versa. During austral summer, however, a reduction of the upwelling strength is also verified on the middle and inner shelf of the central and southern SBB sectors. The northeastern sector (around Cabo Frio) shows the weakest changes among the evaluated periods.

These strong upward vertical flows at the Cabo Frio region lead to a marked lower SST, in particular during summer, that is also persistent on the inter-annual scale (Fig. 3.5, left panels). In this region, SST is up to 4 °C lower than at the central sector. This is also apparent at the Santa Marta cape, although to a lesser geographical extent. Nevertheless, lower temperatures are found across the whole SBB when compared with the warmer wa-

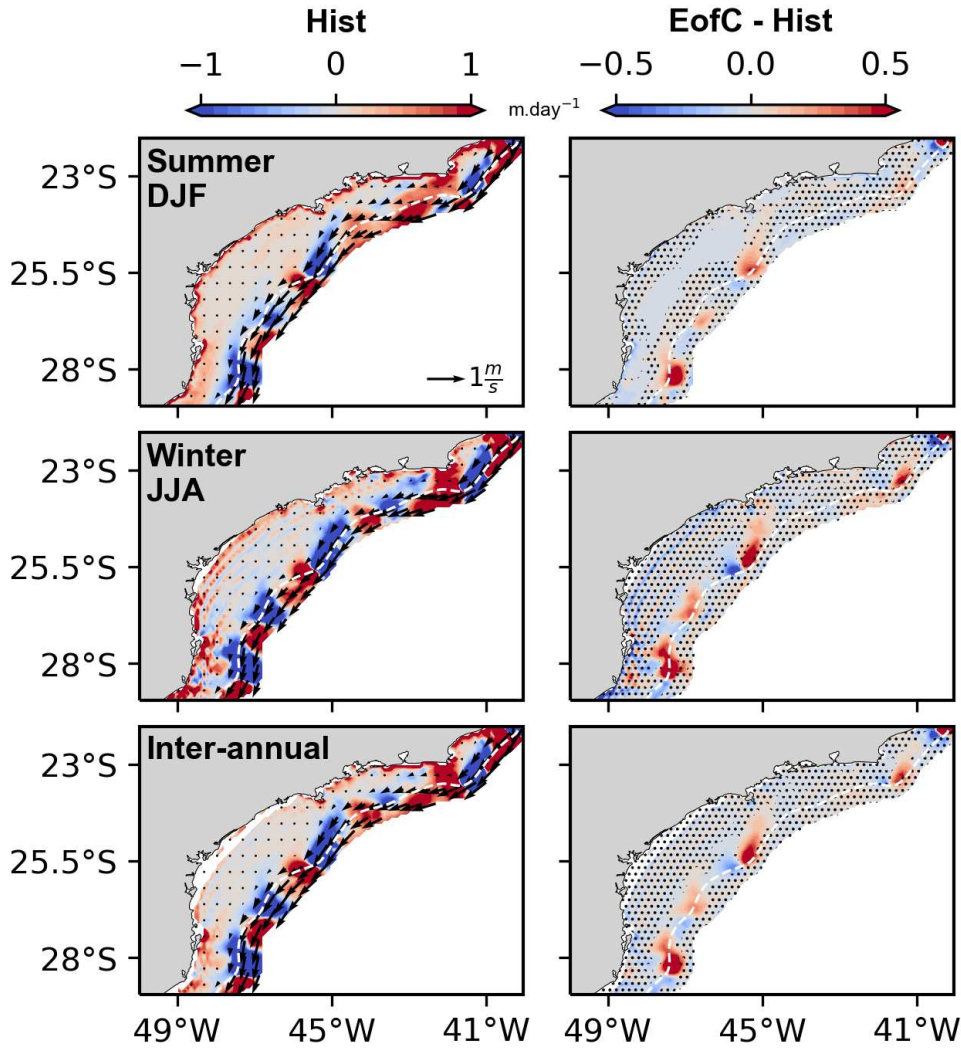


Figure 3.4: Historical climatology of the vertical velocity at the bottom of the mixed-layer (W_{MLD} - 1980 to 2009, left panels) for austral summer, winter and inter-annual scales and their respective projected change signals (EofC - Hist, right panels). Positive values for the climatologies indicate upward flow. Data is shown up to the 1000 m isobath, and the dashed white line identifies the 200 m isobath and marks the shelf break. Hashed regions in the projected change signals indicate where the difference is smaller than the control variability and therefore statistically not significant, and colors need to be interpreted in relation to the direction of the climatological flow. Arrows in the left panels represent the horizontal velocity field at the bottom of the mixed-layer. All values for the W_{MLD} are in meters per day.

ters transported by the BC, reflecting the overall effectiveness of the SACW upwelling in cooling surface waters. On the inter-annual scale, we found the SST across the SBB to vary spatially by up to 1.8°C and exceeding 2°C during summer along the shoreline. These spatial differences are not as strong during winter, although we can still see slightly colder waters in the narrower shelf regions. The change signal at the end of the 21st century also

reflects these regional differences (Fig. 3.5, right panels). Although SST increases across most of the SBB, there is a slight but statistically significant temperature decrease at the northern sector of about 1 °C. This mainly extends between Cabo Frio and Ubatuba (see Fig. 3.1 for location references). The increase in temperature is also smaller along the shelf break, being influenced by the shelf break upwelling regime. In contrast, bottom temperature increases along the shelf break (up to 1.2 °C) but decreases across most of the middle and inner shelf regions (Fig. 3.6, right panels). The historical climatology (Fig. 3.6, left panels), in this case, can be considered a reflection of the SACW spread over the shelf, retreating offshore in winter when compared with the summer season. The projected bottom temperature increase is a reflection of the general warming found previously on the TS-diagram over the ocean-shelf edge (Fig. 3.2), whereas the decreasing temperatures over the shelf indicate a stronger influence of the SACW intruding closer to shore.

In contrast, changes to sea surface salinity (SSS) show a more homogeneous pattern when compared to the SST (Fig. 3.7). We found a statistically significant increase across the whole SBB with a maximum of 0.5 in winter close to the shelf break, with differences between summer and winter smaller than 0.2. The distinction between the SSS increase over the continental slope and the shelf is also much more evident in winter than summer, in contrast to changes in SST. This, combined with the presence of a clear plume signal propagating from the southern sector, indicates the influence of the Plata River Plume discharge in the SBB and suggests its importance as a dynamical feature of this region.

3.5 Discussion

3.5.1 The two upwelling regimes

Our results also reflect the presence of two different upwelling regimes in the SBB (Fig. 3.4). The first regime dominates the inner and middle shelf regions in the central and southern SBB sectors and has a strong seasonality (Fig. 3.4, left panels). Physically, the process has been previously explained by [Castro and Miranda \(1998\)](#), where the prevalent NE summer winds induce offshore surface transport in the SBB, being disrupted during winter by southerly winds associated with the passage of cold fronts. This is the classical Ekman upwelling, and essentially balances the offshore transport of surface TW and CW with the onshore transport of subsurface SACW ([Castro and Miranda, 1998](#); [Lima et al., 1996](#); [Castelao et al., 2004](#)). The numerical experiments of [Campos et al. \(2000\)](#) and the recent works of [Cerdeira and Castro \(2014\)](#), [Castro \(2014\)](#) and [Brandini et al. \(2014\)](#) based on survey data showed how this upwelling regime has an impact across all stretches of the SBB on the seasonal scale, supported by the results found herein.

The second regime, in contrast, dominates the shelf break and the northern sector of

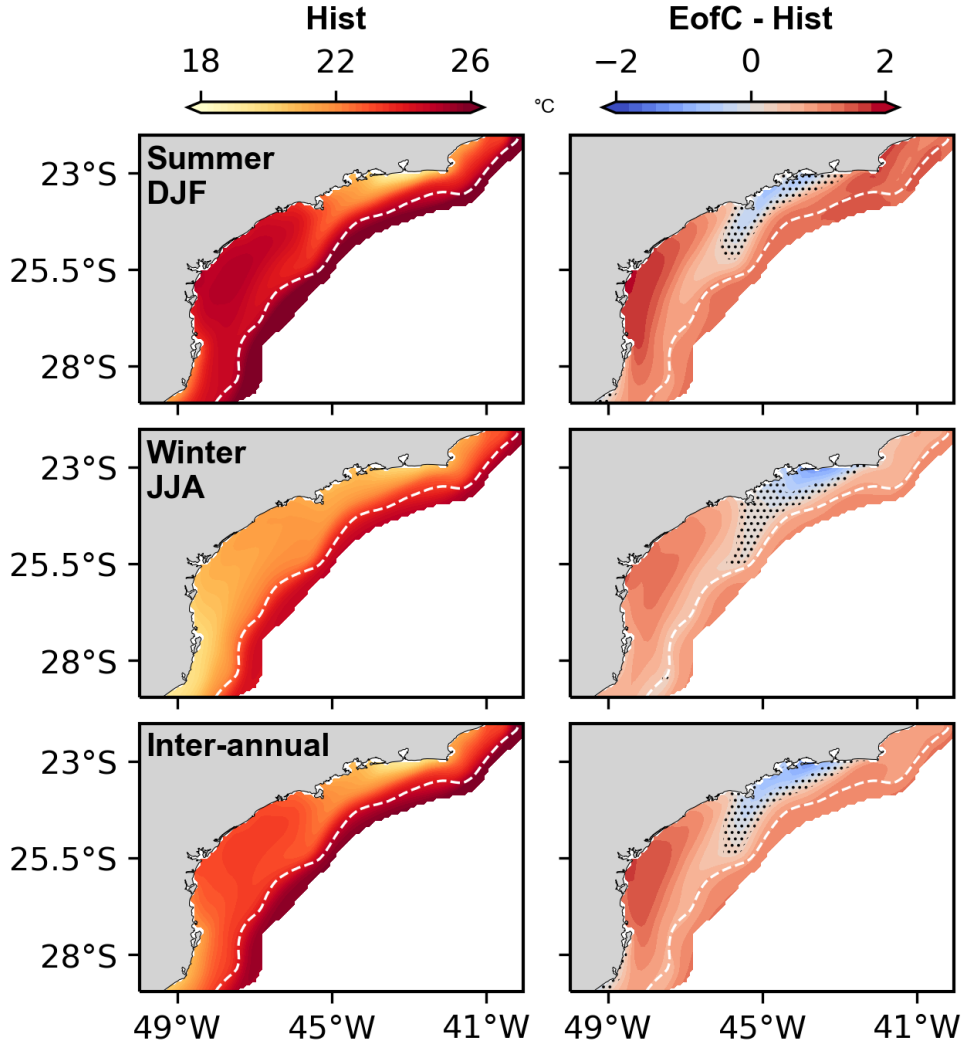


Figure 3.5: Historical climatology of sea surface temperature (SST - 1980 to 2009, left panels) for austral summer, winter and inter-annual scales and their respective projected change signals (EofC - Hist, right panels). Data is shown up to the 1000 m isobath, and the dashed white line identifies the 200 m isobath and marks the shelf break. Hashed regions in the projected change signals indicate where the difference is smaller than the control variability and therefore not statistically significant. All values are in degree Celsius.

the SBB and shows only a weak seasonality (Fig. 3.4, left panels). Campos et al. (1995) first proposed that the shelf break upwelling is driven by cyclonic meanders of the BC. Later, Campos et al. (2000) showed how this shelf break regime co-existed with the Ekman upwelling and was effective year-round, based on a combination of hydrographic data and model results. Meanwhile, Silveira et al. (2000) explained the formation of these cyclonic meanders based on the conservation of potential vorticity (Π). According to these authors, as the BC overshoots the region around Cabo Frio due to the change in coastal geometry, it veers westward to conserve Π . This generates barotropic shear instability and leads to the creation of a topographical Rossby wave that propagates southwestward. This wave then

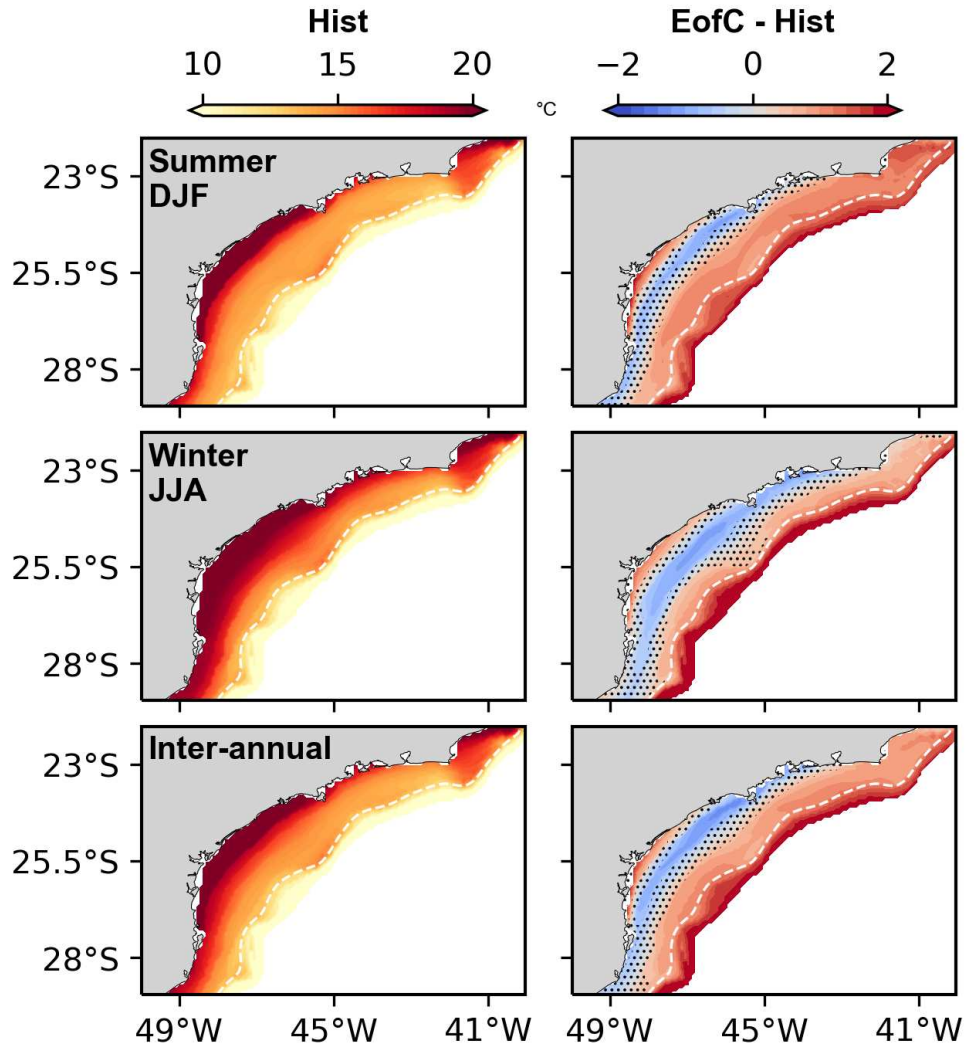


Figure 3.6: Historical climatology of the shelf's bottom temperatures (1980 to 2009, left panels) for summer, winter and inter-annual scales and their respective projected change signals (EofC - Hist, right panels). Data is shown up to the 1000 m isobath, and the dashed white line identifies the 200 m isobath and marks the shelf break. Hashed regions in the projected change signals indicate where the difference is smaller than the control variability and therefore not statistically significant. All values are in degree Celsius.

generates the cyclonic meanders described by [Campos et al. \(2000\)](#), which produce upwelling at their leading edge and downwelling at their trailing edge. More recently, [Palma and Matano \(2009\)](#) did a comprehensive modeling study of the SBB and also identified a dominating role of the BC to the shelf break regime. However, they argued that it is rather its interaction with the bottom topography along the BC path that creates changes of the alongshore pressure gradient and drives the upwelling through the bottom boundary layer. Their proposed mechanism is similar to the one found by [Oke and Middleton \(2000\)](#) for the eastern Australian shelf.

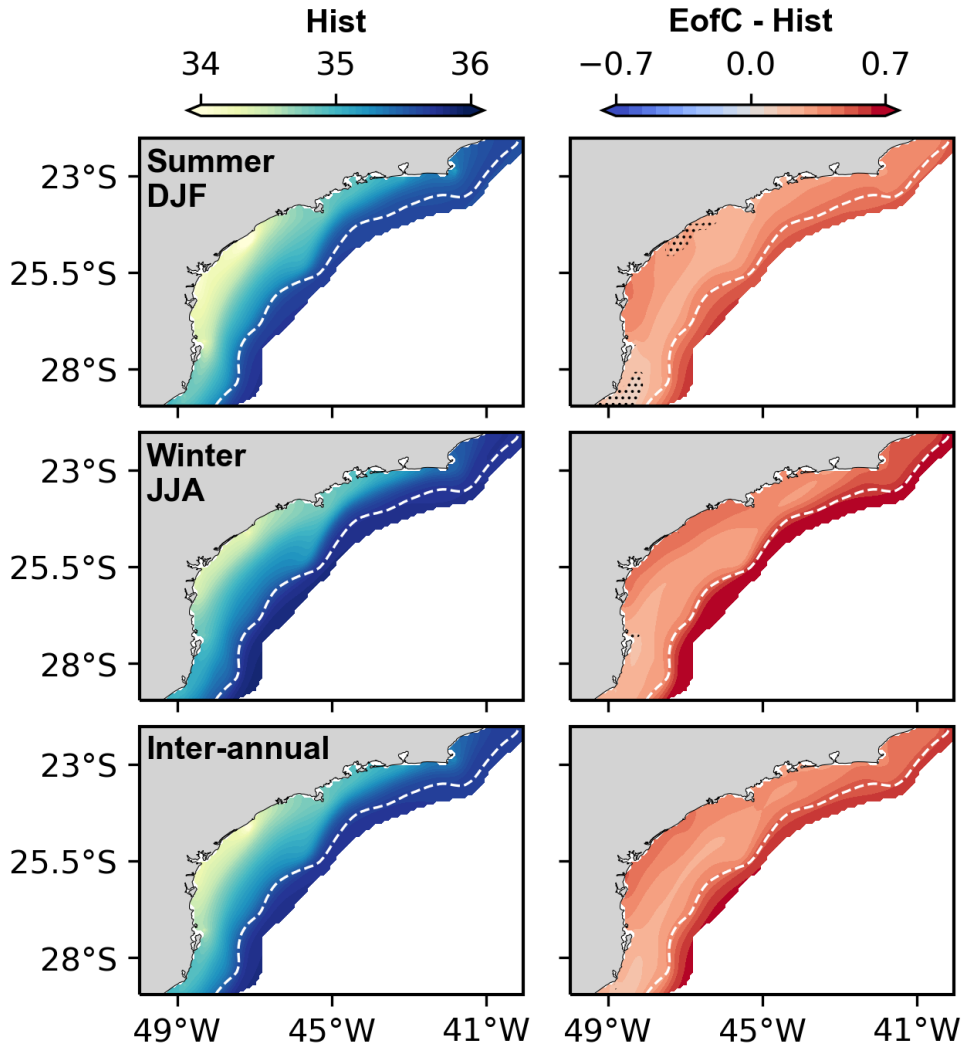


Figure 3.7: Historical climatology of sea surface salinity (SSS - 1980 to 2009, left panels) for austral summer, winter and inter-annual scales and their respective projected change signals (EofC - Hist, right panels). Data is shown up to the 1000 m isobath, and the dashed white line identifies the 200 m isobath and marks the shelf break. Hashed regions in the projected change signals indicate where the difference is smaller than the control variability and therefore not statistically significant.

Given both these explanations and based on our own results, we suggest that the mechanism is a combination of characteristics from both conceptual models. The experiments of [Song and Chao \(2004\)](#) provide the basis for our proposed explanation. They conducted an idealized study on the interaction of a varying bottom topography with a strong boundary current, similar to the conditions found in the SBB, in which a series of ridges can be seen along the 200 m isobath starting around Cabo Frio (see Fig. 3.1). Their results show that as the boundary current flows along the ridge topography, it creates a dipole structure attached to the ridge. This structure consists of a downwelling core upstream and an upwelling core downstream of the ridge. They also related the development of these dipole

structures to changes in the relative vorticity (ζ), producing anticyclonic and cyclonic circulations over the downwelling and upwelling cores as the boundary flow meanders around these bathymetrical features. As a result, these dipoles were fixed in space, as identified in our results as well (Fig. 3.4).

In essence, this would corroborate the basis of [Silveira et al. \(2000\)](#) argument that the potential vorticity drives the shelf break upwelling regime, but not because of the generation of a topographical Rossby wave associated with the BC overshooting the latitude of Cabo Frio. The BC is under geostrophic balance and, as such, has to conserve Π ($\Pi = \frac{\zeta+f}{D}$) as it flows around a varying topography (Fig. 3.7, bottom right). Since its planetary vorticity (Coriolis parameter, f) is always decreasing along its path, local changes in depth (D) have to be mostly balanced by changes in ζ (Fig. 3.8, top panels). This means that it gains positive ζ and spins anticyclonically as it travels upslope, generating a downwelling region. And the opposite is also valid, it gains negative ζ as it travels downslope, spinning cyclonically and generating upwelling. These changes in ζ also account for the meandering of the BC, as observed by [Campos et al. \(1995, 2000\)](#) and [Castelao et al. \(2004\)](#). A similar explanation for topographically induced upwelling has been proposed for the Vietnamese coast ([Hein et al., 2013](#)) and the Hainan coast at the South China Sea ([Su and Pohlmann, 2009](#)). Nevertheless, for our argument to hold, we first have to establish that these ridges are indeed a feature of the local shelf break topography and that they are necessary to produce the shelf break upwelling.

To the first point, figure 4 of [Campos et al. \(2000\)](#) shows the 200 m isobath south of Ubatuba (for locations, see Fig. 3.1). In it, the presence of a ridge is clearly seen, similar to the profile found here. Not only that, but the presence of an upwelling core is seen downstream of this ridge, with no SACW signal upstream of it in any of their three cruises. The dipole structures found in our study can also be seen in their model results from figure 7, where they show the cross-isopycnal velocity, although the shelf break profile was not superimposed in this image. The same ridge can also be seen in figure 13 of [Silveira et al. \(2000\)](#), along with the ridges southeast of Cabo Frio and east of the S. Marta Cape (Fig. 3.1). Based on these results, we are confident in the presence of these ridges as actual topographical features along the SBB and their impact on the upwelling dynamics.

As for whether these features are necessary to produce the shelf break upwelling, it is interesting to compare our results to the ones from [Palma and Matano \(2009\)](#). Looking at their bathymetrical profile along the SBB (their figure 1), we can see that the 200 m isobath is very smooth and presents no features, although the change in coastal geometry around Cabo Frio is preserved. This means that, according to the argument from [Silveira et al. \(2000\)](#), the BC overshooting Cabo Frio should still produce the topographical Rossby wave that creates the cyclonic meanders. However, [Palma and Matano \(2009\)](#) results shown in

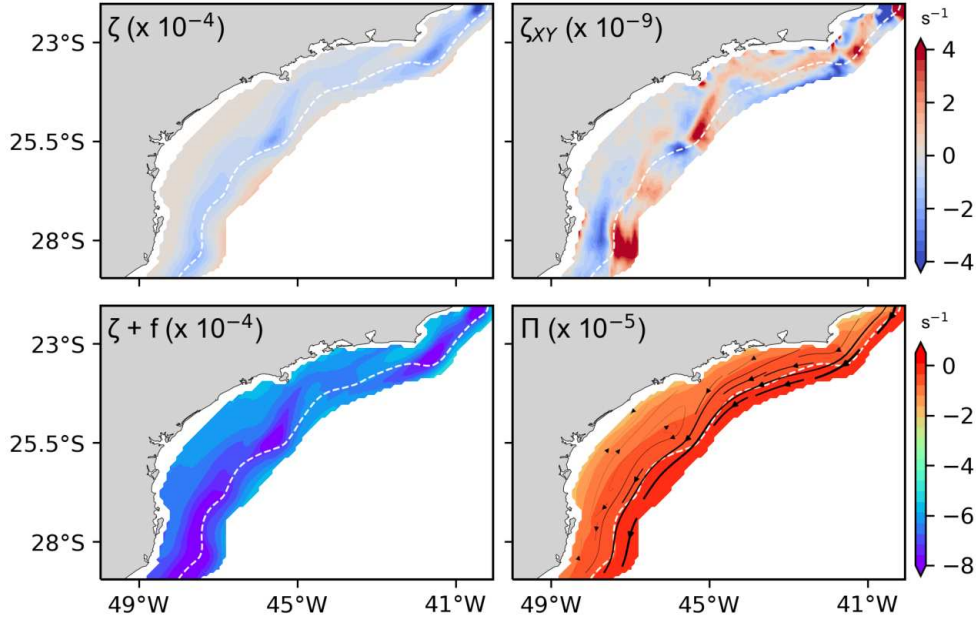


Figure 3.8: Components of the potential vorticity conservation in the South Brazil Bight calculated at the bottom of the mixed-layer for the inter-annual variability case during the historical period (1980 to 2009). Top figures are the relative vorticity (ζ , left) and its tendency (ζ_{XY} , right) and at the bottom are the absolute vorticity ($\zeta + f$, left) and the potential vorticity (Π , right). Streamlines over Π represent the flow, with the varying thickness as an indication of relative flow strength. Data is shown up to the 1000 m isobath, and the dashed white line identifies the 200 m isobath and marks the shelf break.

figure 3 do not indicate any meandering of the BC flow. As a consequence, their upwelling signal is restricted to the northern sector around Cabo Frio, which is then transported southward by the surface flow over the shelf. This suggests that the shelf break upwelling regime is indeed dependent upon the topographical features. Unfortunately, they did not show results for the vertical velocities directly, so we have to limit our comparison qualitatively to the surface behavior of the BC.

Finally, as for the stronger upwelling signal found in the northern sector (Fig. 3.4 and 3.5), the local reduction of the shelf width in front of Cabo Frio advectively accelerates the inshore flow and pushes the upwelled water from the shelf break towards the coastline. This is a process identified by Oke and Middleton (2000) with regards to the East Australian Current and by Cerda and Castro (2014) and Palma and Matano (2009) based on hydrographic climatologies and simulations for the SBB, respectively. Furthermore, it is likely further enhanced by the barotropic instabilities identified by Silveira et al. (2000), as the increased eddy kinetic energy generated in this region (Oliveira et al., 2009) can feed these dipole structures. These processes could contribute to maintain a strong presence of the SACW year-round in the Cabo Frio region (Fig. 3.4), as opposed to the rest of the SBB where the shelf is wider.

3.5.2 Anthropogenic climate impacts to the upwelling regimes

Upwelling strength and duration is expected to increase in the Benguela Current System in the eastern South Atlantic under increased anthropogenic forcing (Wang et al., 2015). Change is mostly attributed to an increase of the alongshore winds over the subtropical South Atlantic (Sydeman et al., 2014). This increase, in turn, is associated with a southward migration of the South Atlantic Subtropical High (Rykaczewski et al., 2015) in response to the expected southward migration of the westerlies over the Southern Ocean (Swart and Fyfe, 2012; Wilcox et al., 2012; Barnes and Polvani, 2013) and the widening of the Hadley circulation (Kang and Lu, 2012; Davis and Rosenlof, 2012; Hu et al., 2018).

To confirm this behavior within our simulations, we calculated the wind speed climatologies for the historical and end of the century periods (Fig. 3.9) over our South Atlantic domain. Although we see no significant changes in the wind speeds associated with the general circulation over the South Atlantic Subtropical High (SASH), there is a clear southward migration of its center of approximately 2° . This is accompanied by a slight increase in wind velocities along the South American coast, as reported by Sydeman et al. (2014), but it also exposes the SBB to the stronger E-NE winds associated with the upper branch of the SASH. With this in mind, we calculated the offshore Ekman transport ($E_k = \frac{\tau_y}{\rho_w f}$) for the SBB based on the alongshore wind stress (τ_y), considering a 45° coastline orientation (Fig. 3.10). We found an increase in the Ekman forcing across the SBB for all periods, albeit much stronger during winter than summer. The exception is in the northeastern sector, where a small reduction can be seen during summer. These results are in line with the global atmospheric trends mentioned above and can also explain the increased spread of SACW over the shelf's bottom indicated by the bottom temperatures (Fig. 3.6). They do not, however, account for the reduction in the W_{MLD} , specially considering that the northeastern sector showed the least amount of significant changes when compared to the rest of the SBB.

On a regional level, increased Ekman forcing leading to increased coastal upwelling is also expected in the Californian upwelling system (Snyder et al., 2003), the Iberian Peninsula (Miranda et al., 2013) and the Canary Upwelling Ecosystem (Sousa et al., 2017), based on the analysis of surface temperature fields. Notwithstanding, we found a reduction of the upwelling strength in the SBB in spite of these general atmospheric trends (Fig. 3.4, right panels). Along the Oman coast in the Indian Ocean, regional heterogeneities in the Ekman transport patterns led to divergent modifications in vertical transport (Praveen et al., 2016), accentuating the importance of local processes in defining variations in local upwelling. In the SBB, the intrusion of the Plata River Plume can be one of such relevant processes. Piola et al. (2005) and Pimenta et al. (2005) identified its northward intrusion up to 24° S, which is congruent to the region of freshwater influence seen in the change

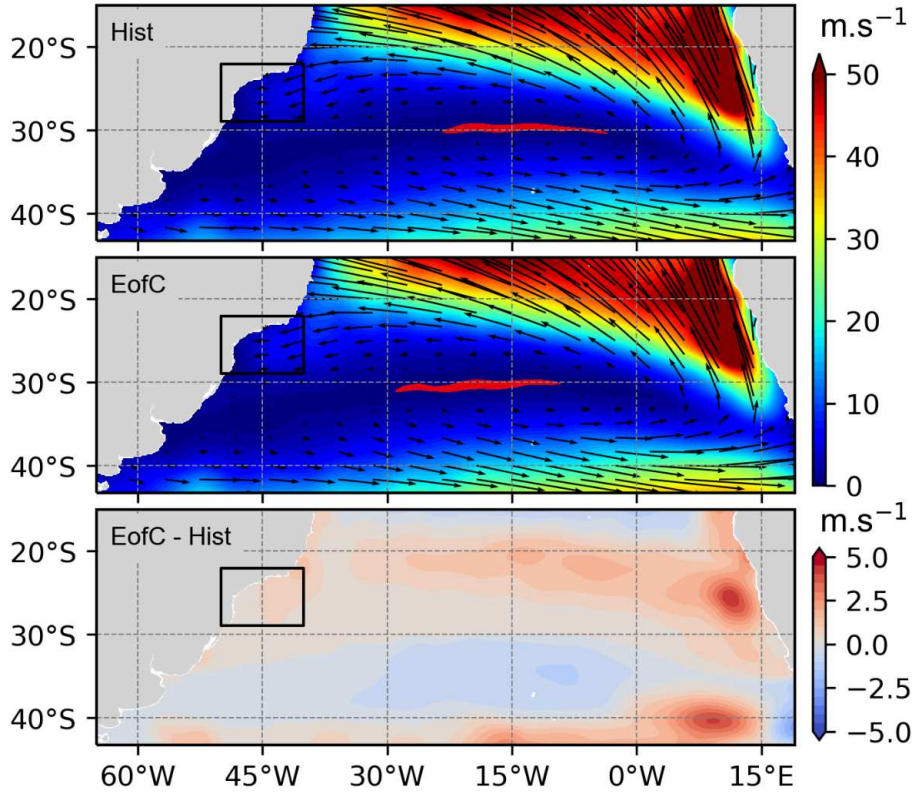


Figure 3.9: Top and middle panels show the wind speed climatology for the historical (1980 to 2009) and end of the century (2071 to 2100) periods over the subtropical South Atlantic, respectively. Bottom panel highlights the change signal between both periods. The black box represents the South Brazil Bight domain analyzed in this study (Fig. 3.1). The red filled contour around 30°S in the upper two panels marks the center of the South Atlantic Subtropical High (wind speeds less than 0.3 m s^{-1}). All values are in m.s^{-1} .

signal in our results (Fig. 3.7). This plume brings fresher waters into the SBB, increasing the water column vertical stability. Its presence in the southern sector and along the middle shelf across all time scales also creates a clear cross-shelf salinity gradient and keeps the overall SSS increase below global projections for the southwestern South Atlantic (IPCC, 2013). However, there is no predicted increase in the Plata River discharge for the RCP8.5, based on the MPI-ESM forcing utilized here, with a slight reduction of its volume input by approximately $100 \text{ m}^3 \text{ s}^{-1}$ at the end of the 21st century. This reduction is not statistically significant when we consider that the standard-deviation for this discharge is above $1000 \text{ m}^3 \text{ s}^{-1}$ and implies that this plume mainly acts as a buffer, reducing the general SSS increase in the SBB but does not contribute to the changes seen in upwelling strength.

Aside from increased alongshore winds and the changes to SSS, anthropogenic climate change is mostly visible on temperatures, primarily affecting the upper 700 m of the water column (IPCC, 2013). This heat input affects the energy budget in the system, which can change the amount available to be converted from potential energy (PE) to kinetic en-

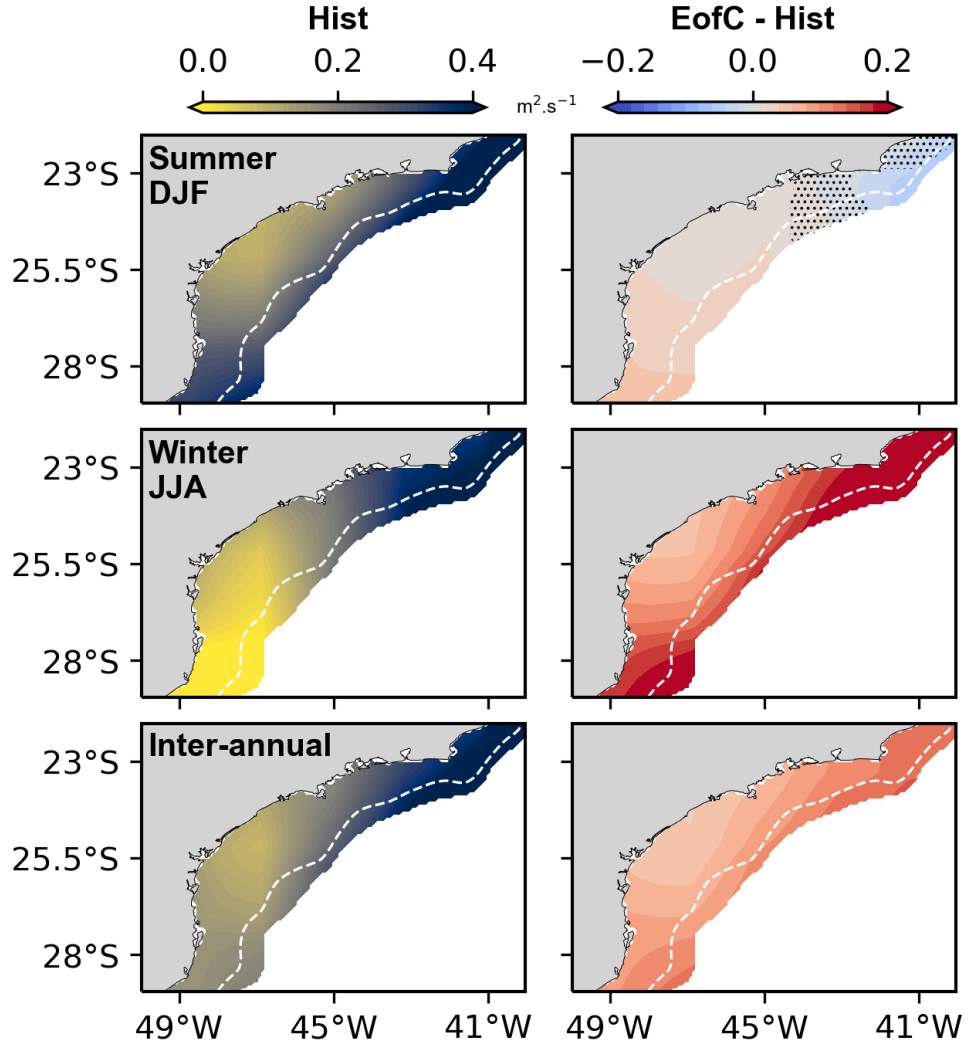


Figure 3.10: Historical climatology of the offshore Ekman transport (1980 to 2009, left panels) of summer, winter and inter-annual scales and their respective projected change signals (EofC - Hist, right panels). Data is shown up to the 1000 m isobath, and the dashed white line identifies the 200 m isobath and marks the shelf break. Hashed regions in the projected change signals indicate where the difference is smaller than the control variability and therefore not statistically significant. All values are in $m^2.s^{-1}$.

ergy (KE) and to induce motion. This is the concept of available potential energy (APE), first introduced by [Lorenz \(1955\)](#), and is considered a measure of the water column stability. We calculated the APE along the SBB as the change in PE between the actual state of water masses found within the model results and a reorganized stable water column (Fig. 3.11). This reorganization consists of rearranging vertical layers of the model, so that the highest densities are found at the bottom and the minimum PE state is achieved (i.e., the background potential energy). A more detailed description of this method can be found in [Urakawa et al. \(2013\)](#). We can see a decrease in APE across the inner and middle shelf regions at all temporal scales, indicating that the water column is becoming more stable

under increased surface warming. For the winter and inter-annual scales, this means that the increase in the Ekman forcing is balanced by the higher stability and we see no significant changes to W_{MLD} (Fig. 3.4, right middle and bottom panels). For the summer period, on the other hand, the smaller increase in E_k is not enough to balance the increased stability and we see a weakening of W_{MLD} .

Urakawa and Hasumi (2009) showed how Ekman upwelling/downwelling represents a conversion from KE to PE, as the flow has to pull up/push down a heavier/lighter water parcel. This means that the change in water mass depth must come with gain/loss of PE, which is supplied by the conversion from KE. Under increased surface warming, the surface layer becomes lighter and requires more KE converted to PE to disturb the water column stability and pull-up the heavier water mass below. In our scenario, the KE input from the enhanced wind field is insufficient to overcome the stronger water column stability, decreasing the amount of water that is upwelled towards the mixed-layer. Since the surface layer is still under increased Ekman forcing, the additional transport of surface water has to be compensated across a larger portion of the shelf, which leads to the wider bottom intrusion of SACW seen through the bottom temperatures (Fig. 3.6). This could lead to an increase in nutrient availability at deeper layers and enhance the deep chlorophyll maximum identified by Brandini et al. (2014), but reduces the input of SACW to the mixed-layer. Since we have not involved a biogeochemistry or ecosystem model in our simulations, a more targeted study considering these impacts on nutrients dynamics over the shelf would be necessary to properly clarify these questions and its consequences to the shelf productivity.

Although the relation between increased Ekman forcing and water column stability explains the weakening of the Ekman upwelling, it does not satisfactorily address the weakening of the shelf break upwelling as well. This is because we still see a decrease in W_{MLD} in austral summer as well as winter, even though the APE change over the shelf break suggests a less stable water column during summer, particularly in the northern sector (Fig. 3.11). Both our results (see section 3.5.1) and previous studies (Campos et al., 1995, 2000; Silveira et al., 2000; Palma and Matano, 2009) identify a close relation between this upwelling regime and the BC, so it behooves us to look at the BC dynamics over the 21st century (Fig. 3.12). A decreasing trend south of 25°S can be clearly identified, which agrees spatially with the strongest decrease of the shelf break upwelling seen in our results (Fig. 3.4). Not only that, but the slight increase in BC transport in the northern sector could explain why we found mostly no differences for this sector, or even a slight increase of the upwelling at the northern shelf break. However, these changes are mostly small and within our uncertainty range when considering our Control variability, which likely stems from the lack of a clear increase in the SASH wind circulation (Fig. 3.9). In this case, these trends found on the BC transport would reflect its adjustment to the new gyre position. It would also suggest

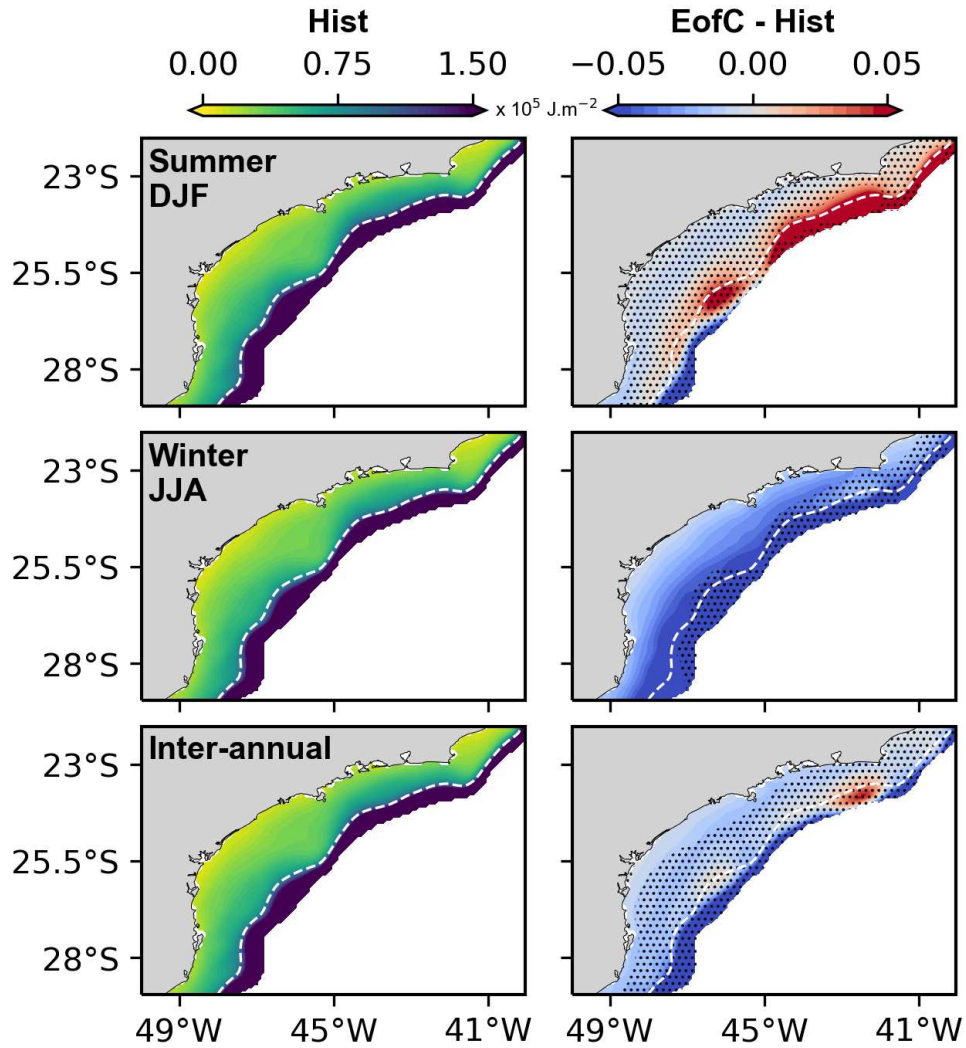


Figure 3.11: Historical climatology of the available potential energy (1980 to 2009, left panels) for summer, winter and inter-annual scales and their respective projected change signals (EofC - Hist, right panels). Data is shown up to the 1000 m isobath, and the dashed white line identifies the 200 m isobath and marks the shelf break. Hashed regions in the projected change signals indicate where the difference is smaller than the control variability and therefore not statistically significant. All values are in J.m^{-2} .

that the shelf break regime is highly sensitive to changes in the BC transport. This would be a direct consequence to the dependence of the shelf break upwelling to changes in the relative vorticity, as increasing the BC would lead to increased flow divergence.

Finally, both upwelling regimes have a clear impact on surface warming (Fig. 3.5, right panels). In general, the maximum end of century SST increase over the shelf (1.8°C , Fig. 3.4) is lower than the projected 2°C to 3°C increase over the SW South Atlantic for the RCP8.5 scenario (IPCC, 2013). The consistent upwelling of colder SACW seems to dampen the impact of increasing radiative forcing, even under a strong climate scenario.

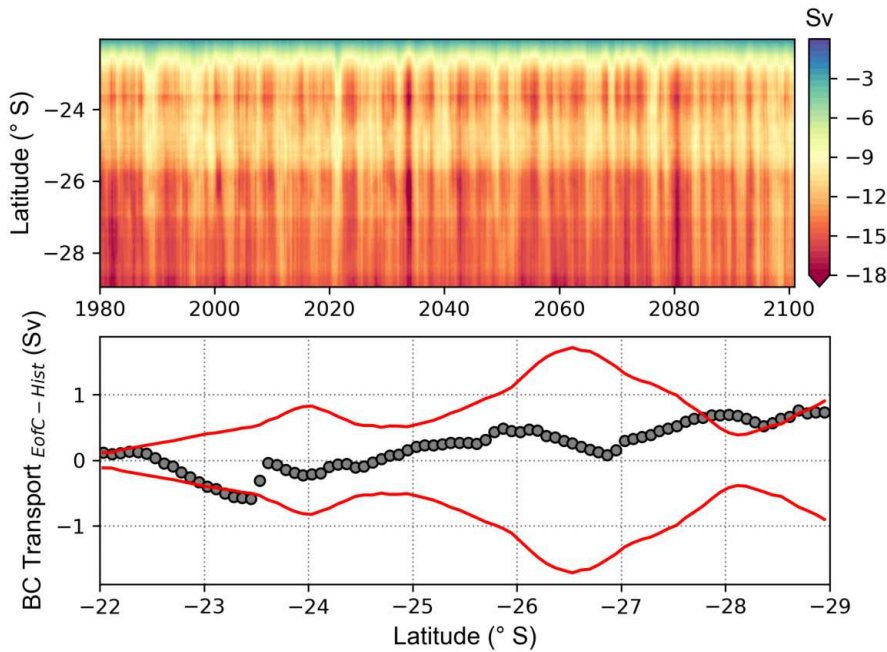


Figure 3.12: At the top, Hovmöller diagram of the Brazil current transport (in Sverdrups) along the extension of the South Brazil Bight during the analyzed time period (1980 to 2100). At the bottom, differences between its climatological transport at the end of the century (EofC, 2071 to 2100) and the historical period (Hist, 1980 to 2009). The red solid line in the bottom graphic is the confidence interval calculated based on the control simulation. Samples within the red region are within our uncertainty range based on the control. Negative differences indicate a strengthening of the BC transport whereas positive values indicate weakening, since the Brazil current flows southward.

Similar results were found by [Miranda et al. \(2013\)](#) in the Iberian Peninsula, by [Praveen et al. \(2016\)](#) along the Oman coast and by [Sousa et al. \(2017\)](#) in the Canary upwelling system. The smaller SST increases over the shelf break when compared to the middle shelf would also suggest that the BC upwelling is a stronger mechanism in dampening the surface warming. This is even more striking over the NE sector of the SBB, where we see a decrease in SST. Our results suggest that SST in this region is strongly influenced by the SACW upwelled at the adjacent shelf break and advected towards the coast. This is then spread SW by the surface circulation along the SBB, with this pathway having also been identified by [Cerdeira and Castro \(2014\)](#) on hydrographic data. Thus, the decrease in SST between Cabo Frio and Ubatuba could be a direct consequence of the increase in BC transport around 23°S (Fig. 3.12), with this water being transported back to the shelf break, south of Ubatuba. This would make the central SBB region more susceptible to global warming, since it would mainly be affected by the Ekman upwelling, which is less capable of compensating the increased warming, thus leading to higher SST increases in this region.

3.6 Conclusions

We presented further evidence of two distinct upwelling regimes in the SBB. The first is driven by the alongshore winds and represents the classical Ekman upwelling, whereas the second occurs mainly along the shelf break and is driven by relative vorticity, as the BC steers around the shelf edge. These two regimes would co-exist year-round and contribute to the overall upwelling of SACW in the SBB, although the Ekman upwelling has a stronger seasonal component. For the northern sector of the Bight, however, the shelf break upwelling acts as a significant year-long source of SACW, affecting the shelf region up towards the coastline.

During the 21st century, we found a general weakening of both upwelling regimes, although this behavior is in disagreement with what has been found in other systems worldwide. In our simulations, these reductions are mostly a response to increased water column stabilization due to the surface warming and a small reduction of the BC transport south of 25° latitude. This evidences the importance of local processes in assessing the response of coastal environments to global climate change. Most upwelling studies rely on indexes derived either from temperature differences between the coastal and oceanic zones, or on the strength of the overlaying winds. As we demonstrated for the SBB, we still found a reduction of vertical velocities even under an increased offshore Ekman forcing, although we also found evidence of increased bottom spread of SACW over the shelf. In this light, we believe that an accurate assessment in localized upwelling regions has to consider a combination of local atmospheric forcings and ocean variables to take regional responses into account.

In the SBB, the combination of these two upwelling regimes dominates the SST response. SST increases over most of the shelf, but is lower than projections derived from Earth System Models under the RCP8.5 scenario. This is a direct response to the SACW upwelling that dampened the potential warming, up to the point of reducing surface temperatures over the northeastern sector when compared to present-day conditions. Over the middle and inner shelves in the central and southern sectors of the SBB, where the SACW signal was weaker, SST increases were similar to global projections of almost 2 °C under RCP8.5 conditions. As for the behavior at the northern sector, the SST decrease seems mostly driven by a slight strengthening of the BC at around 23° latitude, which in turn is driven by an adjustment of the BC flow to a southward migration of the Subtropical High. This interaction highlights how sensitive the shelf break upwelling is to small variations of the BC transport and how important the BC response to anthropogenic climate change is to the upwelling in the SBB. Additional sensitivity studies focusing on isolating the effects promoted by the BC could shed further light into its response at the Cabo Frio region.

Chapter 4

Response of the Brazilian Shelf's Stratification to a Strong Warming Scenario

This chapter has been submitted to the
Journal of Geophysical Research: Oceans
and is currently under review.

Key Points

- We found the South Brazil Bight to be the most susceptible region along the Brazilian shelf to anthropogenic climate change
- On a regional scale, strongest changes in the water column stratification are driven by increased bottom intrusion of SACW
- Even in regions with no net change in stratification, the balance between governing physical mechanisms may still undergo shifts

4.1 Abstract

Earth System Models predict an overall increase in ocean stratification, which can reduce the upper ocean's primary production. Shallower depths and cross-shelf exchange processes, however, modify the response of shelf seas and make the inclusion of regional processes a necessity when evaluating local anthropogenic climate change impacts. We investigate the response of the Brazilian shelf's stratification to a strong warming scenario (RCP8.5) performing a high-resolution ($1/12^\circ$) simulation for the South Atlantic Ocean. In contrast to the global expectation of stronger impacts in the tropical Atlantic, changes in stratification are dominant along the subtropical Brazilian coast. We found a general increase in strength and a shallowing of the pycnocline, with an increase of the potential energy anomaly in the mid-to-inner shelf regions and a decrease towards the open ocean. Over these regions, stratification responded to the increased bottom intrusion of South Atlantic Central Water due to a stronger offshore Ekman forcing, driven by the poleward migration of the South Atlantic Subtropical High. In the tropical Brazilian waters, where this bottom intrusion does not occur, changes are mostly within the range of natural variations and driven by increased surface warming. Of note is that temperature will dominate stratification around the Patos Lagoon across all seasons at the end of the 21st century, as opposed to only during summer in the recent past. In a region where no significant long-term impact was found, this highlights that increased emissions can alter the balance between driving mechanisms even when no net impact is apparent.

4.2 Plain language summary

Models that simulate the global ocean under increasing atmospheric CO₂ concentrations predict more stratified conditions at the end of the 21st century, limiting the exchange of properties between the water column's bottom and surface layers. However, these models cannot account for all relevant physical processes near the coast because of their coarse spatial resolution. In our study, we simulate the South Atlantic Ocean in finer detail and

investigate possible impacts of climate change to the Brazilian coastal waters. In agreement with global projections, we find that the water column tends to become more stratified. In contrast, this process is more effective along the southeastern and southern coast, as opposed to northern and northeastern Brazil as projected by global models. In the north, changes are a consequence of increased warming of surface waters. On the other hand, this warming is combined with stronger winds along southern Brazil, pushing more cold water towards the shore through the bottom layers. Together, these processes promote stronger changes to the dynamics of coastal waters, and is specially effective between Rio de Janeiro and Florianópolis. This makes waters in southeastern Brazil more susceptible to climate change.

4.3 Introduction

Shelf seas are strongly influenced by forcing dynamics from the atmospheric, terrestrial and adjacent deep ocean environments, making them specially vulnerable to anthropogenic climate change. Among those impacts, increased stratification can lead to the decoupling between surface layers and deeper waters, with consequences to biogeochemical processes (Capotondi et al., 2012), such as nutrient supply to the euphotic layer from deeper waters. On a global scale, Earth System Models (ESMs) predict a consistent trend of increased stratification and a consequential decrease in primary production, brought about by declining nutrients concentrations in the mixed-layer (Fu et al., 2016). This increased stratification seems to be mostly connected with increased surface temperatures, specially over tropical regions where the strongest ocean warming is projected (Capotondi et al., 2012; IPCC, 2013). This can be valid even in regional seas, as Hordoir and Meier (2012) found only a small contribution to changes in stratification from modifications of the overlaying wind field in the Baltic Sea, with changes in temperature as the main drivers. Under a strong climate forcing scenario, such as the RCP8.5 (IPCC, 2014), these changes are even expected to accelerate after the 21st century (Randerson et al., 2015). Shelf seas, however, can respond differently than the deeper open ocean due to the shallower water depths and cross-shelf exchange processes, as Holt et al. (2010, 2018) and Mathis and Mikolajewicz (2020) demonstrated for the North Sea.

ESMs predict an increase in stratification across the whole Brazilian shelf, with some models indicating a smaller impact over southeast and south Brazil (Fu et al., 2016). Nevertheless, these results reflect the response of large-scale models that tend to under-represent regional processes, and no high resolution studies have been conducted that take those processes into account. For example, over the Abrolhos Shelf (Fig. 4.1), Pereira et al. (2005) found positive density anomalies on its northern bank that pointed towards stronger downwelling trends. On its southern bank, on the other hand, evidences of upwelling led to

stronger stratified conditions. Over the South Brazil Bight (Fig. 4.1), [Castro \(2014\)](#) found a clear cross-shelf gradient, with increasing bulk stratification towards the open ocean. Nevertheless, response to anthropogenic climate change in these regions from ESMs tends to be spatially homogeneous ([Capotondi et al., 2012](#); [Fu et al., 2016](#)).

Over most of the Brazilian shelf, the water mass structure is dominated by the presence of Tropical Water (TW) and South Atlantic Central Water (SACW), transported along the shelf break by the Northern Brazil Current and the Brazil Current (NBC and BC, respectively). In turn, the onshore intrusion of SACW plays an important role in the fertilization of the shelf, in particular the South Brazil Bight, see for example [Castro et al. \(2006\)](#). In locations where coastal systems are dominant (e.g. estuaries), the dilution of TW by the local freshwater discharge creates the Coastal Water (CW) ([Castro et al., 2006](#); [Piola et al., 2018](#)), characterizing one of the locally generated low salinity water masses. Another low salinity water mass is normally found south of the Sta. Marta Cape (see Fig. 4.1). This is a low-salinity plume associated with the Plata River discharge (PW) and the Subtropical Shelf Water (STSW), which results from the mixing of PW with TW and SACW ([Piola et al., 2000](#)). During strong southerly wind events, usually associated with cold fronts ([Castro and Miranda, 1998](#)), PW can be found inside the SBB northward of 28°S ([Piola et al., 2000, 2005](#); [Möller et al., 2008](#)). It is the different combination of these water masses and the interaction between their physical drivers that governs the stratification along our study site.

Recently, [de Souza et al. \(2020\)](#) showed how stronger alongshore wind stresses at the end of the century did not necessarily translate into increased vertical fluxes from deeper waters towards the mixed-layer, as the enhanced offshore Ekman forcing was sustained by increased stratification. Their results, however, were restricted to the South Brazil Bight and focused on the SACW upwelling process. Our goal in this study is to deepen the understanding of changes in stratification due to anthropogenic climate change by considering modifications to the water column as a whole as well as in main pycnocline characteristics, applying this analysis to the whole Brazilian shelf. To this end, we downscale outputs from the Max-Planck Institute Earth System Model - Mixed Resolution (MPI-ESM-MR) to the South Atlantic ocean using a high resolution (1/12°) ocean model (HAMSOM), under a strong warming scenario (RCP8.5). Impacts on potential energy anomaly, along with changes in pycnocline characteristics and surface temperature and salinity, are then used to cluster the different regions along the shelf according to their projected response to climate change at the end of the 21st century.

A brief description of the modeling framework and the data analysis procedures alongside the clustering algorithm employed can be found in sections 4.4.1 and 4.4.2, respectively. Anthropogenic climate change impacts to the region are shown in section 4.5.1 and dis-

cussed within the scope of regional processes and global trends in section 4.6.1. The results from the clustering procedure are found in section 4.5.2, with the relevance of each cluster and its characteristics discussed in section 4.6.2. Concluding remarks are given in section 4.7.

4.4 Methods

4.4.1 Modeling framework

On the global scale, our simulations are forced by the atmospheric and oceanic outputs from the Max-Planck Institute Earth System Model - Mixed Resolution (MPI-ESM-MR - Giorgetta et al., 2013). They are used to feed a high-resolution regional model of the South Atlantic at $1/12^\circ$ using the HAMburg Shelf Ocean Model (HAMSOM - Backhaus, 1985; Pohlmann, 1996, 2006), with a focus on resolving the upper-ocean circulation. Details on this framework can be found in de Souza et al. (2019). We focus on the Brazilian shelf southeast of the Amazon, limited offshore by the 200 m isobath (Fig. 4.1).

Originally, five ensemble members for the RCP8.5 scenario (IPCC, 2014) were produced for the regional South Atlantic domain, by slightly varying initial conditions (by $\approx 1\%$) in HAMSOM. This was done to account for the internal variability of the regional model system, but was shown to have negligible variance in comparison to the response to the prescribed external forcing from the global model (de Souza et al., 2020). Based on the results from this previous study, we follow the same approach here and analyze the data pertaining to the median of all ensembles. Aside from the RCP8.5 simulations, we also performed a control run based on constant pre-industrial GHG concentrations (IPCC, 2013, 2014). This control simulation allows us to estimate the natural variability's range without the anthropogenic forcing and derive a significant threshold for the imposed climate change signal. Model results are stored as daily outputs, but averaged into monthly means for the subsequent analysis.

4.4.2 Data analysis

Our analysis is focused on the impact of anthropogenic climate change to the water column stratification across the Brazilian shelf, using the potential energy anomaly (ϕ_{PE}) as a proxy. This property, first suggested by Simpson (1981), reflects the amount of energy necessary to fully mix the water column and has been extensively used both for large-scale dynamics (e.g. Yamaguchi et al. (2019) for the North Pacific) and coastal seas (e.g. Holt et al. (2010) for the North Sea). They do not, however, provide further information on vertical changes to cline characteristics. To account for these changes, we additionally calculate the maximum pycnocline gradient and its depth ($\nabla\rho_{max}$ and $\nabla\rho_{depth}$, respectively) across

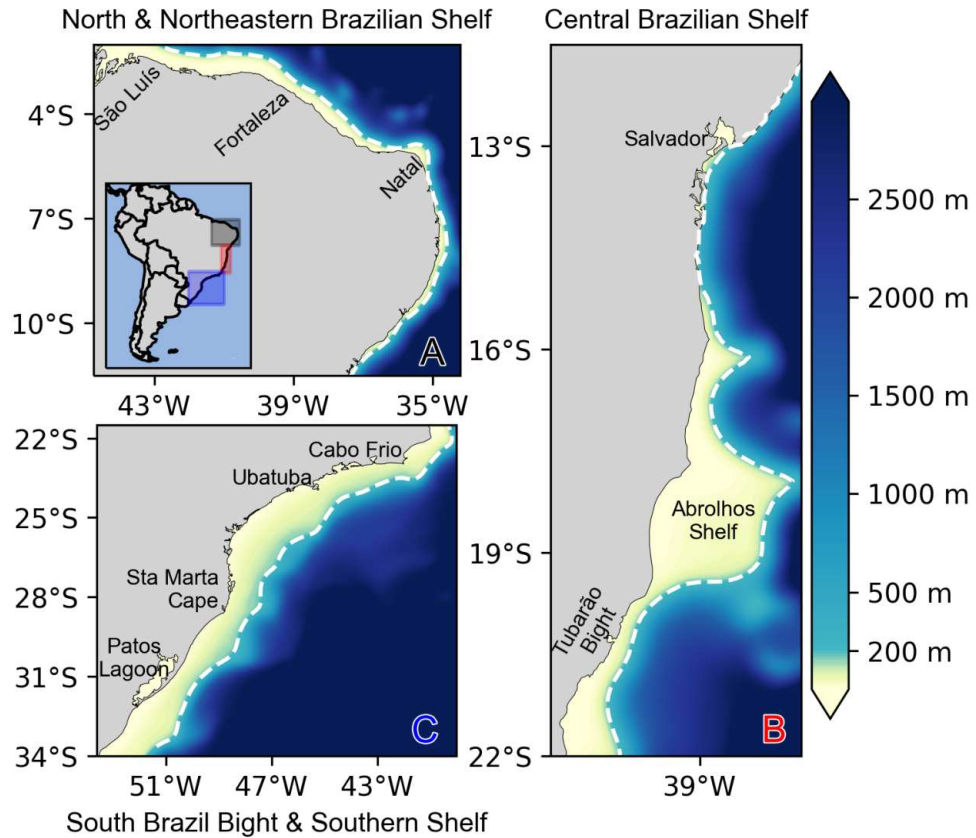


Figure 4.1: Bathymetry along the Brazilian coastline (in meters). The shelf is sectioned in three sections to allow an easier visualization, and each lettered subplot is color-referenced on the general South America inset in subset A. For subplot C, the South Brazil Bight is the region between Cabo Frio and the Sta. Marta Cape, whereas the Southern Shelf extends beyond that to the end of the domain. The dotted line represents the 200 m isobath and marks the position of the shelf break.

the Brazilian shelf, similarly to how [Mathis and Pohlmann \(2014\)](#) did for the North Sea in regards to anthropogenic impacts on the thermocline. In our case, however, using the pycnocline allows us to account for the effects of long-term changes in both temperature and salinity in this region.

Our estimations of future changes are based on two distinct time intervals corresponding to a historical (HIST, from 1980 to 2009) and end of century (EOFC, from 2071 to 2100) climatology, and all analysis are performed for each model cell independently. Change signals are defined as the difference between both climatologies (EOFC - HIST), and is considered significant when its values is above the natural variance threshold derived from the control simulation. This threshold is estimated by computing the climatology within every possible 30-year slice between 1980 and 2100 using a one-year sliding window. The variance between those climatologies is doubled to increase confidence in our results and multiplied by 1.96 to derive a 95% confidence level, following the procedure

of Mathis et al. (2018). Aside from seasonal changes, long-term impact is estimated on the inter-annual scale after applying a 12-months running mean over the monthly data. Similarly as for the calculation of the change signal's confidence interval, a running 30-yr trend over the RCP8.5 scenario is used to gain more insight into the temporal evolution of the shelf's response.

Furthermore, to identify and classify common regional aspects, anthropogenic impact along the Brazilian shelf is clustered using Self-Organizing Maps (SOM - Kohonen, 1990, 2001). These clusters reflect regions with similar impacts not only to the ϕ_{PE} , but also take into account changes in the pycnocline characteristics ($\nabla\rho_{max}$ and $\nabla\rho_{depth}$) and in the sea surface temperature and salinity (SST and SSS, respectively). In literature, SOM has been used to establish biogeochemical provinces in the world's oceans (Landschützer et al., 2013) and along the continental margins (Laruelle et al., 2017), to identify dominant patterns in N_2O air-sea exchange (Lessin et al., 2020) and to extract patterns along the Loop Current associated with sea surface height variability (Liu et al., 2016), to name a few examples. Further applications can be found in Lobo (2009).

For each of our input properties, we ran SOM considering the monthly change signal as opposed to the long-term residuals, so the analysis is able to take into account any significant seasonal changes. Each variable was also independently normalized to avoid the magnitude of any one property dominating the analysis. At the end, each evaluated cell along the shelf has 12 time steps over a set of five properties, yielding 60 training samples per location. These are then used to train the SOM's neural network, which calculates the euclidean distance between those samples' hyper-parameter space and the SOM's neurons, assigning a cluster value for each cell along the shelf based on their closest SOM neuron. The number of neurons, hence the final number of clusters generated, is chosen based on iterations of several different configurations and a portion of these results can be seen in section 4.5.2. Finally, a representative level of impact for each property is defined in each cluster, along with its standard-deviation.

4.5 Results

4.5.1 Anthropogenic impact on stratification

We used the potential energy anomaly (ϕ_{PE}) as a measure of the vertical stratification across the Brazilian shelf and calculated the historical climatologies and the change signal for austral summer (December, January and February - Fig. 4.2, left panels), austral winter (June, July and August - Fig. 4.2, right panels) and the inter-annual scales (Fig. 4.3, left panel). Overall, the strongest impacts are found in winter, although the shelf in general is more stratified during summer. The north and northeastern shelf is comparatively well-

mixed during both seasons when we consider the rest of the domain, and contrasting small changes in ϕ_{PE} during both seasons leads to only a slightly more vertically stratified water column in the inter-annual scale. Nevertheless, a large portion of these changes is not significant when we account for the control variability (Fig. 4.3, left panel). Similar to northern Brazil, the central shelf shows mostly a well-mixed water column with a strong horizontal gradient along the shelf break and higher ϕ_{PE} in the southeastern end of the Abrolhos shelf. The latter region also shows a significant increase in ϕ_{PE} at the end of the century, mostly driven by changes in summer. Finally, the shelf along southern Brazil shows a clear cross-shelf ϕ_{PE} profile, suggesting the predominance of well-mixed conditions on the inner shelf. The extent of the well-mixed region, however, is more restricted during summer and extends further into the middle shelf during winter. In terms of anthropogenic impact, this shelf regions also show a more distinct behavior that persist across all temporal scales. In the inner to middle shelf areas, the water column tends to become more vertically stratified, whereas it becomes more less stratified from the middle shelf towards the shelf break and around the northern sector of the South Brazil Bight (around Cabo Frio). At the very south of our domain, below the Patos Lagoon, the water column becomes more well-mixed across all time periods evaluated, although changes are mostly within our control range, i.e. insignificant.

Aside from its impact on the ϕ_{PE} , increased GHG emissions lead to an overall increase in the maximum pycnocline gradient ($\nabla\rho_{max}$) as well as to shallower pycnocline depths ($\nabla\rho_{depth}$) across the shelf, as can be seen in Fig. 4.3 (central and right panels) for the inter-annual scale. For both properties, the seasonal signals (not shown) essentially have the same pattern as for the inter-annual scale, with slightly stronger gradients during summer and a shallower pycnocline in winter. Similarly as for the ϕ_{PE} , changes are mostly insignificant in north and northeastern Brazil, where the predominantly well-mixed conditions during the historical climatology indicate a lack of a clear pycnocline. The pycnocline strength at the middle to outer Abrolhos shelf tends to increase at the end of the century without a significant change of its depth. The strongest impacts are found along southern Brazil, where the pycnocline can strengthen by $\approx 50\%$ over the inner shelf and become shallower by up to 10 m. On the other hand, no cross-shelf pattern is identified and changes are mostly spatially homogeneous.

4.5.2 Clustering impacts across the Brazilian shelf

The Brazilian coastline measures over 8000 km, with continental shelf widths between 10 km to 330 km (Castro et al., 2006). Nevertheless, as seen from our results, some aspects of anthropogenic impacts show general similarities over large areas. To capture those similarities, we aggregate regions into clusters using self-organizing maps (SOM). This, in turn, allows us to define a set of representative impacts' magnitude and range over our

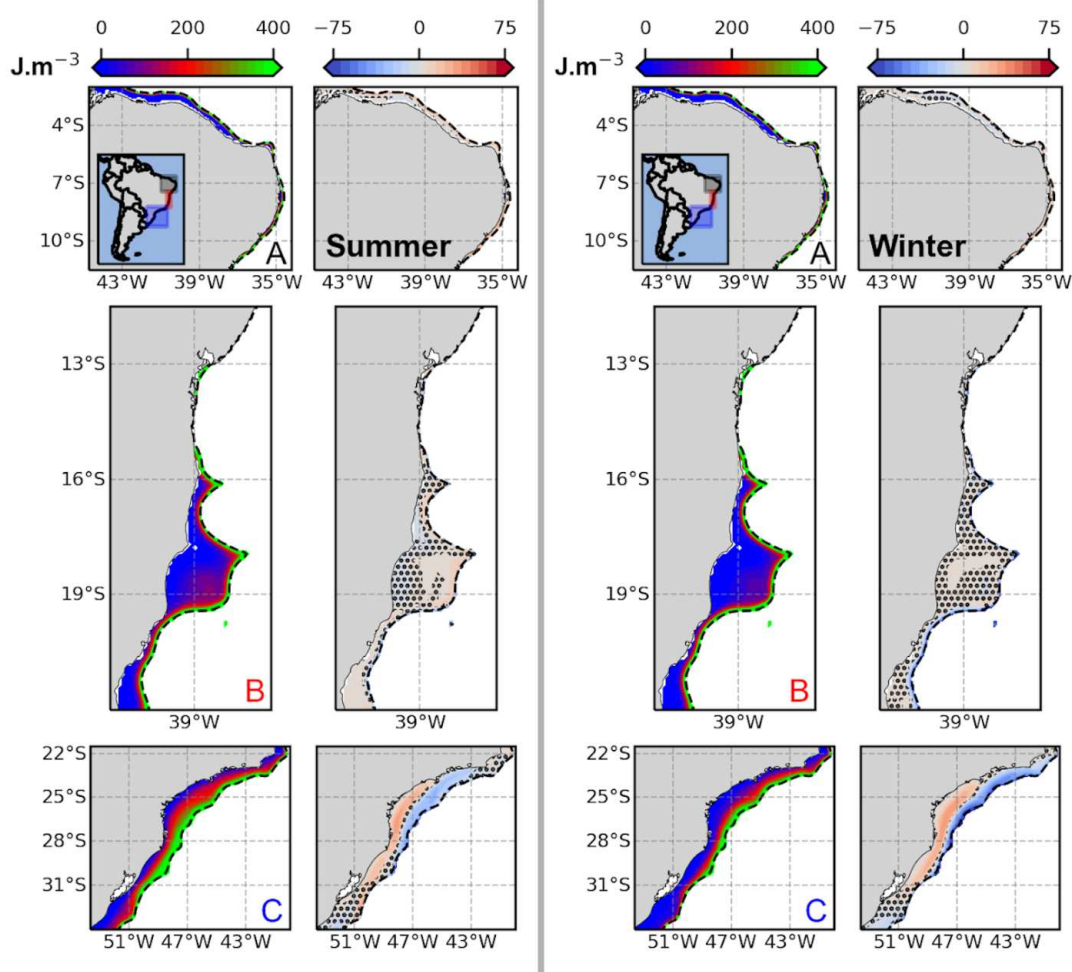


Figure 4.2: Historical climatology and change signal for the austral summer (left panel) and winter (right panel) of the potential energy anomaly (ϕ_{PE} in J.m^{-3}) across the Brazilian shelf. Summer is defined as the averages for December, January and February, whereas for Winter is June, July and August. Warm (positive) values indicate increased stratification, whereas cold (negative) values indicates a shift towards well-mixed conditions. The shelf is sectioned in three sectors to allow an easier visualization, and each lettered sector is color-referenced on the general South America inset in subset A. The dotted line represents the 200 m isobath and marks the shelf break.

domain, as well as explore the temporal evolution of the desired properties under anthropogenic forcing. For this reason, we define the SOM clusters using a combination of five properties: $\nabla \rho_{max}$, $\nabla \rho_{depth}$, ϕ_{PE} , sea surface temperature (SST) and sea surface salinity (SSS).

We tested different numbers of clusters, ranging from 4 to 10, and a sample of those results can be seen on Fig. 4.4. As shown in Figs. 4.2 and 4.3, the strongest impacts are found along south Brazil. The difference is such, however, that only by increasing the number of clusters above 7 does SOM start separating the impacts along the central and northern coastlines. Even with 10 clusters, both regions are essentially assigned a single cluster

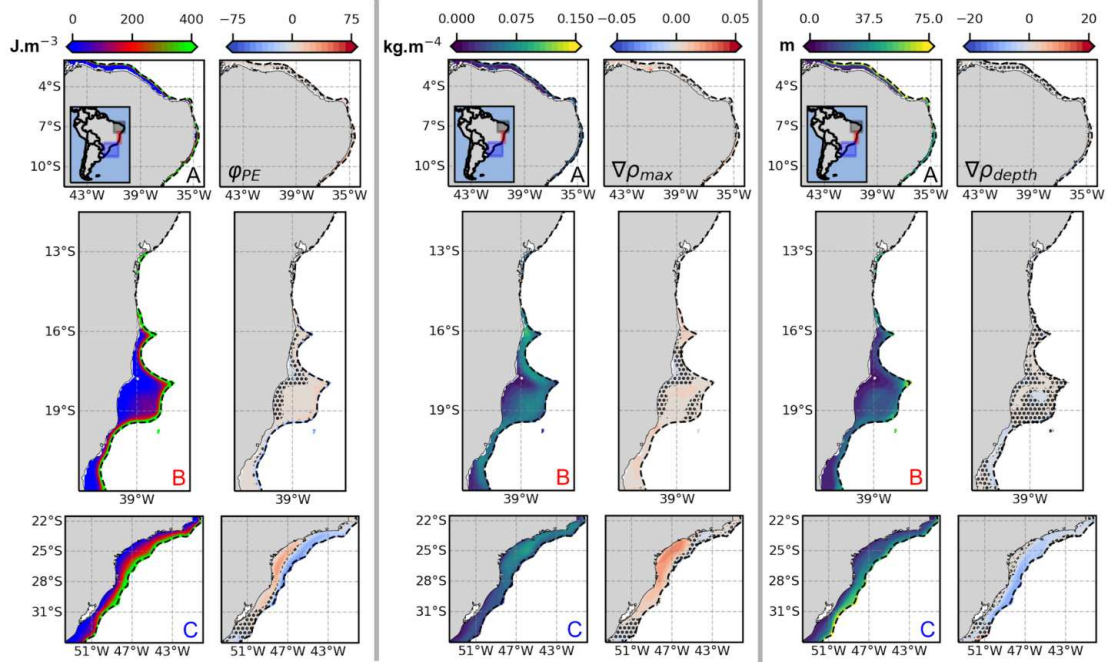


Figure 4.3: Historical climatology and change signal for the annual mean potential energy anomaly (ϕ_{PE} in J.m^{-3} , left panel) and the maximum pycnocline gradient ($\nabla\rho_{max}$ in kg.m^{-4} , central panel) and depth ($\nabla\rho_{depth}$ in m, right panel) across the Brazilian shelf. The shelf is sectioned in three sectors to allow an easier visualization, and each lettered sector is color-referenced on the general South America inset in subset A. The dotted line represents the 200 m isobath and marks the shelf break.

each, at most. In the south, on the other hand, a cluster below the Patos Lagoon and a cross-shelf gradient over the remainder shelf is preserved across all tests. As the number of clusters increase, this region is further refined zonally and over the shelf break, reflecting the susceptible nature of this region to anthropogenic climate change. Based on these results, we chose 6 clusters as an adequate representation of the different levels of anthropogenic impact over the Brazilian shelf. Although this choice is essentially subjective, it ensures clusters are not too small and t-test statistics between them reveals that only 2-3 and 4-6 are not significantly different from each other. The number of insignificant clusters increases in higher SOM configurations and even at 4 there was an insignificant pair (1-3).

Time series of the ϕ_{PE} for each cluster further illustrate the impacts on the vertical water column structure across the shelf (Fig. 4.5). For clusters 1, 5 and 6, ϕ_{PE} essentially oscillates around the historical average until the end of the 21st century, with roughly the same distribution between positive and negative trend phases (increase and reduction in stratification, respectively). These are the regions where changes in ϕ_{PE} were mostly insignificant across all time scales when we considered our control (Figs. 4.2 and 4.3). For the remainder clusters, however, anthropogenic impacts are clear. Clusters 2 and 3 show a

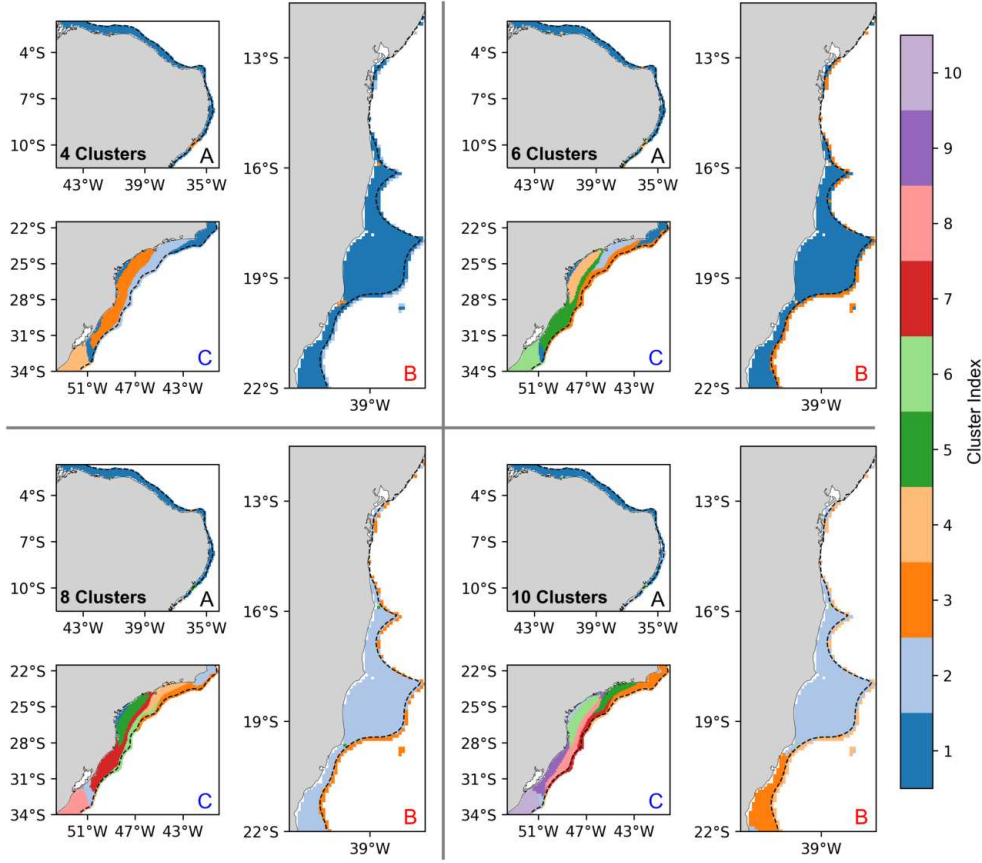


Figure 4.4: Cluster assignment using self-organizing maps (SOM) to model the change signal along the Brazilian shelf. Four test are shown, using 4, 6, 8 and 10 as the number of clusters to classify. The shelf is sectioned in three sectors to allow an easier visualization, and each lettered sector is color-referenced on the general South America inset in subset A (see Fig. 4.1). The dotted line represents the 200 m isobath and marks the shelf break.

clear negative trend for almost all climatologies. These accumulate during the second half of the 21st century and lead to the more well-mixed conditions seen around Cabo Frio's coastline and the outer shelf of the South Brazil Bight (Fig. 4.2). Cluster 4, on the other hand, shows the opposite behavior and accumulates mostly positive trends, leading to a more stratified water column at the inner region of the South Brazil Bight.

We can draw further insights on the shelf's water column response to increased GHG emissions by looking at the relative contribution of temperature ($\phi_{PE,T}$) and salinity ($\phi_{PE,S}$) to the ϕ_{PE} , which is done by calculating ϕ_{PE} based on their depth-averaged profiles at each cell and time step (Fig. 4.6). Overall, temperature tends to be the dominating factor to the ϕ_{PE} and increases in the order of 5 - 10% at the end of the century. The exception is cluster 6, where both temperature and salinity act as equal drivers to the ϕ_{PE} balance. Even in this region, however, we still see a shift in dominance after around 2050, with temperature overtaking salinity.

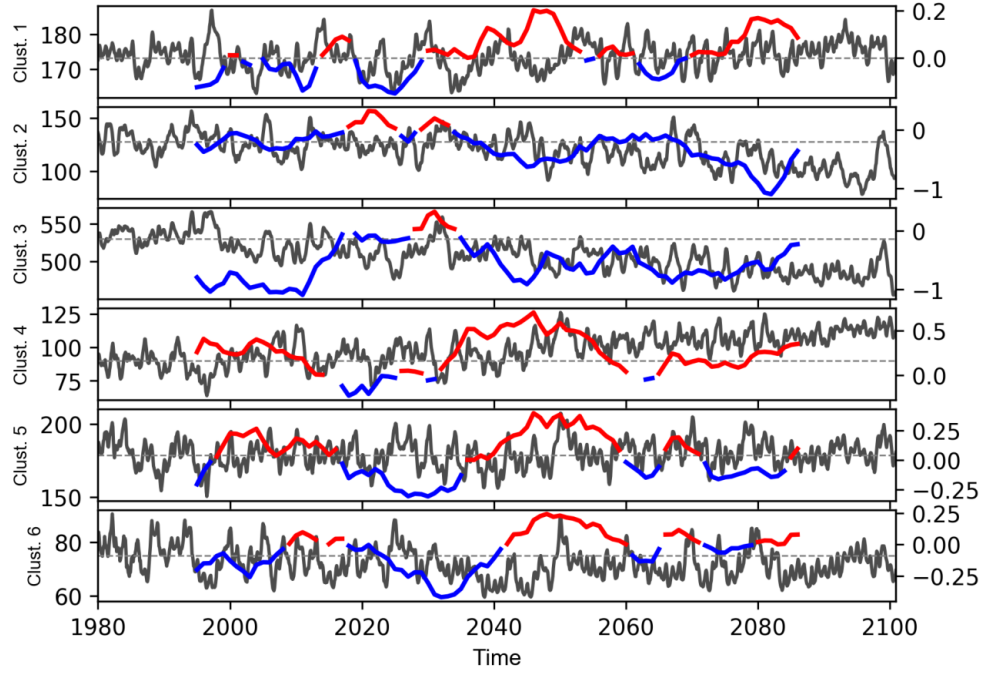


Figure 4.5: Left axis show the time series of the potential energy anomaly (ϕ_{PE} in J.m^{-3} , black line), whereas the right axis show the trend ($\text{J.m}^{-3}.\text{year}^{-1}$, colored line) for each defined cluster. The trend is estimated with a one-year running window for every 30-year climatology between 1980 and 2100, and referenced to the climatology's halfway year (e.g., 1994 for the period between 1980 and 2009). Red indicates higher stratification and blue indicates a shift towards more well-mixed conditions. Gaps are present where the trend is essentially zero. The dashed gray line represents the calculated historical average, considering the period between 1980 and 2009, and is related to the left axis.

Among these results, we can see that some portions within cluster 5 also showed an increase in ϕ_{PE} , specially around the southern shelf, but were grouped with regions where this impact was insignificant (Figs. 4.2 and 4.3). This led to the approximately neutral change seen in this cluster's ϕ_{PE} time series. This happens because different properties can dominate the separation between clusters (Fig. 4.7). Cluster 1, which represents the largest portion of the Brazilian shelf in length, shows essentially no impact on stratification (both ϕ_{PE} and pycnocline characteristics). SST increases on the order of 1°C , with a SSS increase of 0.5. Cluster 6, located south of the Patos Lagoon, shows a similar low impact on ϕ_{PE} but a slightly higher variance in pycnocline depth. It distinguish itself from other clusters mostly for the highest average salinity increase of ≈ 1 , alongside the highest SST variance. Cluster 4, located in the internal region of the South Brazil Bight, has the largest increase in pycnocline strength ($\nabla\rho_{max}$, $\pm 0.2 \text{ kg m}^{-4}$), a stronger increase in ϕ_{PE} and SST increase above 1°C . Clusters 2, 3 and 5 all show a tendency towards shallower pycnoclines and reduced ϕ_{PE} , while having similar small increases in SSS. However, cluster 2, located in the inner shelf near Cabo Frio, is also the only region to show an average SST decrease.

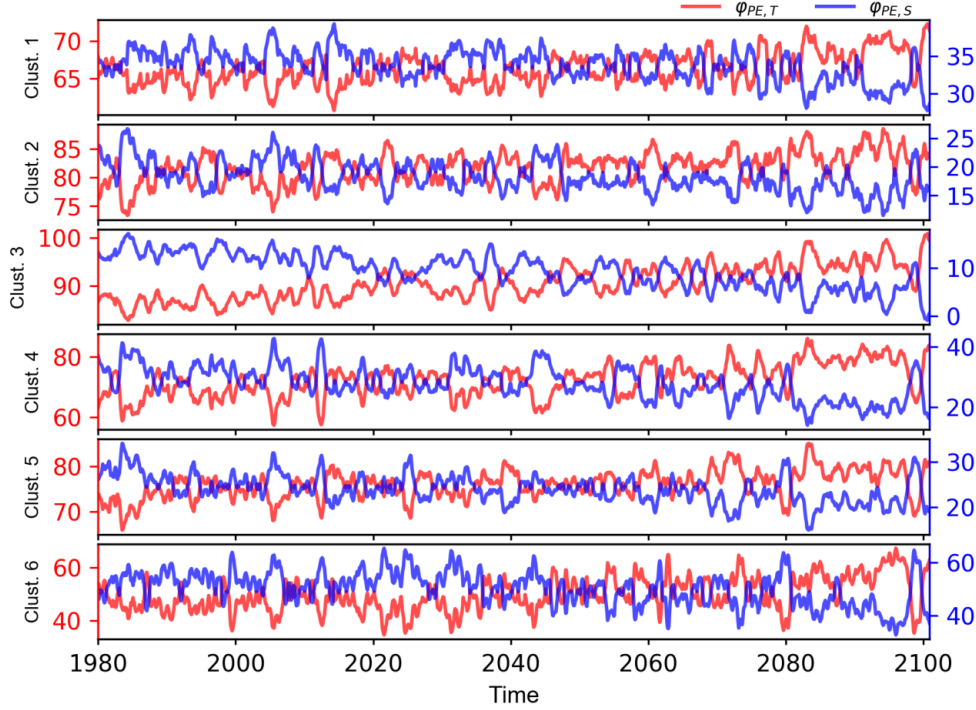


Figure 4.6: Time series of the relative contribution of temperature (red, left axis) and salinity (right, blue axis) to the potential energy anomaly (in %) for each defined cluster. We would like to draw the readers' attention to both axes' ranges.

This characteristic, in itself, distinguishes this cluster from number 3, even though they have insignificant t-test statistics between them when all properties are considered.

4.6 Discussion

4.6.1 Shelf's stratification response to a strong warming scenario

Over northern and northeastern Brazil, we mostly found very low ϕ_{PE} and essentially no evidence of a pycnocline ($\nabla\rho_{max}$, Fig. 4.3), even on a seasonal scale (Fig. 4.2). In this region, the water column is dominated by TW, forced shoreward by the constant downwelling pressure of the SE trade winds (Lentz, 1995; Soares and de Castro Filho, 1996). Even over the outer shelf and the shelf break, evidence of stratified conditions is only barely perceptible (Fig. 4.3). This could reflect the presence of the NBC, as Johns et al. (1998) found that up to 5 Sv of its volume can be transported through this region. Over the 21st century, however, there is no expectation of increased trade winds, only an expansion of the Hadley cells (Davis and Rosenlof, 2012; Hu et al., 2018). This could explain why the calculated change signal is mostly insignificant (Fig. 4.3). In this case, changes in ϕ_{PE} are a direct response to increasing surface temperature and salinity, which act to enhance and break down stratification (Atkinson and Blanton, 1986), respectively. Both impacts tend

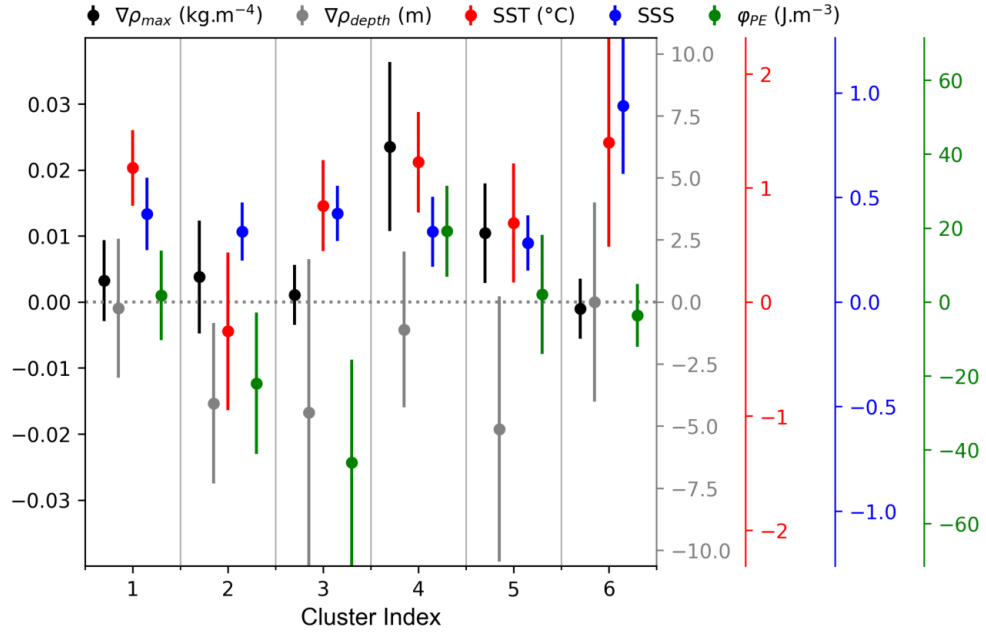


Figure 4.7: Mean and variance among model cells within each of the 6 clusters assigned by the SOM algorithm. Values are shown for the pycnocline strength and depth ($\nabla\rho_{max}$ in kg m^{-4} and $\nabla\rho_{depth}$ in m, respectively), sea surface temperature (SST in $^{\circ}\text{C}$), sea surface salinity (SSS) and potential energy anomaly (ϕ_{PE} in J m^{-3}).

to balance each other towards the end of the century (Fig. 4.7, cluster 1), even though some slight changes on the seasonal patterns can be expected (Fig. 4.2).

In contrast, we can see clear evidence of stratification over the central and south Brazilian shelves under recent past conditions (Figs. 4.2 and 4.3). As opposed to the northern coast, these locations are not under the influence of the trade winds, but rather of the upper branch of the South Atlantic Subtropical High (SASH), and are bound offshore by the BC (Stramma and England, 1999). The E and NE winds associated with the SASH creates upwelling-favorable conditions that push the SACW inshore year-round, with southerly wind anomalies occasionally disrupting this pattern during austral winter (Castro and Miranda, 1998). The SACW presence over the outer shelf was first identified by Campos et al. (1995) in the South Brazil Bight (between Cabo Frio and the Sta. Marta Cape), and linked to the water mass structure composing the BC (TW and SACW).

Along central Brazil, this stratification can be seen over the south bank of the Abrolhos Shelf and over the Tubarão Bight (Fig. 4.3), which both Pereira et al. (2005) and Palóczy et al. (2016) had previously identified as preferential SACW intrusion pathway. Although mostly wind-driven, Palóczy et al. (2016) showed that the presence of the BC uplifts the thermocline and leads to colder water contributions over the bottom boundary layer (up to -1.4°C), increasing the vertical temperature gradient and contributing to a higher ϕ_{PE} . Additionally, some austral summer and winter variability can be seen over the Abrolhos

shelf, but seasonal changes in stratification are much more important further south (Fig. 4.2).

We found that highly stratified conditions can reach up to the shoreline over the South Brazil Bight and the Southern Shelf during austral summer, affecting at least up to the mid-shelf (Fig. 4.2). [Castro \(2014\)](#) calculated the bulk stratification over the South Brazil Bight and found a clear cross-shelf gradient, with largest bulk stratification in the outer shelf. Seasonally, higher bulk stratification was found closer to the shoreline in austral summer when compared to austral winter, with the SACW signal around the 30 m and 70 m isobaths, respectively. The smallest variability was found in the outer shelf, with no clear seasonal fluctuations. This pattern of seasonal intrusion extends all the way to the Sta. Marta Cape ([Campos et al., 2013](#)) and beyond to the Southern Shelf. Although, over the Southern Shelf, it tends to be limited to the shelf break during austral winter (Fig. 4.2). This happens mostly because this region is also dominated by the periodic seasonal excursion of the Plata River Plume (bringing PW), which dominates the vertical structure of the inner-to-mid shelves during winter promoting weakly stratified conditions, and retreats to around 32°S during summer ([Piola et al., 2000](#); [Möller et al., 2008](#); [Palma et al., 2008](#)).

Nevertheless, even though the stratification over these regions seems to be essentially controlled by the SACW intrusions, their response to anthropogenic climate change is distinct. Over the central shelf, there is an overall increase in stratification (both ϕ_{PE} and pycnocline strength), accompanied by a shallower pycnocline position (Fig. 4.3). The same can be found over the mid-to-inner shelf regions of the South Brazil Bight (except around Cabo Frio) and the Southern Shelf (Fig. 4.3), with a clear seasonal pattern (Fig. 4.2). Over the mid-to-outer shelf and around Cabo Frio specifically, a reduction in ϕ_{PE} and a stronger shoaling of the pycnocline points towards an increased volume of SACW, in agreement with the findings of [de Souza et al. \(2020\)](#). In essence, the ϕ_{PE} increase in the mid-to-inner shelf reflects the further on-shelf migration of SACW combined with the increased surface warming. The ϕ_{PE} decrease in the outer shelf, however, is dominated by the pycnocline shoaling, as a higher vertical proportion of the water column reflects SACW characteristics and compensates the surface warming. In the latter case, the pycnocline is vertically squeezed closer to the surface, increasing its gradient. A similar mechanism was found to develop in the North Sea in response to storm passages ([Gronholz et al., 2017](#)).

On the synoptic scale, these overall changes in stratification are connected to the south-westward migration of the SASH ([Ryckaczewski et al., 2015](#)), in response to the poleward migration of the westerlies ([Barnes and Polvani, 2013](#)). [de Souza et al. \(2020\)](#) showed how wind speeds associated with the SASH could increase by $\approx 2 \text{ m s}^{-1}$ along the Brazilian coastline, leading to a stronger Ekman offshore forcing and a larger spread of the SACW over the bottom boundary layer of the South Brazil Bight. They also showed, however, that

this does not necessarily induce an increased fertilization of the surface waters, as vertical velocities at the bottom of the mixed-layer decrease. In this case, the higher momentum input by the enhanced wind field does not produce enough kinetic energy to overcome the stronger pycnocline, even though the water column is characterized by a decrease in ϕ_{PE} . Albeit these results reflect the impact of RCP8.5 conditions, [Sydeman et al. \(2014\)](#) showed similar trends in data sets covering the recent past, providing further confidence in the changes presented here.

An important consequence of a stronger pycnocline is that it can lead to reduced supply of O_2 to deeper layers of the water column, and even to anoxic events ([Keeling et al., 2010](#)). As an example, hypoxia is expected for the Gulf of Mexico under increased GHG emissions ([Laurent et al., 2018](#)). For the Brazilian shelf, the consequences to the ecosystem balance remains unclear, as our simulations did not involve a biogeochemical model, but increased stratification could disrupt food chains over the shelf. [Resgalla Jr et al. \(2001\)](#), for example, showed how the presence of SACW over the Southern Shelf was correlated to high zooplankton biomass, specially of species typically found in upwelling zones. Understanding the ecological impact is especially important in the South Brazil Bight and the Southern Shelf, which are natural fisheries hot spots and have large economical importance on a national level ([Castro et al., 2006](#); [Piola et al., 2018](#)).

4.6.2 Understanding the regional segmentation

Once the physical processes over the Brazilian shelf have been explored, we can try to gather further understanding on the leading mechanisms that drive the cluster assignments provided by SOM (Fig. 4.4) and their response to anthropogenic climate change. Unless specified, cluster numbers refer to the regions defined for 6 clusters (see section 4.5.2). Cluster 1 comprises both the central shelf and the northern/northeastern Brazilian shelves, which are under the effect of different synoptic wind systems. Nevertheless, they are grouped together or divided at most in two clusters for all SOM grid configurations. Even when separated in two regions (e.g., for 8 clusters), the two groupings are not statistically different from each other, based on a t-test considering all model cells within each group. This indicates that, at the long-term scale, the slightly increased water column stabilization over the northern shelf mostly reflects the increase in surface warming. The exception is when 10 clusters are considered. In this case, a third cluster is defined around the Tubarão Bight until Cabo Frio, spanning the whole shelf (Fig. 4.4, bottom right). This is a reflection of the stronger influence of the SACW upwelling over this region ([Palóczy et al., 2016](#)). The already ubiquitous presence of SACW, however, also means that the enhanced wind field ([de Souza et al., 2020](#)) does not produce an impact as strong as what can be seen in south Brazil, limiting the long-term impacts on stratification in this region (Fig. 4.3).

Cluster 3 defines the shelf break region below 13°S and represents the influence of the BC, veering slightly onshore over the outer shelf in the South Brazil Bight. It is characterized by the strongest changes to the ϕ_{PE} and a large variance on the pycnocline depth (Fig. 4.7). These changes reflect the stronger shoaling of the pycnocline and indicate an uplifted SACW within the BC. This can be seen when we consider the relative contribution of temperature and salinity to ϕ_{PE} (Fig. 4.6), with temperature contributing almost 100% at the end of the century as the thermal gradient between TW and SACW increases along the pycnocline. When the number of clusters is increased (e.g., 8 clusters), this region is refined into two segments separated at $\approx 25^\circ\text{S}$. Between those two segments, the only significant difference is in the pycnocline depth (not shown), with a deeper pycnocline below this latitude. [de Souza et al. \(2020\)](#) showed that, at 25°S, there was a change in the local transport of the BC, with a slight increase to the north and a slight reduction to the south of this latitude, respectively. Coupled with a higher mesoscale activity associated with the BC around the northern portion ([Oliveira et al., 2009](#)), these processes could lead to a shallower pycnocline, thus causing the separation seen here.

Clusters 2 and 4, located in the inner-to-mid shelf region of the South Brazil Bight, are perhaps the most stable in terms of position and shape between all clusters. Cluster 2 is the only location where an overall SST decrease is found (Fig. 4.7). In this region, located between Cabo Frio and Ubatuba, SACW is present year-round ([Castelao and Barth, 2006](#)) and reflects the combined effects of the Ekman upwelling ([Castro and Miranda, 1998](#)) and a shelf break upwelling ([Campos et al., 2000](#)), the latter of which is advectively-accelerated onshore due to the narrowing of the shelf's width around Cabo Frio when the shelf break orientation turns E-W ([Palma and Matano, 2009](#)). Its shape, which produces a surface cold tongue visible on satellite imagery ([Castelao et al., 2004](#)), reflects the SW advection of SACW and is considered one of two preferential pathways for its intrusion over the South Brazil Bight ([Cerdeira and Castro, 2014](#)). [de Souza et al. \(2020\)](#) showed how the decrease in SST over this region at the end of the century is a consequence of increased upwelling at the shelf break, due to a local adjustment of the BC flow to the southward migration of the SASH. This also explains the decreased ϕ_{PE} , as a higher proportion of SACW dominates the water column's vertical structure, and the small changes to the pycnocline, as the region is already dominated by the dynamics of the SACW intrusions. In turn, cluster 4 shows the strongest stratification increase among all clusters (Fig. 4.7). In this region, SACW is normally only found during summer and retreats closer to the outer shelf during winter ([Palma and Matano, 2009](#); [Brandini et al., 2014](#); [Castro, 2014](#)). However, under increased Ekman forcing due to the strong warming scenario, the bottom intrusion of SACW travels further onshore and affects the region within this cluster even during winter ([de Souza et al., 2020](#)). In essence, the effects in cluster 4 reflect the increased bottom influence of SACW over a larger portion of the South Brazil Bight.

Finally, clusters 5 and 6 are found mostly over the Southern Shelf. In this region, SACW intrusion is limited to the mid-to-outer shelf in present conditions (Fig. 4.2), and the constant presence of the PW further complicates the interaction between water masses. Cluster 5's dominant characteristic is a stronger pycnocline shoaling, although with a large variance (Fig. 4.7). This points towards a stronger influence of the on-shelf SACW intrusions in the future, similar to the effects found for cluster 3. This is specially important during winter (Fig. 4.2) when this process would normally be limited to the outer shelf (Piola et al., 2008). When increasing the number of clusters above 9, this region is further segmented into two cross-shelf clusters (Fig. 4.4). While the inshore cluster likely reflects the northward excursion of the Plata River plume (Piola et al., 2000; Möller et al., 2008), the offshore cluster likely reflects the southward transport of STSW and the development of the inverted thermocline (Castello and Möller Jr., 1977), where temperature can increase with depth due to enhanced vertical stratification. In both cases, however, the STSW is the transported water mass, and likely explains why the separation between these two clusters is not statistically-significant and the anthropogenic impact is homogeneous along the whole shelf.

Cluster 6, similar to clusters 2 and 4, also presents a rather stable position. Its northern limit, around 32°S, marks the approximate location of the subtropical shelf front. This front separates the influences of the STSW and the subantarctic shelf water, normally associated with colder waters from the Malvinas Current (Piola et al., 2000). This position also marks an important transition in regards to the Plata River plume dynamics. During winter, the plume is pushed northward due to atmospheric cold fronts and can advance up to the South Brazil Bight as a shallow coastal plume. During summer, on the other hand, the constant NE winds trap the plume southward of this front, extending the plume throughout the whole shelf and dominating the water column (Piola et al., 2000, 2008; Möller et al., 2008). This indicates that this cluster captures the region of constant influence from the Plata River plume and explains the strongest SSS and SST variability found herein (Fig. 4.7), as its dynamics is strongly modulated by the seasonally reversing winds (Piola et al., 2005; Palma et al., 2008). It also explains why anthropogenic climate impact over this area is mostly insignificant when we consider our control variability (Figs. 4.2 and 4.3), as we see no significant changes to the Plata River discharge at the end of the century (de Souza et al., 2020). Notwithstanding, this is the only cluster where temperature and salinity contributed approximately equally to the overall ϕ_{PE} (Fig. 4.6). Piola et al. (2008) identified that temperature controlled the stratification over this region during summer, but salinity was the dominant forcing during winter. Although our ratio of T/S influence in summer suggests a more equal contribution of both properties (0.96), the winter ratio shows a clear salinity driven stratification (0.83). In the end of the century this no longer holds true, and both summer and winter ratios shows the higher importance of temperature in driving

stratification, with ratios of 1.27 and 1.12, respectively. This highlights that even though no clear anthropogenic impact might be apparent, changes in the balance between forcing mechanisms can be significant.

Based on these analyses, the South Brazil Bight stands out as the region along the Brazilian coastline most susceptible to climate-induced changes in stratification, as it is influenced by physical drivers modulating the onshore intrusion of SACW and the northward penetration of PW. Although, its changes respond mostly to modifications in the SACW intrusion. This is reflected in SOM through the largest number of cluster assignments within this region, combined with a more refined cross-shelf segmentation. While arguments to increase the number of clusters to further segment other regions of the shelf can be made, they mostly create insignificant separations (e.g. northern and central shelves or cross-shelf segmentation in the Southern Shelf). Nevertheless, it is important to recognize that all generated regions have strong underlining support in dynamical characteristics, even when we only consider the net change signal for their modeling.

4.7 Conclusions

Our results indicate that changes in stratification due to anthropogenic climate change will have a greater effect in the south and southeastern sections of the Brazilian shelf, in comparison to the north(eastern) and central sections of the coast. The stronger changes in stratification are mostly driven by a more effective bottom intrusion of SACW, specially evident as it uplifts the pycnocline. In the far south (around the Patos Lagoon), the balance between temperature and salinity in driving the ϕ_{PE} will shift, with temperature dominating the stratification even during austral winter. This result is specially important when we consider that the net change signal in this region is mostly indistinguishable from natural variability, indicating that modifications of individual driving mechanisms can happen even if no climate change impact is apparent.

Over the inner to mid shelf sectors of the South Brazil Bight and the Southern Shelf, stratification will increase due the spread of SACW over a larger portion of the shelf and the increased surface warming. In the outer shelf and the shelf break, on the other hand, the currently ubiquitous presence of SACW leads to an overall decrease in ϕ_{PE} , as its influence further grows in the water column towards the end of the century. Nevertheless, this same process lifts and squeezes the pycnocline, increasing its strength and potentially limits nutrient fluxes towards the mixed-layer. Dynamically, the strongest impacted region is found within the South Brazil Bight, between Ubatuba and the Sta. Marta Cape, but a more detailed assessment of biogeochemical fluxes would require information from an ecosystem model.

Shelf regions in northern and central Brazil, in contrast, are projected to experience only a small increase in stratification, mostly associated with the increased surface warming. Increase in stratification over this region is also weaker than the projected impact over southeastern Brazil, although ESMs tend to estimate a stronger impact over the tropical Atlantic. This highlights the importance of regional processes (i.e., the SACW intrusion in our study site) in mediating the response of local shelf seas to increased GHG emissions.

Chapter 5

Overall Assessment & Concluding Remarks

In this chapter, we review the major findings explored in each manuscript, how they relate to each other and how they help us advance our understanding of the projected impacts of anthropogenic climate change to the physical conditions along the Brazilian shelf. Section 5.1 explores the model performance in reproducing the recent past at the basin-wide scale and the most relevant regional ocean processes in Brazil's shelf waters. It also discusses the shelf break upwelling at the South Brazil Bight and its driving mechanism. This is particularly relevant for understanding the decrease in sea surface temperature found in this region at the end of the 21st century, which is further explored in section 5.2. Specifically, section 5.2 analyses how the changes affecting the Brazil-Malvinas confluence are connected to the changes in the upwelling regime at the South Brazil Bight and in water column stratification along Brazil's shelf. Ultimately, the forecast impacts associated with anthropogenic climate change are put into perspective, considering the expected modifications in the atmosphere and to the South Atlantic more broadly. Finally, we evaluate the shortcomings in our model and how they relate to some of the biases found in our results in section 5.3, and suggest improvements to the modeling framework that could expand the analysis performed here and provide a more complete understanding of the effects of increased greenhouse gas emissions to the Brazilian shelf waters.

5.1 Model evaluation and historical performance

Overall, ensemble variability was small for our five RCP8.5 simulations and the correlation between ensemble members for different properties was consistently high (above 0.90) when evaluated in locations within the Brazilian shelf (see section 3.4.1). In this case, a median profile based on the five ensemble members proved to be a good representative of the general model behavior, capturing the dominating frequency ranges within all evaluated time series. This reflects the stronger influence of the external forcing induced by the boundary conditions in comparison to the internal variability of our high-resolution domain on the model spread, which was also shown by Mathis et al. (2018) for the Northwest European shelf. To further test HAMSOM's performance during the recent past, we evaluated its behavior with respect to temperature, salinity and general circulation, over the South Atlantic and within the Brazilian shelf.

Temperature We had a correlation coefficient higher than 0.98 for all seasons (averaged over 1985 to 2016) when compared to the WOCE/Argo Global Hydrographic Climatology (Gouretski, 2018) for the same period, with the model reproducing some important features of the basin wide circulation and regional processes along the Brazilian shelf. In the tropics, the appearance of an equatorial cold tongue during austral winter (Fig. 2.2) and the shallower equatorial mixed layer (Fig. 2.3) showcases the effect of the equatorial upwelling (Wan et al., 2011), whereas the predominance of well-mixed conditions year-round

over the Brazilian shelf (Fig. 4.2) highlights the effectiveness of the SE trade winds in controlling the water column stratification (Lentz, 1995; Soares and de Castro Filho, 1996). In the subtropics, we can see the northward intrusion of cold sub-antarctic water along the shelf during austral winter (Fig. 2.2), previously reported by Campos et al. (1999a), as well as the colder sea surface temperature anomalies during austral summer along the Cabo Frio coastline (Fig. 3.5), which reflects the influence of a coastal upwelling (Campos et al., 2000).

This coastal upwelling, in particular, reflects two different regimes and brings colder South Atlantic Central Water within the shelf (Campos et al., 2000; Palma and Matano, 2009). The first is driven by the NE winds associated with the South Atlantic Subtropical High, and is most effective during austral summer (Lima et al., 1996; Castro and Miranda, 1998; Castelao et al., 2004). At the central shelf, it affects both the south bank of the Abrolhos shelf and the Tubarão Bight (Fig. 4.2), being important mechanisms for the water column stratification (Pereira et al., 2005; Palóczy et al., 2016). These cold water intrusions are constantly present at the outer shelf (Castro, 2014), being able to reach all the way up to the coastline during austral summer in some section of the South Brazil Bight and near the Santa Marta Cape (Campos et al., 2000; Möller et al., 2008; Campos et al., 2013). This seasonal variability pattern is well captured within our HAMSOM domain (Figs. 3.4 and 4.2) and are important mechanisms for the fertilization of the subtropical Brazilian shelf waters (Castro et al., 2006).

The second upwelling regime is controlled by the interaction of the Brazil Current with the shelf break topography and is seen within the South Brazil Bight (Campos et al., 1995). The process behind this interaction, however, has been explained using different mechanisms. Campos et al. (2000) and Silveira et al. (2000) hypothesized that this upwelling is driven by a southwestward moving Rossby wave, triggered because of barotropic instabilities along the Brazil Current as it overshoots the latitude of Cabo Frio. In this case, this Rossby wave would be a consequence of potential vorticity conservation in response to the coastline geometry shift from NE-SW to E-W around Cabo Frio. Palma and Matano (2009), on the other hand, hypothesized that it is the change in the along pressure gradient around Cabo Frio that forces an enhanced bottom intrusion around Cabo Frio, advectively accelerating the flow from the Brazil Current inshore.

Our results, however, suggest a combination of both processes (see section 3.5.1). Based on the same potential vorticity conservation arguments from Campos et al. (2000) and Silveira et al. (2000), we believe that the Brazil Current produces dipole structures with upwelling and downwelling cores as it flows around and interacts with the shelf break's ridge topography (Figs. 3.4 and 3.8), following the theoretical mechanism described by Song and Chao (2004). This would not require the geometry shift found in Cabo Frio,

only the presence of these large scale ridges that can be seen along the topography (Fig. 3.1). This is supported by the results from [Palma and Matano \(2009\)](#). In their simulations, the smoothing of bathymetric contours removes the ridges seen along the shelf break and limits the upwelling to the Cabo Frio region, where the geometry shift is still preserved (essentially a large ridge). This discourages the Rossby wave explanation from [Silveira et al. \(2000\)](#), as it should still happen under [Palma and Matano \(2009\)](#) configuration downstream of Cabo Frio, but it does not. Additionally, we found the same acceleration found by [Palma and Matano \(2009\)](#), which enhances the upwelling process in the northern sector of the South Brazil Bight and explains why the upwelling is much more effective along this section of the coast, as demonstrated by [Castelao and Barth \(2006\)](#).

Salinity An evaluation of salinity against the same dataset yielded correlations above 0.77 for all seasons, with HAMSOM showing a fresher surface ocean, particularly over the tropics. This is expected, as the MPI-ESM model shows a positive precipitation bias over the tropical Atlantic with a similar fresher upper ocean ([Jungclauss et al., 2006, 2013](#)), which our bias correction do not manage to fully eliminate as it relates to an incorrect representation of the ITCZ dynamics over the tropics from the global model. Nevertheless, the maximum salinity core is well represented within the South Atlantic Subtropical High, as well as the plume effects associated with the Amazon and the La Plata rivers (Fig. 2.4). Regionally, the dominant effect of the Plata River Plume over the southern Brazilian shelf (Figs. 4.6 and 4.7, cluster 6) and its northward migration towards the South Brazil Bight (Figs. 2.4 and 3.7) during austral winter are both captured within our HAMSOM domain, being important drivers of the local circulation ([Castro et al., 2006; Piola et al., 2018](#)).

Circulation Mean and eddy kinetic energy calculated based on the horizontal zonal and meridional velocities obtained from HAMSOM were compared to data from the Global Drifters Program following the methodology of [Oliveira et al. \(2009\)](#). For the main circulation, represented by the mean kinetic energy, model performance was fair with a correlation coefficient of 0.58 (Fig. 2.6). Our estimated Malvinas Current strength at 45°S (35.8 ± 8.2 Sv) is similar to the estimate obtained by [Spadone and Provost \(2009\)](#), while our Brazil Current strength at 29°S is within one standard-deviation of estimates found within [Gabioux et al. \(2013\)](#) but indicates a stronger flow, with both currents exhibiting a correct seasonal variation (Fig. 2.7).

In this case, we believe the overestimation of the Brazil Current is a reflection of the poor resolution of turbulent flows within the Brazil-Malvinas Confluence, as the Zapiola Anticyclone is not properly reproduced (Fig. 2.6) and some of the main flow's energy is not dissipated before continuing along the gyre circulation. This is because the representation of the Zapiola Anticyclone is sensitive to the correct interaction between the Malvinas Current and the bottom topography ([de Miranda et al., 1999; Combes and Matano, 2014a](#)),

which is likely underestimated in our simulations due to the coarse vertical discretization at the deep ocean. Nevertheless, the mean position of the Brazil-Malvinas Confluence as well as its seasonal variability is well reproduced (Fig. 2.7), and its poleward migration within the recent past is in agreement with the estimates from previous authors (Goni et al., 2011; Lumpkin and Garzoli, 2011; Combes and Matano, 2014b).

5.2 Forecasting anthropogenic climate impacts

We investigated future impacts of anthropogenic climate change on the Brazilian shelf by looking at processes affecting the region from large (Brazil-Malvinas Confluence) to local scales (stratification and upwelling), under a strong warming scenario (RCP8.5). In a more general sense, all the modifications expected to affect the Brazilian coastline at the end of the 21st century reflect the adjustment of the coastal dynamics to the poleward migration of the South Atlantic Subtropical High (Fig. 3.9), identified by Rykaczewski et al. (2015), and the widening of the Hadley cell over the tropics (Kang and Lu, 2012; Davis and Rosenlof, 2012; Hu et al., 2018). This exposes the Brazilian coast to mildly increased wind speeds, around 2 m s^{-1} (Fig. 3.9), and is in agreement with global climate change forecasts indicating no significant change to the gyre's intensity (Reboita et al., 2019), and with historical reanalysis already suggesting similar poleward shifts during the recent past (Sydeman et al., 2014; Gilliland and Keim, 2018).

In essence, this migration of the subtropical gyre is also connected to the poleward migration of the westerlies (Swart and Fyfe, 2012; Wilcox et al., 2012; Barnes and Polvani, 2013), which strengthens the Southern Ocean atmospheric circulation (Fig. 2.9). As a consequence, the Antarctic Circumpolar Current's main flow shifts closer to Antarctica (see section 2.5.2), weakening the Malvinas Current by $\approx 25\%$ (Figs. 2.8 and 2.10). As no equivalent weakening is seen along the Brazil Current, the main position of the Brazil-Malvinas Confluence continuously shifts poleward at a rate of -0.44° per decade (Fig. 2.8), in response to the new dynamical equilibrium between the two western boundary currents.

Our results suggests that these shifts in the main pathway of the Antarctic Circumpolar Current occurs periodically even during the recent past and are directly connected to the intensity of the Malvinas Current (Fig. 2.10). However, only under increased anthropogenic forcing does it lead to a continued migration of the mean confluence position throughout the 21st century. This has implications to the confluence's seasonal variability as well, decreasing its amplitude by approximately half of its historical range and reaching its maximum northward extension earlier in the year (June, as opposed to July/August). These results corroborate previous findings from Combes and Matano (2014b) and Pontes et al. (2014) to the pivotal role of the Malvinas Current in controlling the Brazil-Malvinas Confluence poleward migration, and explain the connection to the Antarctic Circumpolar

Current even when no apparent changes to its transport can be verified.

Aside from impacts to the confluence dynamics and variability, the projected increase in temperature and salinity over this region (IPCC, 2013) is also likely to indirectly affect the Brazilian coastline. As the zone of formation of the South Atlantic Central Water (Gordon, 1981; Sprintall and Tomczak, 1993), these changes in surface properties will modify the water mass' physical characteristics within the Brazil Current (Fig. 3.2) and, by extension, the Brazilian shelf. This is because the South Atlantic Central Water is an important component of the water column stratification and fertilization along subtropical Brazil (Castro et al., 2006). The other component is the freshwater plume associated with the Plata River (Piola et al., 2000, 2018), south of Brazil, but we found no significant changes to its discharge within our simulations (see section 3.5.2).

In this light, changes modifying the intrusion of South Atlantic Central Water along the Brazilian shelf have a central role in defining the coastal response to anthropogenic climate change. The stronger winds along Brazil's coast due to the southwestward migration of the South Atlantic Subtropical High (Fig. 3.9) enhances the offshore Ekman transport over the shelf (Fig. 3.10) and pushes this cold water intrusion further onshore through the shelf's bottom (Fig. 3.6), exemplified in our results over the South Brazil Bight. A similar process is expected to happen in the Californian Upwelling System (Snyder et al., 2003), along the Iberian Peninsula (Miranda et al., 2013) and the Canary Upwelling System (Sousa et al., 2017), under increased greenhouse gases emissions.

Contrary to expectations, however, it does not lead to higher vertical velocities at the mixed layer (Fig. 3.4), as the enhanced kinetic energy provided by the wind field is not enough to overcome the increased water column stability, reducing the available potential energy to be converted into vertical motion (Fig. 3.11, process described in Urakawa and Hasumi, 2009). This, in turn, is a consequence of the stronger pycnocline that develops over the shelf at the end of the century due to the surface heating (Fig. 4.6). Additionally, the increased bottom intrusion of colder South Atlantic Central Water squeezes the pycnocline towards the surface as its relative fraction in the water column increases, shoaling the pycnocline and further enhancing its strength (Figs. 4.2 and 4.3). In contrast, over the tropics, the water column is dominated by the warm Tropical Water, with the constant pressure of the SE trade winds inhibiting bottom intrusions of the South Atlantic Coastal Water (Lentz, 1995; Soares and de Castro Filho, 1996) and the formation of a pycnocline. This setting does not change in our future scenarios, leading to only slightly increased stratification in northern Brazil (Figs. 4.2 and 4.3) due to the increased surface heating (Fig. 4.6).

Changes in sea surface temperature and salinity across the Brazilian shelf are perhaps the most clear examples of the regional response to anthropogenic climate change. The

IPCC (2013) predicts an increase in sea surface temperature between 2 °C and 3 °C and of up to 0.5 in sea surface salinity along the South America coastline for the RCP8.5 scenario. For the sea surface temperature, our results indicate increases mostly below 2 °C across the whole shelf, with stronger temperature increases where the upwelling mechanism is limited or non-existent (Fig. 4.7, clusters 1, 3 and 6). In the northern sector of the South Brazil Bight we even found a decrease in sea surface temperature at the end of the 21st century of up to 1 °C (Fig. 3.5 and cluster 2 in Fig. 4.7). In this region, the combination of both the Ekman and shelf break upwelling mechanisms (see section 3.5.1) boost the presence of the South Atlantic Central Water, overtaking the heating effects from the increased surface warming. For the sea surface salinity, our results are more inline with the global projections and indicate a slightly reduced impact to this property, with an upper bound at 0.5 (Fig. 4.7). The exception is in the very south of Brazil, close to the Patos Lagoon (Fig. 4.7, cluster 6). In this region, dominated by the Plata River plume dynamics (Piola et al., 2000; Möller et al., 2008; Palma et al., 2008), a strong increase in sea surface salinity (up to 1) suggests a saltier Plata River Plume due to the increased evaporation over the SW South Atlantic (IPCC, 2013), although we did not explicitly analyze this water mass characteristics within our simulations.

Based on our results, the subtropical Brazilian shelf is more susceptible to climate change when compared to the tropical region, specially the South Brazil Bight where the continental shelf is wider and more influenced by variations of the upwelling mechanism (Fig. 4.4 and sections 3.5.1 and 4.6.2). This goes against global projections regarding changes in ocean stratification, which project a stronger impact over the tropics (Capotondi et al., 2012; Fu et al., 2016). The weakening of vertical flows at the mixed layer also evidence a distinct response the large scale dynamics, as Earth System Models predict an overall intensification of the Eastern Boundary Upwelling Systems (Wang et al., 2015). This highlights the heterogeneity in the response of anthropogenic climate change in shelf waters and the importance of considering regional processes when evaluating local responses, as has been likewise demonstrated for other regions (e.g., Holt et al., 2010; Wang et al., 2010; Praveen et al., 2016; Holt et al., 2018; Mathis and Mikolajewicz, 2020).

Ultimately, our results indicate that the dominant regional process shaping the future conditions across the Brazilian shelf is the upwelling of South Atlantic Central Water and how it will respond to shifts in the atmospheric circulation over the South Atlantic Ocean. Nevertheless, even regions where no net change signal was identified can still undergo significant change in its governing processes. We found this to be the case in the southernmost section of the Brazilian shelf, around the Patos Lagoon (Fig. 4.4, cluster 6). Even though changes in stratification in this region were insignificant when we accounted for the natural variability (4.3), the physical property driving its stratification shifted at the end of the century (4.6). In the recent past, stratification is driven by salinity during austral winter

and temperature during austral summer (Piola et al., 2008), but temperature dominates the reaction of the water column's vertical structure across all seasons in the future scenario. This result further underscores the importance of evaluating anthropogenic climate change on a regional scale.

5.3 Outlook and recommendations

As it stands, our model framework is able to reproduce both large scale features of the South Atlantic circulation and the main physical drivers controlling the stratification and dynamics within the Brazilian shelf. Nevertheless, a few improvements are suggested, targeting specific weaknesses. First, if the focus is on better resolving the Brazil Current flow, properly replicating the Zapiola Anticyclone is likely to increase the overall model performance. It would require a significant upgrade in the model vertical discretization, however, as this feature is sensitive to the interaction between the Malvinas Current and the bottom topography (de Miranda et al., 1999; Combes and Matano, 2014a). This would come with a clear increase in computational and data storage/processing cost.

On the other hand, if the goal is to better resolve and understand the shelf dynamics, other modifications might be more appropriate. If the goal is to study the response of precipitation over Brazil, a coupled ocean-atmosphere simulation with a higher resolution atmospheric regional model would be necessary to more adequately resolve ocean-atmosphere coupled variability modes. Nobre et al. (2012a) showed how a coupled simulation was necessary to properly represent the feedback between sea surface temperature and the South Atlantic Convergence Zone in southeast Brazil. Meanwhile, Marengo et al. (2012) analyzed future scenarios (SRES A1B) and found a decrease in precipitation in the Amazonas, São Francisco and Paraná river basins, partly connecting this reduction to a weakening of the South Atlantic Convergence Zone. In the northeast, heavy rainfall episodes have also been correlated to positive sea surface temperature anomalies just off the coast (Kouadio et al., 2012; Hounsou-Gbo et al., 2016). Aside from the impacts on precipitation, stand to reason that these variability modes also affect the near-shore atmospheric circulation, which is an essential component to understanding changes to extreme sea level events along the Brazilian coastline. In this case, regionally resolving the atmosphere would enable a more realistic representation of coastal circulation and the near-shore processes.

Additionally, the increase in stratification and the stronger pycnocline verified in our results should limit the nutrient flux between the mixed layer and the deeper shelf waters (Fu et al., 2016), as well as increase the risk of oxygen depletion at depth (Keeling et al., 2010; Laurent et al., 2018). However, the increased bottom intrusion of South Atlantic Central Water could lead to increased primary production. This water mass has been consistently connected to the fertilization of the shelf waters (Castro et al., 2006; Piola et al.,

2018; Bordin et al., 2019), with the upwelling dynamics having been connected to specific zooplankton assemblages and high biomass (Resgalla Jr et al., 2001) and to maintaining effective diatom populations in the South Brazil Bight over long temporal scales (Brandini et al., 2014). Understanding the net contribution of both the changes in stratification and the stronger bottom water intrusion to the ecological state of the Brazilian shelf is beyond the possibilities of our hydrodynamic model, and would require the explicit simulation of biogeochemical fluxes. This is specially important around the South Brazil Bight and the Southern Shelf, where changes to these physical processes were dominant at the end of the 21st and where industrial and artisanal fishing have large economical and social importance (Castro et al., 2006; Piola et al., 2018).

Bibliography

- Alfredini P, Arasaki E, Pezzoli A, Arcorace M, Cristofori E, de Sousa Jr WC (2014) Exposure of Santos Harbor Metropolitan Area (Brazil) to Wave and Storm Surge Climate Changes. *Water Qual Expo Heal* 6:73–88, doi: 10.1007/s12403-014-0109-7
- Ansorge IJ, Speich S, Lutjeharms JR, Göni GJ, Rautenbach CJ, Froneman PW, Rouault M, Garzoli S (2005) Monitoring the oceanic flow between Africa and Antarctica: Report of the first GoodHope cruise. *S Afr J Sci* 101(1-2):29–35
- Arraut EM, Nobre P, Nobre CA, Scarpa FM (2013) Brazilian Network on Global Climate Change Research (Rede CLIMA): structure, scientific advances and future prospects. *Sustentabilidade em Debate* 3(2):241–256, doi: 10.18472/SustDeb.v3n2.2012.8136
- Atkinson LP, Blanton JO (1986) Process that affect stratification in shelf waters. In: *Baroclinic Process. Cont. Shelves*, vol 3, American Geophysical Union, pp 117–130
- Backhaus JO (1985) A Three-Dimensional Model for the Simulation of Shelf Sea Dynamics. *Dtsch Hydrogr Zeitschrift* 38:165–187
- Barnes EA, Polvani L (2013) Response of the midlatitude jets, and of their variability, to increased greenhouse gases in the CMIP5 models. *J Clim* 26(18):7117–7135, doi: 10.1175/JCLI-D-12-00536.1
- Biastoch A, Böning CW, Schwarzkopf FU, Lutjeharms JR (2009) Increase in Agulhas leakage due to poleward shift of Southern Hemisphere westerlies. *Nature* 462(7272):495–498, doi: 10.1038/nature08519
- Bordin LH, Machado EdC, Carvalho M, Freire AS, Fonseca AL (2019) Nutrient and carbon dynamics under the water mass seasonality on the continental shelf at the South Brazil Bight. *J Mar Syst* 189(September 2018):22–35, doi: 10.1016/j.jmarsys.2018.09.006
- Brandini FP, Nogueira Jr M, Simião M, Codina JCU, Noernberg MA (2014) Deep chlorophyll maximum and plankton community response to oceanic bottom intrusions on the continental shelf in the South Brazilian Bight. *Cont Shelf Res* 89:61–75, doi: 10.1016/j.csr.2013.08.002
- Brandini FP, Tura PM, Santos PP (2018) Ecosystem responses to biogeochemical fronts in the South Brazil Bight. *Prog Oceanogr* 164(December 2017):52–62, doi: 10.1016/j.pocean.2018.04.012

- Breiman L (2001) Random forests. *Mach Learn* 45(1):5–32, doi: 10.1017/CBO9781107415324.004
- Cabré F, Solman S, Núñez M (2014) Climate downscaling over southern South America for present-day climate (1970–1989) using the MM5 model . Mean , interannual variability and internal variability. *Atmósfera* 27(2):117–140, doi: 10.1016/S0187-6236(14)71105-1
- Campos E, Busalacchi A, Garzoli S, Lutjeharms J, Matano R, Nobre P, Olson D, Piola A, Tanajura C, Wainer I (1999a) The South Atlantic and the climate. In: *Proc. Ocean. Ocean Obs. Syst. Clim., Cent. Nat. Etudes Spatiales*, Saint Raphael, France
- Campos EJ, Lorenzzetti JA, Stevenson MR, Stech JL, De Souza RB (1996) Penetration of waters from the Brazil-Malvinas confluence region along the South American continental shelf up to 23°S. *An Acad Bras Cienc* 68(SUPPL. 1):57–58
- Campos EJ, Lentini CA, Miller JL, Piola AR (1999b) Interannual variability of the sea surface temperature in the South Brazil Bight. *Geophys Res Lett* 26(14):2061–2064, doi: 10.1029/1999GL900297
- Campos EJ, Velhote D, Da Silveira IC (2000) Shelfbreak upwelling driven by Brazil current cyclonic meanders. *Geophys Res Lett* 27(6):751–754, doi: 10.1029/1999GL010502
- Campos EJD, Gonçalves JE, Ikeda Y (1995) Water mass characteristics and geostrophic circulation in the South Brazil Bight: Summer of 1991. *J Geophys Res* 100(C9):18537–18550, doi: 10.1029/95jc01724
- Campos PC, Möller OO, Piola AR, Palma ED (2013) Seasonal variability and coastal upwelling near Cape Santa Marta (Brazil). *J Geophys Res Ocean* 118(3):1420–1433, doi: 10.1002/jgrc.20131
- Capotondi A, Alexander MA, Bond NA, Curchitser EN, Scott JD (2012) Enhanced upper ocean stratification with climate change in the CMIP3 models. *J Geophys Res Ocean* 117(4):1–23, doi: 10.1029/2011JC007409
- Carton JA, Giese BS (2008) A Reanalysis of Ocean Climate Using Simple Ocean Data Assimilation (SODA). *Mon Weather Rev* 136(8):2999–3017, doi: 10.1175/2007MWR1978.1
- Castelao RM, Barth JA (2006) Upwelling around Cabo Frio, Brazil: The importance of wind stress curl. *Geophys Res Lett* 33(3):2–5, doi: 10.1029/2005GL025182
- Castelao RM, Campos EJD, Miller JL (2004) A Modelling Study of Coastal Upwelling Driven by Wind and Meanders of the Brazil Current. *J Coast Res* 203:662–671, doi: 10.2112/1551-5036(2004)20[662:AMSOCU]2.0.CO;2

- Castello JP, Möller Jr OO (1977) Sobre as condições oceanográficas no Rio Grande do Sul, Brasil. *Atlântica* 2:25–110
- Castro BM (2014) Summer / winter stratification variability in the central part of the South Brazil Bight. *Cont Shelf Res* 89:15–23, doi: 10.1016/j.csr.2013.12.002
- Castro BM, Miranda LB (1998) Physical oceanography of the Western Atlantic continental shelf located between 4° N and 34° S. In: Robinson AR, Brink KH (eds) *Sea*, John Wiley & Sons, New York, pp 20–251
- Castro BM, Brandini FP, Pires-Vanin AMS, Miranda LB (2006) Multidisciplinary oceanographic processes on the Western Atlantic continental shelf between 4° N and 34° S. In: Robinson AR, Brink KH (eds) *Sea Ideas Obs. Prog. Study Seas, Part A. Panregional Synth. Coasts North South Am. Asia*, vol 14, Harvard University Press, Cambridge, MA, chap 8, pp 259–294
- Cerda C, Castro BM (2014) Hydrographic climatology of South Brazil Bight shelf waters between Sao Sebastiao (24°S) and Cabo Sao Tome (22°S). *Cont Shelf Res* 89:5–14, doi: 10.1016/j.csr.2013.11.003
- Chou SC, Marengo JA, Lyra AA, Sueiro G, Pesquero JF, Alves LM, Kay G, Betts R, Chagas DJ, Gomes JL, Bustamante JF, Tavares P (2012) Downscaling of South America present climate driven by 4-member HadCM3 runs. *Clim Dyn* 38:635–653, doi: 10.1007/s00382-011-1002-8
- Combes V, Matano RP (2014a) A two-way nested simulation of the oceanic circulation in the Southwestern Atlantic. *J Geophys Res Ocean* 119:731–756, doi: 10.1002/2013JC009498. Received
- Combes V, Matano RP (2014b) Trends in the Brazil/Malvinas Confluence region. *Geophys Res Lett* 41:8971–8977, doi: 10.1002/2014GL062523
- Daewel U, Schrum C (2017) Low frequency variability in North Sea and Baltic Sea identified through simulations with the 3-d coupled physical-biogeochemical model ECOSMO. *Earth Syst Dyn Discuss* (April):1–23, doi: 10.5194/esd-2017-36
- Davis SM, Rosenlof KH (2012) A multidiagnostic intercomparison of tropical-width time series using reanalyses and satellite observations. *J Clim* 25(4):1061–1078, doi: 10.1175/JCLI-D-11-00127.1
- Döll P, Kaspar F, Lehner B (2003) A global hydrological model for deriving water availability indicators: model tuning and validation. *J Hydrol* 270(1):105–134, doi: 10.1016/S0022-1694(02)00283-4

- Downes SM, Hogg AMCC (2013) Southern Ocean Circulation and Eddy Compensation in CMIP5 Models. *J Clim* 26(18):7198–7220, doi: 10.1175/JCLI-D-12-00504.1
- de Figueiredo SA, Calliari LJ, Machado AA (2018) Modelling the effects of sea-level rise and sediment budget in coastal retreat at hermenegildo beach, Southern Brazil. *Brazilian J Oceanogr* 66(2):210–219, doi: 10.1590/s1679-87592018009806602
- Friedman JH (2001) Greedy Function Approximation: A Gradient Boosting Machine. *Ann Stat* 29(5):1189–1232
- Fu W, Randerson JT, Keith Moore J (2016) Climate change impacts on net primary production (NPP) and export production (EP) regulated by increasing stratification and phytoplankton community structure in the CMIP5 models. *Biogeosciences* 13(18):5151–5170, doi: 10.5194/bg-13-5151-2016
- Gabioux M, da Costa VSC, de Souza JMAC, de Oliveira BE, Paiva AM (2013) Modeling the south atlantic ocean from medium to high-resolution. *Rev Bras Geofis* 31(2):229–242
- Gilliland JM, Keim BD (2018) Position of the South Atlantic anticyclone and its impact on surface conditions across Brazil. *J Appl Meteorol Climatol* 57(3):535–553, doi: 10.1175/JAMC-D-17-0178.1
- Giorgetta Ma, Jungclaus JH, Reick CH, Legutke S, Bader J, Böttinger M, Brovkin V, Crueger T, Esch M, Fieg K, Glushak K, Gayler V, Haak H, Hollweg HD, Ilyina T, Kinne S, Kornbluh L, Matei D, Mauritsen T, Mikolajewicz U, Mueller W, Notz D, Pithan F, Raddatz T, Rast S, Redler R, Roeckner E, Schmidt H, Schnur R, Segschneider J, Six KD, Stockhause M, Timmreck C, Wegner J, Widmann H, Wieners KH, Claussen M, Marotzke J, Stevens B (2013) Climate and carbon cycle changes from 1850 to 2100 in MPI-ESM simulations for the coupled model intercomparison project phase 5. *J Adv Model Earth Syst* 5(3):572–597, doi: 10.1002/jame.20038
- Goni GJ, Bringas F, Dinezio PN (2011) Observed low frequency variability of the Brazil Current front. *J Geophys Res Ocean* 116(10):1–10, doi: 10.1029/2011JC007198
- Gordon AL (1981) South Atlantic thermocline ventilation. *Deep Sea Res Part A, Oceanogr Res Pap* 28(11):1239–1264, doi: 10.1016/0198-0149(81)90033-9
- Gouretski V (2018) World ocean circulation experiment-argo global hydrographic climatology. *Ocean Sci* 14(5):1127–1146, doi: 10.5194/os-14-1127-2018
- Gronholz A, Gräwe U, Paul A, Schulz M (2017) Investigating the effects of a summer storm on the North Sea stratification using a regional coupled ocean-atmosphere model. *Ocean Dyn* 67(2):211–235, doi: 10.1007/s10236-016-1023-2

- Gupta AS, Santoso A, Taschetto AS, Ummenhofer CC, Trevena J, England MH (2009) Projected changes to the Southern Hemisphere ocean and sea ice in the IPCC AR4 climate models. *J Clim* 22(11):3047–3078, doi: 10.1175/2008JCLI2827.1
- Harley CD, Hughes AR, Hultgren KM, Miner BG, Sorte CJ, Thornber CS, Rodriguez LF, Tomanek L, Williams SL (2006) The impacts of climate change in coastal marine systems. *Ecol Lett* 9(2):228–241, doi: 10.1111/j.1461-0248.2005.00871.x
- Hein H, Hein B, Pohlmann T, Long BH (2013) Inter-annual variability of upwelling off the South-Vietnamese coast and its relation to nutrient dynamics. *Glob Planet Change* 110:170–182, doi: 10.1016/j.gloplacha.2013.09.009
- Ho M, Kiem AS, Verdon-Kidd DC (2012) The Southern Annular Mode: A comparison of indices. *Hydrol Earth Syst Sci* 16(3):967–982, doi: 10.5194/hess-16-967-2012
- Holt J, Wakelin S, Lowe J, Tinker J (2010) The potential impacts of climate change on the hydrography of the northwest European continental shelf. *Prog Oceanogr* 86(3-4):361–379, doi: 10.1016/j.pocean.2010.05.003
- Holt J, Polton J, Huthnance J, Wakelin S, O'Dea E, Harle J, Yool A, Artioli Y, Blackford J, Siddorn J, Inall M (2018) Climate-Driven Change in the North Atlantic and Arctic Oceans Can Greatly Reduce the Circulation of the North Sea. *Geophys Res Lett* 45(21):11,827–11,836, doi: 10.1029/2018GL078878
- Hordoir R, Meier HE (2012) Effect of climate change on the thermal stratification of the baltic sea: A sensitivity experiment. *Clim Dyn* 38(9-10):1703–1713, doi: 10.1007/s00382-011-1036-y
- Hounsou-Gbo GA, Servain J, Araujo M, Martins ES, Bourlès B, Caniaux G (2016) Oceanic Indices for Forecasting Seasonal Rainfall over the Northern Part of Brazilian Northeast. *Am J Clim Chang* 05(02):261–274, doi: 10.4236/ajcc.2016.52022
- Hu Y, Huang H, Zhou C (2018) Widening and weakening of the Hadley circulation under global warming. *Sci Bull* 63(10):640–644, doi: 10.1016/j.scib.2018.04.020
- IBGE (2011) Atlas geográfico das zonas costeiras e oceânicas do Brasil. Rio de Janeiro, RJ, Brasil
- IPCC (2013) The physical science basis. Contribution of working group I to the fifth assessment report of the intergovernmental panel on climate change. Cambridge University Press, Cambridge, UK and New York, NY, USA, doi: 10.1017/CBO9781107415324.015
- IPCC (2014) Climate Change 2014: Synthesis Report. Contribution of Working Groups I, II and III to the Fifth Assessment Report of the Intergovernmental Panel on Climate Change. IPCC, Geneva, Switzerland

- Johns WE, Lee TN, Beardsley RC, Candela J, Limeburner R, Castro B (1998) Annual cycle and variability of the North Brazil current. *J Phys Oceanogr* 28(1):103–128, doi: 10.1175/1520-0485(1998)028<0103:ACAVOT>2.0.CO;2
- Jungclaus JH, Keenlyside N, Botzet M, Haak H, Luo JJ, Latif M, Marotzke J, Mikolajewicz U, Roeckner E (2006) Ocean circulation and tropical variability in the coupled model ECHAM5/MPI-OM. *J Clim* 19(16):3952–3972, doi: 10.1175/JCLI3827.1
- Jungclaus JH, Fischer N, Haak H, Lohmann K, Marotzke J, Matei D, Mikolajewicz U, Notz D, Von Storch JS (2013) Characteristics of the ocean simulations in the Max Planck Institute Ocean Model (MPIOM) the ocean component of the MPI-Earth system model. *J Adv Model Earth Syst* 5(2):422–446, doi: 10.1002/jame.20023
- Kalnay E, Kanamitsu M, Kistler R, Collins W, Deaven D, Gandin L, Iredell M, Saha S, White G, Woollen J, Zhu Y, Chelliah M, Ebisuzaki W, Higgins W, Janowiak J, Mo KC, Ropelewski C, Wang J, Leetmaa A, Reynolds R, Jenne R, Joseph D (1996) The NCEP/NCAR 40-year reanalysis project. *Bull Am Meteorol Soc* 77(3):437–471, doi: 10.1175/1520-0477(1996)077<0437:TNYP>2.0.CO;2
- Kang SM, Lu J (2012) Expansion of the Hadley cell under global warming: Winter versus summer. *J Clim* 25(24):8387–8393, doi: 10.1175/JCLI-D-12-00323.1
- Kazmin AS (2017) Variability of the climatic oceanic frontal zones and its connection with the large-scale atmospheric forcing. *Prog Oceanogr* 154:38–48, doi: 10.1016/j.pocean.2017.04.012
- Ke G, Meng Q, Wang T, Chen W, Ma W, Liu TY, Finley T, Wang T, Chen W, Ma W, Ye Q, Liu TY (2017) LightGBM: A highly efficient gradient boosting decision tree. *Adv Neural Inf Process Syst (Nips)*:3149–3157
- Keeling RF, Körtzinger A, Gruber N (2010) Ocean Deoxygenation in a Warming World. *Ann Rev Mar Sci* 2(1):199–229, doi: 10.1146/annurev.marine.010908.163855
- Kjellsson J, Zanna L (2017) The Impact of Horizontal Resolution on Energy Transfers in Global Ocean Models. *Fluids* 2(3):45, doi: 10.3390/fluids2030045
- Kochergin VP (1987) Three-Dimensional Prognostic Models. In: *Three-Dimensional Coast. Ocean Model.*, American Geophysical Union, pp 201–208, doi: <http://dx.doi.org/10.1029/CO004p0201>
- Kohonen T (1990) The Self-Organizing Map. In: *Proc. IEEE*, vol 78, pp 1464–1480, doi: 10.1109/5.58325

- Kohonen T (2001) *Self-Organizing Maps*, 3rd edn. Springer-Verlag Berlin Heidelberg, Berlin, doi: 10.1007/978-3-642-56927-2
- Kouadio YK, Servain J, MacHado LA, Lentini CA (2012) Heavy rainfall episodes in the eastern northeast brazil linked to large-scale ocean-atmosphere conditions in the tropical atlantic. *Adv Meteorol* 2012, doi: 10.1155/2012/369567
- Kushner PJ, Held IM, Delworth TL (2000) Southern Hemisphere Atmospheric Circulation Response to Global Warming. *J Clim* 14:2238–2249
- Lacerda F, Nobre P (2010) Aquecimento Global: Conceituação E Repercussões Sobre O Brasil. *Rev Bras Geogr Física* 3(1):14–17, doi: 10.26848/rbgf.v3i1.232653
- Landschützer P, Gruber N, Bakker DC, Schuster U, Nakaoka S, Payne MR, Sasse TP, Zeng J (2013) A neural network-based estimate of the seasonal to inter-annual variability of the Atlantic Ocean carbon sink. *Biogeosciences* 10(11):7793–7815, doi: 10.5194/bg-10-7793-2013
- Laruelle GG, Landschützer P, Gruber N, Tison JL, Delille B, Regnier P (2017) Global high resolution monthly pCO₂ climatology for the coastal ocean derived from neural network interpolation. *Biogeosciences* (2014):1–40, doi: 10.5194/bg-2017-64
- Laurent A, Fennel K, Ko DS, Lehrter J (2018) Climate change projected to exacerbate impacts of coastal Eutrophication in the Northern Gulf of Mexico. *J Geophys Res Ocean* 123(5):3408–3426, doi: 10.1002/2017JC013583
- Lentz SJ (1995) Seasonal variations in the horizontal structure of the Amazon Plume inferred from historical hydrographic data. *J Geophys Res* 100(C2):2391– 2400
- Lessin G, Polimene L, Artioli Y, Butenschön M, Clark DR, Brown I, Rees AP (2020) Modeling the seasonality and controls of nitrous oxide emissions on the northwest European continental shelf. *J Geophys Res Biogeosciences* doi: 10.1029/2019JG005613
- Levitus S (1983) Climatological Atlas of the World Ocean. *Eos, Trans Am Geophys Union* 64(49):962–963, doi: 10.1029/EO064i049p00962-02
- Lima ID, Garcia CA, Möller OO (1996) Ocean surface processes on the Southern Brazilian shelf: Characterization and seasonal variability. *Cont Shelf Res* 16(10):1307–1317, doi: 10.1016/0278-4343(95)00066-6
- Liu Y, Lee Sk, Enfield DB, Muhling BA, Lamkin JT, Muller-Karger FE, Roffer MA (2015) Potential impact of climate change on the Intra-Americas Sea : Part-1 . A dynamic down-scaling of the CMIP5 model projections. *J Mar Syst* 148:56–69, doi: 10.1016/j.jmarsys.2015.01.007

- Liu Y, Weisberg RH, Vignudelli S, Mitchum GT (2016) Patterns of the loop current system and regions of sea surface height variability in the eastern Gulf of Mexico revealed by the self-organizing maps. *J Geophys Res Ocean* 121:2347–2366, doi: 10.1002/2015JC011493
- Lobo VJ (2009) Application of self-organizing maps to the maritime environment. In: *Inf. Fusion Geogr. Inf. Syst.*, Springer, Berlin, vol 20, pp 19–36, doi: 10.1007/978-3-642-00304-2-2
- Lorenz EN (1955) Available Potential Energy and the Maintenance of the General Circulation. *Tellus* 7(2):157–167, doi: 10.3402/tellusa.v7i2.8796
- Lumpkin R, Garzoli S (2011) Interannual to decadal changes in the western South Atlantic's surface circulation. *J Geophys Res* 116(November 2010):1–10, doi: 10.1029/2010JC006285
- Marengo JA, Chou SC, Kay G, Alves LM, Pesquero JF, Soares WR, Santos DC, Lyra AA, Sueiro G, Betts R, Chagas DJ, Gomes JL, Bustamante JF, Tavares P (2012) Development of regional future climate change scenarios in South America using the Eta CPTEC / HadCM3 climate change projections : climatology and regional analyses for the Amazon , São Francisco and the Paraná River basins. *Clim Dyn* 38:1829–1848, doi: 10.1007/s00382-011-1155-5
- Marshall GJ (2003) Trends in the Southern Annular Mode from observations and reanalyses. *J Clim* 16(24):4134–4143, doi: 10.1175/1520-0442(2003)016<4134:TITSAM>2.0.CO;2
- Martins KA, Souza Pereira PD, Silva-Casarín R, Nogueira Neto AV (2017) The Influence of Climate Change on Coastal Erosion Vulnerability in Northeast Brazil. *Coast Eng J* 59(2), doi: 10.1142/S0578563417400071
- Matano RPRP, Schlax MG, Chelton DB (1993) Seasonal variability in the southwestern Atlantic. *J Geophys Res* 98(C10):18027, doi: doi:10.1029/93JC01602
- Mathis M, Mikolajewicz U (2020) The impact of meltwater discharge from the Greenland ice sheet on the Atlantic nutrient supply to the northwest European shelf. *Ocean Sci* 16(1):167–193, doi: 10.5194/os-16-167-2020
- Mathis M, Pohlmann T (2014) Projection of physical conditions in the North Sea for the 21st century. *Clim Res* 61:1–17, doi: 10.3354/cr01232
- Mathis M, Mayer B, Pohlmann T (2013) An uncoupled dynamical downscaling for the North Sea : Method and evaluation. *Ocean Model* 72:153–166, doi: 10.1016/j.ocemod.2013.09.004

- Mathis M, Elizalde A, Mikolajewicz U (2018) Which complexity of regional climate system models is essential for downscaling anthropogenic climate change in the Northwest European Shelf? *Clim Dyn* 50(7-8):2637–2659, doi: 10.1007/s00382-017-3761-3
- de Miranda AP, Barnier B, Dewar WK (1999) On the dynamics of the Zapiola Anticyclone. *J Geophys Res* 104(C9):21137–21149, doi: 10.1029/1999jc900042
- Miranda PM, Alves JM, Serra N (2013) Climate change and upwelling: Response of Iberian upwelling to atmospheric forcing in a regional climate scenario. *Clim Dyn* 40(11-12):2813–2824, doi: 10.1007/s00382-012-1442-9
- Möller OO, Piola AR, Freitas AC, Campos EJ (2008) The effects of river discharge and seasonal winds on the shelf off southeastern South America. *Cont Shelf Res* 28(13):1607–1624, doi: 10.1016/j.csr.2008.03.012
- Morioka Y, Tozuka T, Yamagata T (2011) On the growth and decay of the subtropical dipole mode in the South Atlantic. *J Clim* 24(21):5538–5554, doi: 10.1175/2011JCLI4010.1
- Nobre CA (2008) Mudanças climáticas globais e o Brasil : por que devemos nos preocupar. Tech. rep., Biblioteca Digital da Câmara dos Deputados, Brasília
- Nobre P, de Almeida RA, Malagutti M, Giarolla E (2012a) Coupled Ocean – Atmosphere Variations over the South Atlantic Ocean. *J Clim* 25:6349–6358, doi: 10.1175/JCLI-D-11-00444.1
- Nobre P, Siqueira LSP, de Almeida RA, Malagutti M, Giarolla E, Castelão GP, Bottino MJ, Kubota P, Figueroa SN, Costa MC, Baptista Jr M, Irber Jr L, Marcondes GG (2012b) Climate Simulation and Change in the Brazilian Climate Model. *J Clim* 26:6716–6732, doi: 10.1175/JCLI-D-12-00580.1
- Oke PR, Middleton JH (2000) Topographically induced upwelling off Eastern Australia. *J Phys Oceanogr* 30(3):512–531, doi: 10.1175/1520-0485(2000)030<0512:TIUOEA>2.0.CO;2
- Oliveira LR, Piola AR, Mata MM, Soares ID (2009) Brazil Current surface circulation and energetics observed from drifting buoys. *J Geophys Res Ocean* 114(10):1–12, doi: 10.1029/2008JC004900
- Palma ED, Matano RP (2009) Disentangling the upwelling mechanisms of the South Brazil Bight. *Cont Shelf Res* 29:1525–1534, doi: 10.1016/j.csr.2009.04.002
- Palma ED, Matano RP, Piola AR (2008) A numerical study of the Southwestern Atlantic Shelf circulation: Stratified ocean response to local and offshore forcing. *J Geophys Res* 113(May):1–22, doi: 10.1029/2007JC004720

- Palóczy A, Brink KH, da Silveira ICA, Arruda WZ, Martins RP (2016) Pathways and mechanisms of offshore water intrusions on the Espírito Santo Basin shelf (18S–22S, Brazil). *J Geophys Res Ocean* 121:5134–5163, doi: 10.1002/2015JC011486. Received
- PBMC (2014) Base científica das mudanças climáticas. Contribuição do Grupo de Trabalho 1 do Painel Brasileiro de Mudanças Climáticas ao Primeiro Relatório da Avaliação Nacional sobre Mudanças Climáticas. COPPE, Universidade Federal do Rio de Janeiro, Rio de Janeiro, RJ, Brasil
- Pereira AF, Belém AL, Castro BM, Geremias R (2005) Tide-topography interaction along the eastern Brazilian shelf. *Cont Shelf Res* 25(12-13):1521–1539, doi: 10.1016/j.csr.2005.04.008
- Pereira EB, Martins FR, Pes MP, Segundo ElIdC, Lyra AA (2013) The impacts of global climate changes on the wind power density in Brazil. *Renew Energy* 49:107–110, doi: 10.1016/j.renene.2012.01.053
- Pimenta FM, Campos EJD, Miller JL, Piola AR (2005) A numerical study of the Plata River plume along the southeastern South American continental shelf. *Brazilian J Oceanogr* 53(3-4):129–146, doi: 10.1590/s1679-87592005000200004
- Piola AR, Matano RP (2017) Ocean Currents: Atlantic Western Boundary—Brazil Current/Falkland (Malvinas) Current. December, Elsevier Inc., doi: 10.1016/B978-0-12-409548-9.10541-X
- Piola AR, Campos EJD, Möller OO, Charo M, Martinez C (2000) Subtropical Shelf Front off eastern South America. *J Geophys Res Ocean* 105(C3):6565–6578, doi: 10.1029/1999JC000300
- Piola AR, Matano RP, Palma ED, Möller OO, Campos EJ (2005) The influence of the Plata River discharge on the western South Atlantic shelf. *Geophys Res Lett* 32(1):1–4, doi: 10.1029/2004GL021638
- Piola AR, Möller OO, Guerrero RA, Campos EJ (2008) Variability of the subtropical shelf front off eastern South America: Winter 2003 and summer 2004. *Cont Shelf Res* 28(13):1639–1648, doi: 10.1016/j.csr.2008.03.013
- Piola AR, Palma ED, Bianchi AA, Castro BM, Dottori M, Guerrero RA, Marrari M, Matano RP, Möller OO, Saraceno M (2018) Physical Oceanography of the SW Atlantic Shelf: A Review. In: Hoffmeyer MS, Sabatini ME, Brandini FP, Calliari DL, Santinelli NH (eds) *Plankt. Ecol. Southwest. Atl. From Subtrop. to Subantarctic Realm*, Springer International Publishing, Cham, pp 37–56

- Pohlmann T (1996) Predicting the thermocline in a circulation model of the North Sea - Part I: Model description, calibration and verification. *Cont Shelf Res* 16(2):131–146, doi: 10.1016/0278-4343(95)90885-S
- Pohlmann T (2006) A meso-scale model of the central and southern North Sea: Consequences of an improved resolution. *Cont Shelf Res* 26:2367–2385, doi: 10.1016/j.csr.2006.06.011
- Pontes GM, Gupta AS, Taschetto AS (2014) Projected changes to South Atlantic boundary currents and confluence region in the CMIP5 models : the role of wind and deep ocean changes. *Environ Res Lett* 11(9):1–9, doi: 10.1088/1748-9326/11/9/094013
- Praveen V, Ajayamohan RS, Valsala V, Sandeep S (2016) Intensification of upwelling along Oman coast in a warming scenario. *Geophys Res Lett* 43(14):7581–7589, doi: 10.1002/2016GL069638
- Ramos da Silva R, Haas R (2016) Ocean global warming impacts on the South America climate. *Front Earth Sci* 4(March):1–8, doi: 10.3389/feart.2016.00030
- Randerson JT, Lindsay K, Munoz E, Fu W, Moore JK, Hoffman FM, Mahowald NM, Doney SC (2015) Multicentury changes in ocean and land contributions to the climate-carbon feedback. *Global Biogeochem Cycles* 29:744–759, doi: 10.1111/1462-2920.13280
- Reboita MS, Ambrizzi T, Silva BA, Pinheiro RF, da Rocha RP (2019) The south atlantic subtropical anticyclone: Present and future climate. *Front Earth Sci* 7(February):1–15, doi: 10.3389/feart.2019.00008
- Renault L, McWilliams JC, Penven P (2017) Modulation of the Agulhas Current Retroflection and Leakage by Oceanic Current Interaction with the Atmosphere in Coupled Simulations. *J Phys Oceanogr* 47(346):2077–2100, doi: 10.1175/JPO-D-16-0168.1
- Resgalla Jr C, de La Rocha C, Montú M (2001) The Influence of Ekman Transport on Zooplankton Biomass Variability off Southern Brazil. *J Plankton Res* 23(6):641–650, doi: 10.1093/plankt/23.6.641
- Robertson AW, Mechoso CR (2000) Interannual and interdecadal variability of the South Atlantic Convergence Zone. *Mon Weather Rev* 128:2947–2957, doi: 10.1175/1520-0493(2000)128<2947:IAIVOT>2.0.CO;2
- Rodrigues RR, Campos EJD, Haarsma R (2015) The impact of ENSO on the south Atlantic subtropical dipole mode. *J Clim* 28(7):2691–2705, doi: 10.1175/JCLI-D-14-00483.1

- Rykaczewski RR, Dunne JP, Sydemann WJ, García-reyes M, Black BA, Bograd SJ (2015) Poleward displacement of coastal upwelling-favorable winds in the ocean's eastern boundary currents through the 21st century. *Geophys Res Lett* 42:6424–6431, doi: 10.1002/2015GL064694
- Silveira ICA, Schmidt ACK, Campos EJD, de Godoi SS, Ikeda Y (2000) A corrente do Brasil ao largo da costa leste brasileira. *Rev Bras Oceanogr* 48(2):171–183, doi: 10.1590/S1413-77392000000200008
- Simpson JH (1981) The shelf-sea fronts : implications of their existence and behaviour. *Philos Trans R Soc London* 302:531–546
- Smagorinsky J (1963) General Circulation Experiments With the Primitive Equations. *Mon Weather Rev* 91(3):99–164, doi: 10.1175/1520-0493(1963)091<0099:GCEWTP>2.3.CO;2
- Snyder MA, Sloan LC, Diffenbaugh NS, Bell JL (2003) Future climate change and upwelling in the California Current. *Geophys Res Lett* 30(15):1–4, doi: 10.1029/2003GL017647
- Soares J, de Castro Filho BM (1996) Numerical modeling of the response of Ceará continental shelf waters to wind stress forcing. *Rev Bras Oceanogr* 44(2):135–153, doi: 10.1590/s1413-77391996000200004
- Song YT, Chao Y (2004) A theoretical study of topographic effects on coastal upwelling and cross-shore exchange. *Ocean Model* 6:151–176, doi: 10.1016/S1463-5003(02)00064-1
- Sousa MC, Alvarez I, DeCastro M, Gomez-Gesteira M, Dias JM (2017) Seasonality of coastal upwelling trends under future warming scenarios along the southern limit of the canary upwelling system. *Prog Oceanogr* 153:16–23, doi: 10.1016/j.pocean.2017.04.002
- de Souza MM, Mathis M, Pohlmann T (2019) Driving mechanisms of the variability and long - term trend of the Brazil – Malvinas confluence during the 21st century. *Clim Dyn* 53:6453–6468, doi: <https://doi.org/10.1007/s00382-019-04942-7>
- de Souza MM, Mathis M, Mayer B, Noernberg MA, Pohlmann T (2020) Possible impacts of anthropogenic climate change to the upwelling in the South Brazil Bight. *Clim Dyn* 55:651–664, doi: 10.1007/s00382-020-05289-0
- Spadone A, Provost C (2009) Variations in the Malvinas Current volume transport since October 1992. *J Geophys Res* 114(2):1–21, doi: 10.1029/2008JC004882
- Sprintall J, Tomczak M (1993) On the formation of central water and thermocline ventilation in the southern hemisphere. *Deep Res Part I* 40(4):827–848, doi: 10.1016/0967-0637(93)90074-D

- Stevens B, Giorgetta M, Esch M, Mauritsen T, Crueger T, Rast S, Salzmann M, Schmidt H, Block K, Brokopf R, Fast I, Kinne S, Kornblueh L, Lohmann U, Pincus R, Reichler T, Roeckner E (2013) Atmospheric component of the MPI-M Earth System Model: ECHAM6. *J Adv Model Earth Syst* 5:146–172, doi: 10.1002/jame.20015
- Stramma L, England M (1999) On the water masses and mean circulation of the South Atlantic Ocean. *J Geophys Res* 104(9):20863–20883, doi: 10.1029/1999JC900139
- Su J, Pohlmann T (2009) Wind and topography influence on an upwelling system at the eastern Hainan coast. *J Geophys Res Ocean* 114(6):1–19, doi: 10.1029/2008JC005018
- Sun X, Cook KH, Vizy EK (2017) The South Atlantic subtropical high: Climatology and interannual variability. *J Clim* 30(9):3279–3296, doi: 10.1175/JCLI-D-16-0705.1
- Swart NC, Fyfe JC (2012) Observed and simulated changes in the Southern Hemisphere surface westerly wind-stress. *Geophys Res Lett* 39(16):6–11, doi: 10.1029/2012GL052810
- Sydeman WJ, Schoeman DS, Rykaczewski RR, Thompson SA, Black BA, Bograd SJ (2014) Climate change and wind intensification in coastal upwelling ecosystems. *Science* (80-) 345(6192):77–80
- Toste R, Assad LPdF, Landau L (2018) Downscaling of the global HadGEM2-ES results to model the future and present-day ocean conditions of the southeastern Brazilian continental shelf. *Clim Dyn* 51(1-2):143–159, doi: 10.1007/s00382-017-3911-7
- Trenberth KE (1997) The definition of El Niño. *Bull Amer Meteorol Soc* 78(August):2771–2777
- Urakawa LS, Hasumi H (2009) The energetics of global thermohaline circulation and its wind enhancement. *J Phys Oceanogr* 39(7):1715–1728, doi: 10.1175/2009JPO4073.1
- Urakawa LS, Saenz JA, Hogg AM (2013) Available potential energy gain from mixing due to the nonlinearity of the equation of state in a global ocean model. *Geophys Res Lett* 40(10):2224–2228, doi: 10.1002/grl.50508
- Varela R, Lima FP, Seabra R, Meneghesso C, Gómez-Gesteira M (2018) Coastal warming and wind-driven upwelling: A global analysis. *Sci Total Environ* 639:1501–1511, doi: 10.1016/j.scitotenv.2018.05.273
- van Vuuren DP, Edmonds J, Kainuma M, Riahi K, Thomson A, Hibbard K, Hurtt GC, Kram T, Krey V, Lamarque JF, Masui T, Meinshausen M, Nakicenovic N, Smith SJ, Rose SK (2011) The representative concentration pathways: An overview. *Clim Change* 109(1):5–31, doi: 10.1007/s10584-011-0148-z

- Wainer I, Gent P, Goni G (2000) Annual cycle of the Brazil-Malvinas confluence region in the National Center for Atmospheric Research Climate System Model. *J Geophys Res Ocean* 105(C11):26167–26177, doi: 10.1029/1999JC000134
- Wan X, Chang P, Jackson CS, Ji L, Li M (2011) Plausible effect of climate model bias on abrupt climate change simulations in Atlantic sector. *Deep Res II* 58(17-18):1904–1913, doi: 10.1016/j.dsr2.2010.10.068
- Wang D, Gouhier TC, Menge BA, Ganguly AR (2015) Intensification and spatial homogenization of coastal upwelling under climate change. *Nature* 518(7539):390–394, doi: 10.1038/nature14235
- Wang M, Overland JE, Bond NA (2010) Climate projections for selected large marine ecosystems. *J Mar Syst* 79(3-4):258–266, doi: 10.1016/j.jmarsys.2008.11.028
- Wang Z, Kuhlbrodt T, Meredith MP (2011) On the response of the Antarctic Circumpolar Current transport to climate change in coupled climate models. *J Geophys Res Ocean* 116(8):1–17, doi: 10.1016/j.bios.2012.10.063
- Wilcox LJ, Charlton-Perez AJ, Gray LJ (2012) Trends in Austral jet position in ensembles of high- and low-top CMIP5 models. *J Geophys Res Atmos* 117(13):1–10, doi: 10.1029/2012JD017597
- Yamaguchi R, Suga T, Richards KJ, Qiu B (2019) Diagnosing the development of seasonal stratification using the potential energy anomaly in the North Pacific. *Clim Dyn* 53(7-8):4667–4681, doi: 10.1007/s00382-019-04816-y
- Yang XY, He Z (2014) Decadal change of Antarctic Intermediate Water in the region of Brazil and Malvinas confluence. *Deep Res Part I Oceanogr Res Pap* 88(1):1–7, doi: 10.1016/j.dsr.2014.02.007
- Zavialov PO, Wainer I, Absy JM (1999) Sea surface temperature variability off southern Brazil and Uruguay as revealed from historical data since 1854. *J Geophys Res* 104(C9):21021–21032, doi: 10.1029/1998JC900096
- Zheng F, Li J, Clark RT, Nnamchi HC (2013) Simulation and projection of the Southern Hemisphere annular mode in CMIP5 models. *J Clim* 26(24):9860–9879, doi: 10.1175/JCLI-D-13-00204.1

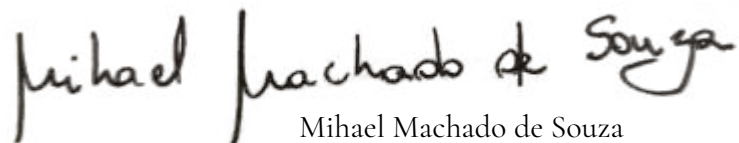
Affirmation on Oath

Deutsch

Hiermit versichere ich an Eides statt, dass ich die vorliegende Dissertation mit dem Titel: „Effects of Climate Change on the Physical Conditions of the Brazilian Shelf“ selbstständig verfasst und keine anderen als die angegebenen Hilfsmittel – insbesondere keine im Quellenverzeichnis nicht benannten Internet-Quellen – benutzt habe. Alle Stellen, die wörtlich oder sinngemäß aus Veröffentlichungen entnommen wurden, sind als solche kenntlich gemacht. Ich versichere weiterhin, dass ich die Dissertation oder Teile davon vorher weder im In- noch im Ausland in einem anderen Prüfungsverfahren eingereicht habe und die eingereichte schriftliche Fassung der auf dem elektronischen Speichermedium entspricht.

English

I hereby declare an oath that I have written the present dissertation on my own with the title: "Effects of Climate Change on the Physical Conditions of the Brazilian Shelf" and have not used other than the acknowledge resources and aids. All passages taken literally or analogously from other publications are identified as such. I further declare that this thesis has not been submitted to any other German or foreign examination board and that the submitted written version corresponds to that on the electronic repository.

A handwritten signature in black ink, reading "Mihael Machado de Souza". The signature is written in a cursive, flowing style.

Mihael Machado de Souza

Hamburg, October 1, 2020